First Principles-based Thermokinetic Modeling of Steels and Ni Alloys for Nuclear Applications

By

Leland Barnard

A dissertation submitted in partial fulfillment of the

requirements for the degree of

Doctor of Philosophy

(Materials Science)

at the

UNIVERSITY OF WISCONSIN-MADISON

2013

Date of final oral examination: 12/06/2013

The dissertation is approved by the following members of the Final Oral Committee

Dane Morgan, Associate Professor, Materials Science and Engineering
J. R. Schmidt, Assistant Professor, Chemistry
Kumar Sridharan, Distinguished Research Professor, Engineering Physics
Izabela Szlufarska, Associate Professor, Materials Science and Engineering
Xudong Wang, Assistant Professor, Materials Science and Engineering
George Young, Advisory Scientist, Knolls Atomic Power Laboratory

Abstract

The objective of this dissertation was to develop multiscale modeling frameworks for describing modes of thermal and radiation-induced degradation in steels and Ni alloys for nuclear applications. The development of these models was performed according to the following general method: first, electronic structure calculations were performed to obtain key atomistic energies and insights. These calculations then formed a foundation for atomistic simulations and continuum level models used to describe microstructural processes of interest. The results of these models were compared to experimental measurements, and used to identify the fundamental mechanisms underlying the observed material phenomena.

This approach was applied to three distinct topics. The first is the theory and prediction of radiation induced segregation in the Ni-Cr and Fe-Cr systems. In this subproject, the modeling effort yielded an important new understanding of the role of interstitial diffusion in radiation induced segregation. The effects of defect annihilation kinetics at grain boundaries were also examined. The second topic was the kinetics of the disorder-order phase transformation in Ni-Cr alloys. This project resulted in a physics-based model for describing the phase transformation that shows good agreement with both atomistic simulations and experimental measurements. The predictions of this model indicate that this phase transformation may be of serious concern in Ni-Cr alloys near the Ni_2Cr stoichiometry during very long service lifetimes. Finally, the third topic was the evolution of oxide nanoprecipitates in nanostructured ferritic alloys. The key results of this effort were a better understanding of nanoprecipitate coarsening mechanisms and the effects of alloy composition on nanoprecipitate size distribution. The predictions of this model also indicate that the nanoprecipitates in

nanostructured ferritic alloys should be thermally stable for as long as 80 years at proposed operating temperatures. In all three projects the first principles-based foundation provided by the electronic structure calculations allowed the resulting models to go beyond empirical fitting, and to provide understanding of the mechanisms underlying the microstructural processes of interest.

Acknowledgements

This dissertation would not have been possible without the aid of many individuals. Foremost, I would like to thank Professor Dane Morgan, my principal advisor. This project was fueled by his contagious enthusiasm, and steered by his thoughtful prudence. I would also like to thank both Professors Izabela Szlufarska and Dane Morgan for creating a truly exceptional group environment. They lead by example, and their professionalism and dedication to their craft are inspiring, humbling, and oblige the rest of us to be always better than our yesterday-selves.

Outside of the Computational Materials Group at Wisconsin, I would like to thank Drs George Young and Kevin Field, as well as Professor G. Robert Odette. A theorist is only as good as their data, and these three excellent scientists generously provided plenty of it, as well as critical experimental insights that kept me from wandering too far astray. I also wish to thank Professor Julie Tucker, whose friendship and guidance were invaluable during a six month appointment at the Knolls Atomic Power Laboratory. Without her help and that of Dr George Young, that would have been a fruitless enterprise indeed. I am also indebted to all the members of my oral committee, Professors Dane Morgan, J. R. Schmidt, Kumar Sridharan, Izabela Szlufarska, Xudong Wang, and Dr George Young, who generously gave significant time and energy to reviewing this dissertation and participating in my oral defense. Finally, I would like to thank Diana Rhoads. I do not believe anyone in the Materials Science Program could find their way to graduation without her constant and generous navigation.

Financial support for this research was provided by numerous sources. Principally, I would like to gratefully acknowledge personal financial support by the Rickover Fellowship Program. Additional support was provided by the DOE Nuclear Engineering Research Initiative

Consortium Program (NERIC), Award Number DE-FG07-07ID14894, as well as the DOE Nuclear Engineering University Program (NEUP) under Grant Number 10-888. Computational resources were provided in part by the National Science Foundation through Tera-Grid and XSEDE, operated by the Texas Advanced Computing Center under grant numbers TG-DMR090023 and DMR060007.

For Dawn

Contents

List of Figures and Tables

Figures

Chapter 2

Tables

Chapter 2

Chapter 3

Chapter 4

Chapter 1: Introduction

1.1 Project summary

The material integrity of the structural components of a nuclear reactor is among the most significant issues facing advancements in nuclear power technology, and is often the limiting factor for plant construction and operating costs, safety, and reactor operational lifetimes. Replacement of some components is costly, often requiring a shutdown of the reactor, and certain components such as the reactor pressure vessel are non-recoverable. A more complete understanding of the microstructural changes that occur in the reactor structural materials during service could allow for the extension of component lifetimes. Furthermore, it might open possibilities for the design of new, safer materials that could reduce operational and construction costs even further.

The discipline of computational materials science offers many tools that can be of vital assistance toward gaining this fundamental understanding. Material degradation in a nuclear reactor involves many complex atomic level phenomena, and first principles-based computational methods such as density functional theory (DFT) can offer key data and information about these phenomena that are not available by any other means. This information can then be used as a basis for atomistic simulation techniques such as Monte Carlo or molecular dynamics to explore kinetic processes that occur on the atomic scale. Finally, the results of these atomistic techniques form the foundation for higher level models that can be used to predict material structure and property changes over long time scales and wide ranges of operating conditions. Such predictions can help guide material selection during reactor design as well as choices regarding component lifetimes and possible lifetime extensions.

The goal of the research described in this document was to utilize these computational techniques to explore key modes of material degradation faced during service in nuclear power applications by Ni-Cr alloys and Fe-Cr nanostructured ferritic alloys (NFA), two of the most important structural material classes for current and future reactor designs. Specifically, the focus of this research was the study of the effects of irradiation damage on local alloy chemistry and microstructural stability at elevated temperature during very long service lifetimes. While the specific research topics were somewhat disparate in nature, the research methodology for all topics was conducted broadly using the following ground-up approach:

1. **Density functional theory calculations:** DFT was employed to calculate key atomic interactions and migration barriers for irradiation-produced defects in fcc Ni-Cr and bcc Fe-Cr. The data obtained from these calculations as then used to develop models and simulation tools to predict the effects of irradiation on local chemistry in these alloy systems. DFT was used to examine the clustering tendencies of metal-oxygen particles in NFAs. Insights gained from these calculations guided further development of higher level models for predicting the long time thermal stability of these particles. Finally, DFT calculations formed the basis of a model for understanding and predicting the order-disorder phase transformation in Ni-Cr alloys, which may dramatically impact the mechanical properties of Ni-Cr alloys during very long service lifetimes.
2. **Atomistic simulations:** Monte Carlo and molecular dynamics simulation techniques were utilized to explore the dynamics of diffusion and phase transformations on the atomic scale. These simulations provided crucial mechanistic data and insights into the processes that dominate thermal and irradiation stability.

3. **Continuum level model development:** The results of the DFT calculations and atomistic simulations formed the foundation for higher level model development. These models were used to better understand and predict the evolution of local alloy chemistry under irradiation in Ni-Cr and Fe-Cr alloys, and the long term thermal stability of Ni-Cr alloys and NFAs.

The culmination of this multiscale modeling approach has lead to a significantly improved understanding of key material degradation phenomena in Ni-Cr alloys and NFAs during service in nuclear applications.

The body of this document is organized as follows: The remainder of Chapter 1 provides additional motivation and background information regarding the specific alloys and modes of degradation that were the focus of this research, as well as a summary of key results. The following three chapters will focus on the specific technical projects conducted during the course of this research: Chapter 2 describes on the development of simulation and modeling tools for understanding and predicting radiation-induced segregation in Ni-Cr and Fe-Cr alloys. Chapter 3 describes the multi-scale modeling effort toward understanding and predicting the disorder to order phase transformation in Ni-Cr alloys. Chapter 4 presents the results of DFT calculations of clustering energetics in NFAs, and details the development of a model framework for describing the thermodynamic and kinetic aspects of oxide precipitation in said alloys. Finally, Chapter 5 presents concluding remarks, as well as ruminations on possible future research efforts.

1.2 Motivation and Background

Structural components in nuclear power systems face operating conditions that are among the most demanding of any engineering application, as the combination of high temperatures, corrosive surroundings, and exposure to large doses of radiation creates an environment that is unique in its potential to damage materials. The development and operation of safer and more efficient nuclear power systems hinges upon proper selection of materials that can withstand these harsh conditions. Two prominent material classes for these applications are Ni-Cr alloys and Fe-Cr ferritic and martensitic steels, in particular nanostructured ferritic alloys (NFAs). Alloys based on the Ni-Cr binary system demonstrate good strength and toughness at elevated temperatures, as well as excellent corrosion resistance in aqueous environments. These alloys are used extensively in light water reactors (LWR) in particular for coolant water piping. Ferritic and martensitic steels are attractive for nuclear applications due to their high strength and resistance to swelling, however creep resistance and high temperature strength are often issues of concern for these materials. A subclass of ferritic steels designed to alleviate these concerns are NFAs, which are similar to conventional high chromium ferritic and ferritic-martensitic steels except that they also contain a high density of nanometer-scale oxide particles, typically Y or Y-Ti oxides. These oxide precipitates impart remarkable creep resistance and high temperature strength [1]. Additionally, the oxide precipitates provide enhanced resistance to swelling under irradiation by suppressing the buildup of radiation-produced point defects [2]. This combination of attractive mechanical properties and irradiation damage resistance has made NFAs an attractive candidate material class for structural components for proposed fusion applications and

future advanced fission reactor designs, in particular for reactor blanket and fuel cladding applications in proposed fast reactor concepts [1].

In spite of their many advantages, both these material classes may suffer irradiation-induced degradation of mechanical properties during operation. Both alloy types utilize large amounts of Cr, partially to enhance corrosion resistance. However, radiation is known to cause significant changes to alloy composition near microstructural features such as grain boundaries, voids, and other interfaces through a phenomenon known as radiation-induced segregation (RIS) [3]. Significant alteration of alloy chemistry in particular near grain boundaries could impact the local corrosion resistance and ultimately lead to risk of irradiation assisted stress corrosion cracking (IASCC) in these alloys [4, 5]. RIS may additionally lead to local phase instabilities where unexpected secondary phases may appear due to compositional changes, such as the precipitation of Cr-rich α` phase in NFAs [6]. Understanding and predicting RIS in these alloys is therefore crucial for determining safe operating conditions and lifetimes.

Even without the special considerations of irradiation conditions, both of these alloys may exhibit thermally-induced microstructural instabilities on the decades-long time scales of nuclear reactor lifetimes. The Ni-Cr alloy system exhibits an ordered phase at the stoichiometry Ni_2Cr, however in all engineering alloy grades the fcc matrix phase is a single phase solid solution. Alloys near this composition may therefore undergo a disorder to order phase transformation, which can have unexpected and dramatic effects on mechanical properties. NFAs do not typically exhibit a similar phase transformation, however they are still subject to risk of thermally activated microstructural degradation. Both the mechanical properties and irradiation damage resistance of NFAs rely upon the high density dispersion of nanometerscale

oxide particles. During very long service at high temperature these particles may begin to coarsen, increasing in their mean size and decreasing in number density. Excessive coarsening of these precipitates would lead to a dramatic loss of creep resistance and high temperature strength [7, 8]. These thermal degradation effects are readily observable at very high temperatures, but at nuclear reactor operating temperatures, these phenomena might take decades to manifest. It is therefore not practical or even feasible to fully explore these processes through direct experimental measurements. Some kind of model will be necessary to make predictions about material property changes on the timescale of nuclear reactor lifetimes. The development of such models was the primary objective of this research, and was accomplished during the course of three distinct research projects. These projects are specified in the following subsection.

1.3 Descriptions and key results of research projects

The research described in this document was pursued as three distinct but related research projects. A brief description and key results of these projects are provided below:

1. **Theory and prediction of radiation induced segregation in Ni-Cr and Fe-Cr alloys:** In this project, DFT calculations, molecular dynamics simulations, and diffusion theory were combined to produce a fully *ab initio* model of RIS for the first time. Key results include the identification of underlying RIS mechanisms in Ni-Cr and Fe-Cr alloys, related in particular to the diffusion of self-interstitial defects.
2. **Atomistic modeling of the order-disorder phase transformation in Ni-Cr alloys:** The goal of this project was to develop a model for estimating the timescale of the disorder to order phase transformation in Ni-Cr alloys, based upon Monte Carlo simulation

techniques. This effort yielded a simple, novel model that accurately describes ordering kinetics in the Monte Carlo simulations and can closely reproduce experimental data, with reasonable physical parameters. The predictions of this model indicate that the disorder-order phase transformation may be of concern under LWR operating conditions, particularly on the timescales of proposed reactor life extensions.

3. **Thermodynamic and kinetic modeling of oxide precipitation in nanostructured ferritic alloys:** This project focused on combining DFT calculations and available thermodynamic and kinetic data to examine oxide nucleation and growth phenomena in NFAs. Important results of this project include new insights into oxide nanoprecipitate nucleation, coarsening mechanisms, and alloy composition optimization.

The subsequent three chapters will describe the background, technical approaches, and results of these three projects in detail.

Chapter 2: Theory and prediction of radiation induced segregation in Ni-Cr and Fe-Cr alloys

2.1 Introduction and background

Radiation induced segregation is a microstructural process that occurs under radiation whereby an initially homogenous alloy will become strongly segregated near microstructural features such as grain boundaries, voids, or second-phase particles [3, 9]. The root cause of this phenomenon is the diffusion of radiation-produced atomic defects to these features, which act as defect sinks. One result of this flux of defects toward defect sinks is the depletion of some alloy components and enrichment of others in the neighborhood of those sinks, with respect to their initial pre-irradiation concentrations. A typical example of RIS behavior is illustrated in Fig. 2.1,

which depicts the measured concentration profiles near a grain boundary in an Fe-20Cr-25Ni alloy irradiated via neutrons [3]. Significant alloy segregation is observed near the grain boundary.

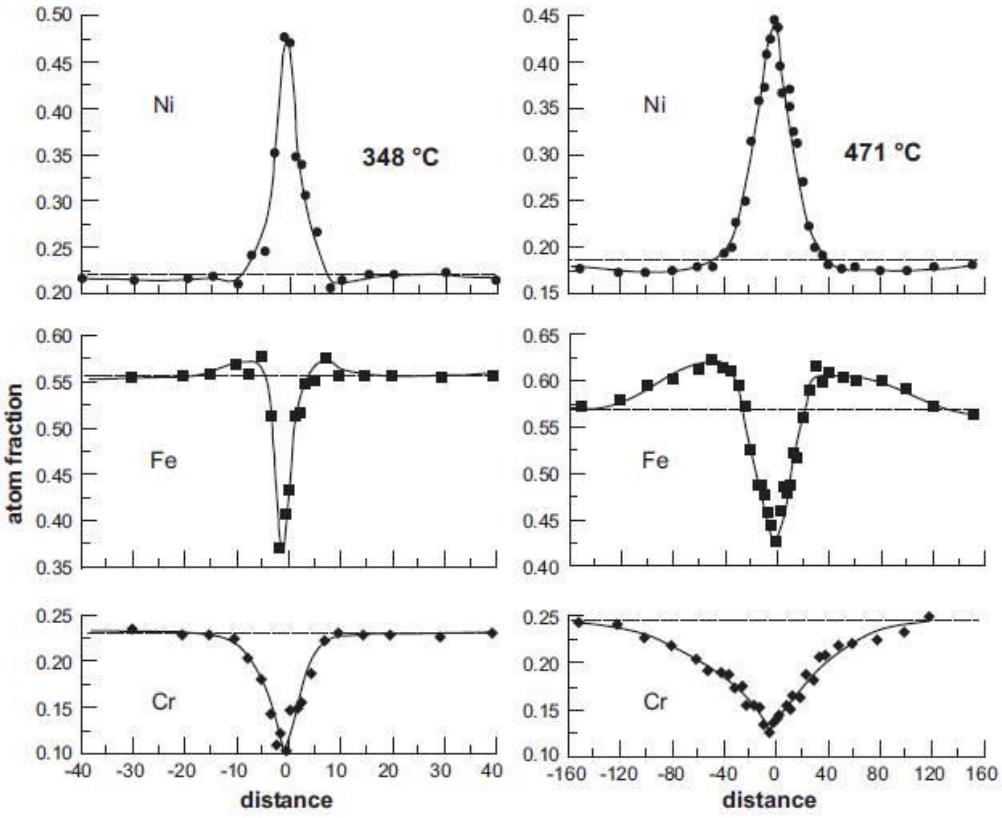

Figure 2.1: RIS profiles in an Fe-20Cr-25Ni alloy irradiated to 1.4 dpa at 348 °C (left) and 4.7 dpa at 471 °C (right) via neutrons. From [3].

RIS is of particular concern in Cr containing alloys such as the Ni-Cr based alloys or high Cr NFAs, both of which are used in modern light water reactors or are candidate materials for future reactor designs [9, 10]. Cr is added to these alloys in part to provide corrosion resistance and in Ni-Cr alloys, experimental results indicate that RIS causes Cr to be depleted near grain boundaries and surface [11], regions where metals are most susceptible to corrosive attack. Corrosion of metallic components in a nuclear power system can lead to failure by a mechanism

known as irradiation assisted stress corrosion cracking (IASCC) [9, 12], and it is believed that RIS plays an important role in the susceptibility of Ni alloys to IASCC [9, 13, 14]. In contrast, RIS appears to cause Cr enrichment in Fe-Cr ferritic steels like NFAs [15, 16]. While corrosion is not therefore the primary concern with respect to RIS in this system, enrichment of Cr could lead to local phase separation of the Cr-rich phase α', causing embrittlement. A simulation tool that can accurately predict RIS would therefore be valuable for material and reactor design, and potentially for preventative maintenance in existing reactors as well. An additional motivation for studying RIS is that it gives fundamental insights into the nature of point defect mobility, which are at the foundation many aspects of alloy microstructural evolution in nuclear materials.

Many models have been developed to simulate Cr RIS in steels, and most are based on a rate theory approach pioneered by Wiedersich et al. [17] that numerically solves the coupled diffusion equations of radiation produced defects and alloy components. An early influential model was developed by Perks *et al* [18] that presumes that RIS occurs due to preferential vacancy migration with one alloy component relative to the others. In this model, as radiation produced vacancies migrate toward a defect sink, they cause a corresponding net flux of this alloy component away from the defect sink, resulting in depletion of this component in the neighborhood of the sink. This process is the vacancy driven component of the inverse Kirkendall effect. The Perks model also assumes that there is no preferential interstitial migration, thus as radiation produced interstitials migrate toward a defect sink, they carry no net flux of any one alloy component and do not alter the alloy composition near the sink. The most important input parameters for the Perks model are therefore the vacancy diffusivities and compositions for each of the species in the alloy, as these are the parameters that determine

which components are enriched or depleted near defect sinks due to RIS. When properly parameterized, such a model can predict RIS with reasonable accuracy at low and intermediate temperatures; however it is less successful at higher temperatures. An important modification was introduced to this model by Grandjean *et al* [19] and developed in detail for the Fe-Ni-Cr alloy system by Allen *et al* [20], resulting in the modified inverse Kirkendall model (MIK). This model refines the Perks model by including the effects of local composition on the diffusivities of the alloy species. Compared to the Perks model, the MIK model provides greater fidelity with experimental results, particularly at elevated temperatures and over a much wider range of alloy base compositions. The model parameters used in the MIK model are obtained via fitting to experimental energies and diffusion data, as well as RIS data.

Both the Perks and MIK models were developed and parameterized for fcc based Fe-Ni-Cr alloys, and similar models have been developed to include other species with success [21]. The success of these models demonstrates the robustness and adaptability of this rate theory approach, given suitable input parameters. However, obtaining input parameters from experimental fitting limits the applicability of such models to cases where adequate data is available. Furthermore, the assumption that RIS is determined by only the vacancy diffusivities of the alloy species potentially distorts the physics of the true system, as the interstitial diffusivities of components in an alloy could be very different and potentially play an important role in RIS [22]. Nastar *et al* [23] developed a model for RIS in Fe-Ni-Cr alloys that contains additional mechanisms and different parameterizations than the MIK model. First, unlike the MIK model, all the parameters for vacancy diffusion were fit to thermodynamic and diffusion data, and not directly to any RIS data. Contrary to the MIK model, Nastar *et al* then found it was

necessary to include the contribution of interstitial diffusion to RIS to reproduce experimentally measured segregation. Due to the lack of experimental interstitial diffusion data in Fe-Ni-Cr alloys, the interstitial diffusion parameters in the model of Nastar *et al* are obtained via fitting to RIS data. Nastar *et al's* model appears to perform approximately as well as the MIK model in matching RIS data for Fe-Ni-Cr alloys. The MIK model and the model of Nastar *et al* thus demonstrate that multiple interpretations of the underlying physics of RIS can result in different models that are equally capable of predicting RIS. Because both models rely to some extent on fitting to RIS data, their capability of accurately modeling RIS data is in itself not sufficient to demonstrate that either model captures the true parameter values or even dominant physical mechanisms of RIS. In this work we explore how ab initio density functional theory (DFT) approaches can help clarify the parameter values and mechanisms relevant for RIS in steels.

DFT is a tool that may be used to determine many parameters needed for modeling both vacancy and interstitial diffusion with excellent precision [22, 24]. It is possible to develop a RIS model based upon DFT calculations that includes the effects of both interstitial and vacancy diffusion without obtaining parameters from experiments. Such a model may therefore provide new insights or independent corroboration of earlier RIS models that are based on fitting to experimental data. In this study, a versatile model is developed for simulating RIS that is adaptable to general thermodynamic and kinetic frameworks. This model is parameterized exclusively using the DFT-based diffusion parameters of Tucker *et al* [22] for the Ni-Cr system and Choudhury et al. for the Fe-Cr system [24]. Through the use of ab initio parameterization we can avoid *a priori* assumptions regarding the mechanism of RIS. The resulting model is then

used to assess the current physical descriptions of RIS, in particular with respect to current assumptions regarding the role of interstitials.

2.2 Rate theory model for simulating RIS

The rate theory RIS model is based on solving the following set of coupled equations to obtain 1-dimensional concentration profiles for each of the species in the irradiated binary A-B alloy system: A atoms, B atoms, single vacancies, and single interstitials [9, 17, 25].

$$\begin{aligned} \frac{dC_m}{dt} &= -\frac{dJ_m}{dx} \\ \frac{dC_d}{dt} &= \varepsilon K_0 - R_{iv} C_{Vac} C_{Int} - \frac{dJ_d}{dx} \end{aligned} \tag{2.1}$$

In the above, *m* refers to metallic species A or B, and *d* refers to defect species vacancies or interstitials. C_i is the site fraction of species *i*, J_i is the flux of species *i*, R_{iv} is the rate coefficient for recombination of vacancies and interstitials, K_0 is the radiation dose rate in dpa and ε is the damage efficiency. Throughout this study, we will assume an efficiency of 20%, consistent with 3.2 MeV protons [9]. The radius of recombination is taken to be equal to the first nn distance. The fluxes J_i are evaluated using the following equations [26]

$$\begin{aligned} J_m &= -\sum_{d=Int,Vac} \sum_{n=A,B} L_{mn}^{d} \frac{d\tilde{\mu}_{nd}}{dx} \\ J_{Vac} &= \sum_{m=A,B} \sum_{n=A,B} L_{mn}^{Vac} \frac{d\tilde{\mu}_{nVac}}{dx} \\ J_{Int} &= -\sum_{m=A,B} \sum_{n=A,B} L_{mn}^{Int} \frac{d\tilde{\mu}_{nInt}}{dx} \end{aligned} \tag{2.2}$$

where L_{mn}^{d} is the phenomenological coefficient relating the flux of species *m* to a driving force acting on species *n* through diffusion mediated by defect species *d*. The driving forces for diffusion are written here as the gradient in diffusion potentials [26, 27], defined as

$$\begin{aligned} \tilde{\mu}_{mVac} &= \mu_m - \mu_{Vac} \\ \tilde{\mu}_{mInt} &= \mu_m + \mu_{Int} \end{aligned} \tag{2.3}$$

where μ_i is the chemical potential of species *i*.

We apply the above set of equations to a physical system that consists of a one dimensional, semi-infinite metal crystal with an ideal free surface on one side, which acts as a sink for the radiation induced vacancies and interstitials, emulating a grain boundary. To treat this system numerically, we discretize the system into lattice planes and evaluate the site fraction of each species in each lattice plane. The gradients of fluxes and diffusion potentials in Eqns. 2.1 and 2.2 then become finite difference equations, as follows:

$$\begin{aligned} \frac{dJ_i^n}{dx} &= -\left[\frac{J_i^{n+1} - J_i^n}{\Delta x}\right] \\ \frac{d\tilde{\mu}_{md}^n}{dx} &= \left[\frac{\tilde{\mu}_{md}^n - \tilde{\mu}_{md}^{n-1}}{\Delta x}\right] \end{aligned} \tag{2.4}$$

where $\tilde{\mu}_i^n$ is the diffusion potential of species *i* in plane *n*, J_i^n is the flux of species *i* between plane *n-1* and *n*, and Δx is the interplanar distance between adjacent close packed planes in the crystal.

We solve the resulting set of finite difference equations subject to the following set of boundary conditions [17]. Plane 1 of the system is the first lattice plane and is modeled as an

ideal flat surface that cannot exchange atoms with the adjacent vacuum, which places the following constraint on the metallic species in the first plane:

$$J_m^1 = 0 \tag{2.5}$$

The surface is modeled as an ideal defect sink, which maintains the concentration of vacancies and interstitials in plane 1 at their thermodynamic equilibrium values. This imparts the following condition on defect species in the first plane:

$$\frac{dC_d^1}{dt} = 0 \tag{2.6}$$

The last plane in the system is considered to be in the center of the symmetric system, far enough from the surface that concentration gradients are zero, and is treated with a mirror boundary condition:

$$J_i^{n_{\max}} = 0 \tag{2.7}$$

For the initial condition of the system, we set the concentration of the vacancies and interstitials in all planes equal to their bulk thermal equilibrium concentrations as determined by DFT calculations [24, 28], and we set the Ni and Cr concentrations equal to their nominal alloy compositions. We then evolve the system in time using a modified implicit multistep Newton method, implemented using the DLSODE solver package [29].

The thermodynamic components of the model equations are contained within the chemical potential terms μ_i. Following the derivation of Lupis [30] it is possible to derive a set of chemical potentials for each species in the system from an arbitrary expression of the Gibbs free energy, provided that it is a function only of the composition of the system. For the system of A, B, vacancies, and interstitials, the resulting expressions are

$$\mu_A = G_m - \sum_{i=B,Int,Vac} C_i \frac{\partial G_m}{\partial C_i}$$
$$\mu_i\big|_{i=B,Int,Vac} = G_m + \sum_{j=B,Int,Vac} (\delta_{ij} - C_i) \frac{\partial G_m}{\partial C_i} \quad (2.8)$$

where G_m is the partial molar Gibbs free energy of the system and δ_{ij} is the Kronecker delta. For this study, we will utilize the following expression for the free energy:

$$G_m = C_{Cr}C_{Vac}W_{CrVac} + C_{Cr}C_{Int}W_{CrInt} + C_{Vac}E_{Vac} + C_{Int}E_{Int} + k_bT\sum_i C_i \ln C_i \quad (2.9)$$

where C_i is the mole fraction of species i, E_i is the formation energy of defect species i, W_{ij} is the 1st nn interaction parameter of species i and j. E_i and W_{ij} are calculated by DFT [22, 24, 31]. This thermodynamic model is consistent with the calculation of the dilute alloy tracer diffusion coefficients as determined by Tucker [22] and Choudhury [24], which include the effects of Cr-vacancy and Cr-interstitial binding.

The diffusion kinetics of the model system are contained in the phenomenological coefficients L^d_{mn}. To determine values of L^d_{mn} from the DFT-based tracer diffusion coefficients calculated by Tucker and Choudhury, we utilize a method for approximating the phenomenological coefficients as a function of composition provided by the Manning random alloy theory [32]. This approach was derived for systems which may be approximated as random solid solutions, and should be appropriate for Ni-Cr and Fe-Cr alloys in the temperature range of interest to RIS. Based on the Manning model the concentration dependent phenomenological coefficients can be expressed in terms of the tracer diffusion coefficients (assumed constant with composition) as:

$$L_{ii} = \left(\frac{C_i d_i^*}{k_b T}\right)\left(1 + \frac{(1-f_0)}{f_0}\frac{C_i d_i^*}{\sum_m C_m d_m^*}\right)$$
$$L_{ij} = L_{ji} = \frac{(1-f_0)}{f_0}\left(\frac{C_i C_j d_i^* d_j^*}{k_b T \sum_m C_m d_m^*}\right) \quad (2.10)$$

where C_i is the concentration of species *i*, f_0 is a correlation factor for diffusion, and d_i^* is the tracer diffusion coefficient of species *i* as calculated by the DFT-based methods detailed in [22] and [24]. Although Eqns. 2.10 were derived for vacancy diffusion, a very similar derivation for interstitial diffusion is provided in [33]. The resulting expressions are identical to Eqns. 2.10, except that the interstitial tracer diffusivities from and the interstitial correlation factor are used instead of the vacancy counterparts.

The use of composition-independent diffusion coefficients places this model at a similar level of approximation as the Perks model. While the MIK model showed a clear improvement in accuracy through the inclusion of compositional dependence in the diffusion coefficients, Perks *et al* demonstrated that a model based on diffusion coefficients that are constant with respect to composition could qualitatively capture RIS phenomena in many austenitic alloys reasonable well. The MIK model demonstrated that composition-dependent diffusion coefficients are essential for accurately simulating RIS in austenitic alloys across varying base alloy compositions with a single set of parameters. Neglecting these compositional effects by using compositionally-independent d_i^* values in Eqns. 2.10 will therefore limit the applicability of this DFT-based model with respect to the MIK model or other composition dependent models, e.g., the model of Nastar *et al* [23].

To simulate RIS, we use the chemical potentials provided by Eqns. 2.8 and the phenomenological coefficients provided by Eqns. 2.10 to parameterize the flux equations 2.2. We then use these flux equations to solve the rate equations 2.1 according to the finite difference method and boundary conditions provided in Eqns. 2.4-2.7.

2.3 Qualitative RIS predictions based upon tracer diffusivities

While the numerical solution of Eqns. 2.1 is necessary to make quantitative RIS predictions, qualitative RIS predictions such as the sign of the segregation for a given species in a binary alloy may be determined by analysis of the interstitial and vacancy tracer diffusivities of the alloy species. In conventional Weidersich-type models [17], qualitative RIS behavior is controlled by the ratios of the interstitial and vacancy diffusivities of the alloy species according to the following proportionality:

$$\Delta C_A \propto \frac{d_{iA}}{d_{iB}} - \frac{d_{vA}}{d_{vB}} \tag{2.11}$$

where ΔC_A is the difference in concentration of species A at the grain boundary relative to the nominal alloy concentration, and d_{ks} is the diffusivity of species *s* via defect type *k*. Fig. 2.2 depicts the diffusivity ratios in the Fe-Cr and Ni-Cr alloy system, as calculated by DFT [22, 24].

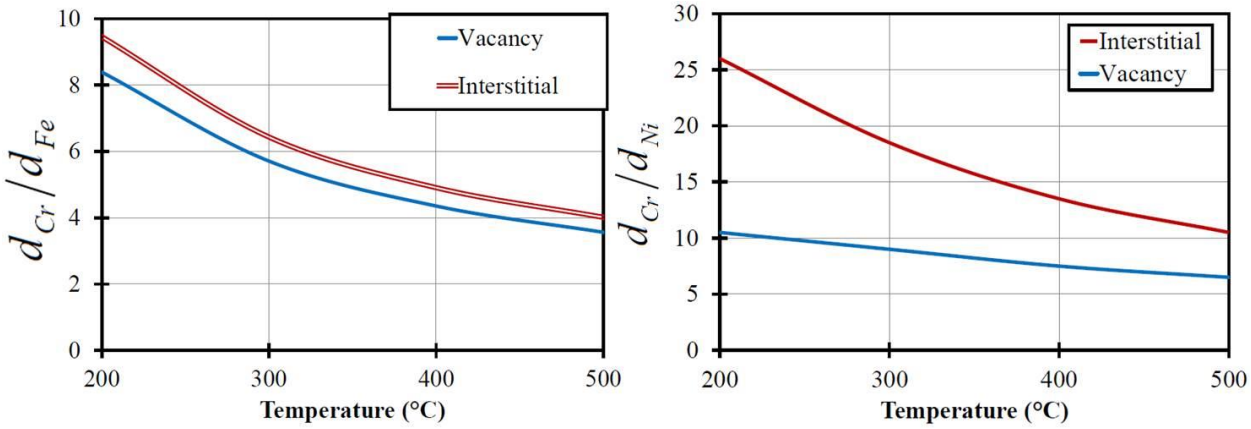

Figure 2.2: Interstitial and vacancy diffusivity ratios in Fe-Cr (left) and Ni-Cr (right), as determined via DFT calculations [22, 24].

From Fig. 2.2 and Eqn. 2.11, it is evident that the DFT-based tracer diffusivities predict that RIS will tend to cause Cr enrichment in both Fe-Cr and Ni-Cr, driven by faster interstitial diffusion of Cr with respect to the solute species (Fe or Ni). Furthermore, based on the large differences between the diffusivity ratios, the effect is likely to be stronger in Ni-Cr leading to more dramatic segregation. This qualitative prediction contradicts the conventional RIS description, which typically neglects the effects of interstitial diffusion as unimportant.

2.4 DFT-based RIS model predictions in the Fe-Cr alloy system

In order to validate the model for RIS in Fe-Cr, RIS was examined in an Fe-9Cr model alloy, irradiated with protons at 400 and 500 °C. Experimental data was collected by Field et al. [15]. In the irradiated materials examined by Field et al., it was observed that the RIS profiles at grain boundaries were highly sensitive to the misorientation angle of the boundary. Based upon this observation, the boundary condition of the basic DFT-based RIS model was altered according to the model of Duh et al. [34] to capture this dependence. This alteration will be described in the following subsection.

2.4.1 Modification of the basic model to capture grain boundary angle dependence of RIS

The key difference between the basic model described in Sec. 2.2 and the one implemented here is the treatment of the sink boundary condition. In the basic model, and in most other RIS models of this type, the sink is treated as an ideal sink, which allows vacancies and interstitials to be instantly annihilated when they arrive at the sink. This maintains a defect concentration near the sink that is equal to the thermodynamic equilibrium concentration in the bulk. With the modification discussed in this section, an alternative boundary condition developed by Duh et al [34], which treats the boundary as a grain boundary with a sink efficiency that is function of grain boundary misorientation angle, was utilized. The boundary condition alters the sink efficiency where a higher general misorientation angle leads to a higher sink strength, while low angles and misorientations near high angle coincident site lattice (CSL) boundaries have a lower sink efficiency. The flux of defects from the first crystal plane into the grain boundary is modeled explicitly and consequently the concentration of defects near the sink is not constrained to be equal to the thermodynamic equilibrium value. While the model of Duh et al. was formulated to treat RIS in FCC Fe-Ni-Cr alloys, with the appropriate selection of parameters it has been adapted to the BCC Fe-Cr system. Values all necessary physical constants for simulating RIS in the Fe-9Cr model alloy are provided in Table 1.

Table 2.1: Physical parameters used in the Fe-Cr RIS model. Diffusion parameters obtained from an Arrhenius fit to the values calculated by Choudhury et al. [24] from first principles.

Basic RIS model parameters			
Parameter	Notation	Value	Ref.
Pre-exponential factor for Fe interstitial diffusivity	$d_{0,Fe}^{Int}$	6.59 x10^{-7} m^2/sec	[24]
Pre-exponential factor for Cr interstitial diffusivity	$d_{0,Cr}^{Int}$	6.85 x10^{-7} m^2/sec	[24]
Pre-exponential factor for Fe vacancy diffusivity	$d_{0,Fe}^{Vac}$	5.92 x10^{-6} m^2/sec	[24]
Pre-exponential factor for Cr vacancy diffusivity	$d_{0,Cr}^{Vac}$	5.46 x10^{-6} m^2/sec	[24]
Activation energy for Fe interstitial diffusivity	$E_a^{Fe,Int}$	0.36 eV	[24]
Activation energy for Cr interstitial diffusivity	$E_a^{Cr,Int}$	0.27 eV	[24]
Activation energy for Fe vacancy diffusivity	$E_a^{Fe,Vac}$	0.77 eV	[24]
Activation energy for Cr vacancy diffusivity	$E_a^{Cr,Vac}$	0.68 eV	[24]
Dislocation density	ρ_d	5 x10^{13} m^{-2}	[15]
Grain boundary model parameters			
Grain boundary attempt frequency	ν_0	5.00 x10^{12} sec^{-1}	[24]
Burgers vector	b	2.48 x10^{-10} m	[15]
Shear strength	μ	86.0 GPa	[35]
Poisson's ratio	ν	0.3	[35]
Grain boundary correlation factor	f_{Int}^{gb}, f_{Vac}^{gb}	0.5	[34]

Under this modified boundary condition, the rate of annihilation of defects at the sink boundary is proportional to the flux of defects into the grain boundary and the density of defect annihilation sites on the boundary. The flux of defects into the grain boundary is determined by an approximate defect grain boundary diffusion coefficient defined by the following expression (where d = vacancy or interstitial):

$$d_d^{GB} = g_d a^2 Z f_d^{gb} \nu_0 \sum_k C_k \exp\left(-\frac{(E_a^{k,d} - a^2\gamma)}{k_b T}\right) \tag{2.12}$$

where g_d is a dimensionless constant which we take to be equal to 1, a is the lattice parameter, Z is the bcc coordination number, f_d^{gb} is the correlation factor for defect type *d* in the grain boundary, v_0 is the attempt frequency, and γ is the specific grain boundary energy. In a multicomponent system C_k is the fraction of component *k* near the boundary and $E_a^{k,d}$ is the migration activation energy of component *k* for defect type *d*. For the parameters g_d and f_d^{gb} we use approximate values of 1 and 0.5. respectively, as their impact on the model results is very minor.

From Eqn. 2.12 it is evident that as grain boundary energy increases, the grain boundary diffusion coefficient increases exponentially. Therefore, for very high energy grain boundaries the flux of defects into the grain boundary is sufficiently fast that the boundary condition approaches ideal sink behavior. In order to study RIS behavior as a function of grain boundary angle, it is necessary to cast the grain boundary energy term in Eqn. 2.12 in terms of grain boundary angle. This is accomplished by the grain boundary theory of Read and Shockley [36]. Details and final expressions for grain boundary energy of low angle grain boundaries, high angle grain boundaries, and special CSL boundaries can be found in [15].

2.4.2 Comparison of model results to experimental measurements

Fig. 2.3 depicts the grain boundary Cr concentration in the Fe-9Cr model alloy irradiated at 400 °C to 3 dpa with protons as a function of grain boundary angle. The dashed line corresponds to the DFT-based RIS model prediction, and the solid symbols are the experimental measurements [15].

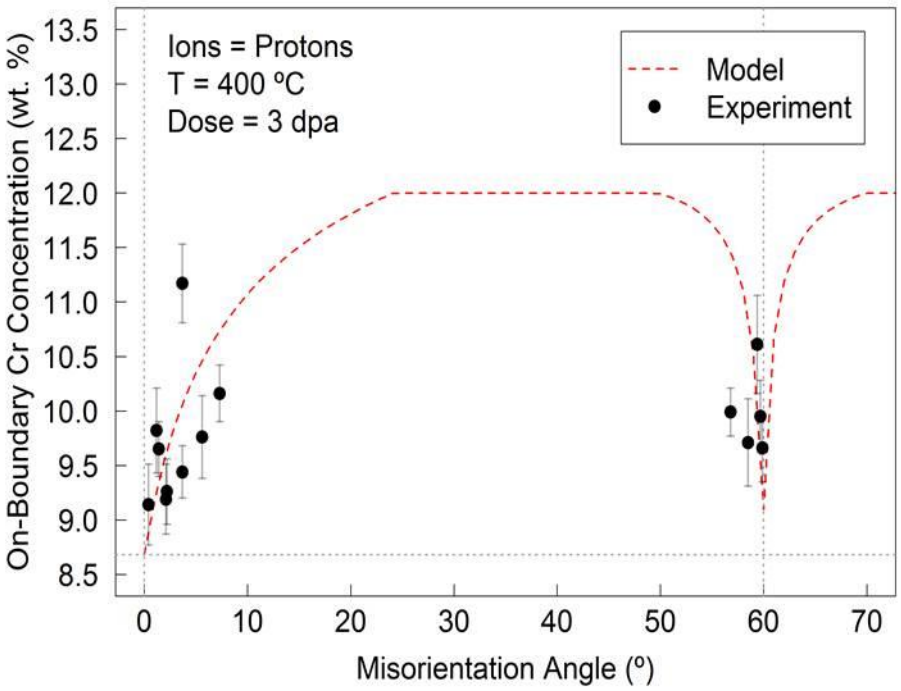

Figure 2.3: Grain boundary Cr concentration in the irradiated Fe-9Cr model alloy, as a function of grain boundary angle. The DFT-based RIS model predictions are represented by the dashed line, and the solid symbols represent experimental measurements. From [15].

While some quantitative discrepancies exist between the model predictions and the experimental measurements, the qualitative trends of Cr segregation with boundary angle are well captured. In Fig. 2.4, Cr profiles are depicted for two boundaries for which the predicted and measured Cr concentration were in good agreement.

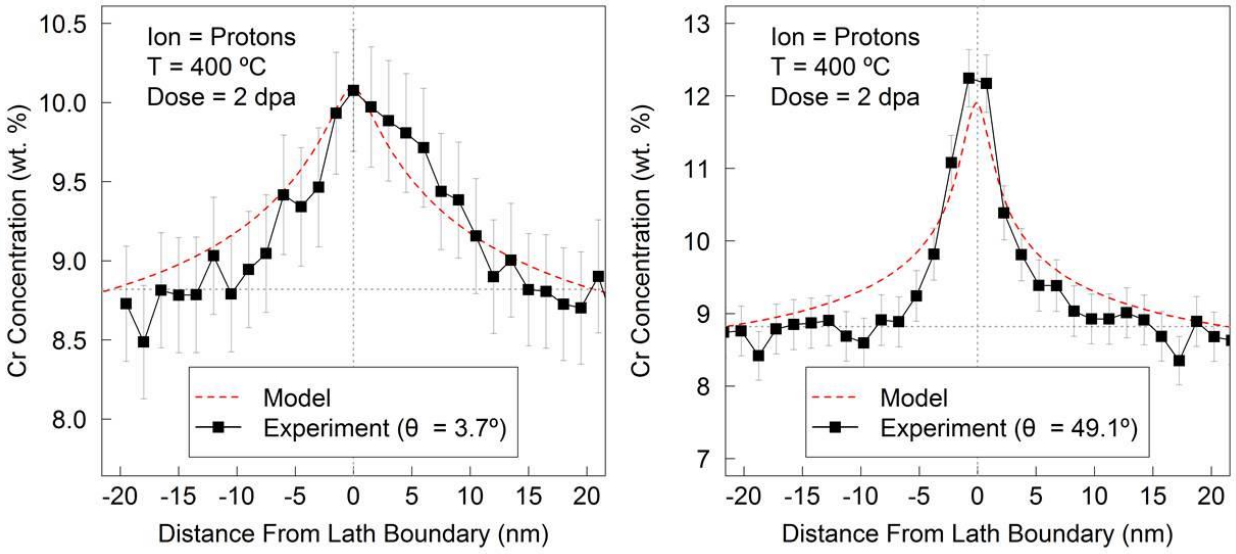

Figure 2.4: Cr concentration profiles near low and high angle boundaries after irradiation at 400 °C to 2 dpa. Dashed red lines illustrate the Cr concentration profiles predicted by the DFT-based RIS model, and the solid symbols represent experimental measurements. From [15].

The shapes of the concentration profiles for the low and high angle boundaries in Fig. 2.4 show excellent agreement. A limited exploration of the temperature dependence of RIS in Fe-9Cr was performed by Field et al. as well [15]. Fig. 2.5 presents the predicted and measured Cr concentration profiles for low angle grain boundaries in the Fe-9Cr alloy irradiated at 400 and 500 °C.

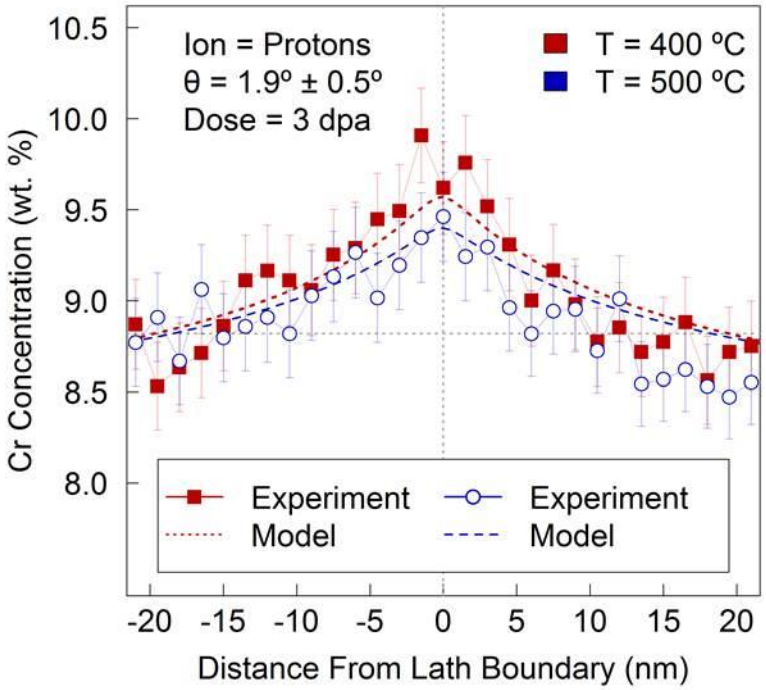

Figure 2.5: Cr concentration profiles on a 1.9° ± 0.5° boundary in the Fe-9Cr alloy irradiated at 400 and 500 °C to 3 dpa. Model predictions are illustrated by the dashed lines, while symbol represent experimental measurements. From [15].

From both the model predictions and the experimental measurements in Fig. 2.5, RIS appears to be slightly reduced at 500 °C with respect to 400 °C. In the model, this is due to an increase in the thermal equilibrium vacancy concentration at 500 °C compared to 400 °C: at high temperatures, the equilibrium vacancy concentration begins to overtake the radiation-induced vacancy concentration, at which point the vacancy concentration gradient near the grain boundaries starts to disappear. Without this defect gradient, any large local fluctuations in alloy composition are quickly dispersed and RIS begins to disappear.

According to all model predictions and experimental measurements, RIS appears to cause Cr enrichment in the Fe-9Cr model alloy. This is in general agreement with most previous RIS studies in this material system [6, 16]. Based on Fig. 2.2, this Cr enrichment in the model is

driven by fast Cr interstitial diffusion with respect to Fe. This is substantial evidence that interstitial diffusion plays an important role in RIS in Fe-Cr, and calls into question the assumption, made without basis, that interstitial diffusion plays no important role in RIS in Ni-Cr and Fe-Ni-Cr alloys [20, 37].

The Cr enrichment predicted by the model and observed in experiment is rather modest, never exceeding about 3 wt%. However, the phase boundary for α-α' decomposition in RIS has been located at around 10 wt% Cr at 400 °C [38]. Therefore, even if it is not very severe, a local enrichment of 3 wt% Cr due to RIS could drive this phase transformation in alloys near the Fe-9Cr composition.

2.5 DFT-based RIS model predictions in the Ni-Cr alloy system

This section examines the results of applying the DFT-based RIS model to the Ni-Cr alloy system. Model results are compared to experimental measurements of RIS in the Ni-18Cr model alloy.

2.5.1 Basic RIS model predictions in the Ni-18Cr model alloy

Fig. 2.6 depicts the simulated RIS concentration profiles for a Ni-18Cr model alloy irradiated to 0.5 dpa at temperatures in the range of 473 – 773 K. The model predicts Cr enrichment at all temperatures, contrary to experimental results for this alloy [11].

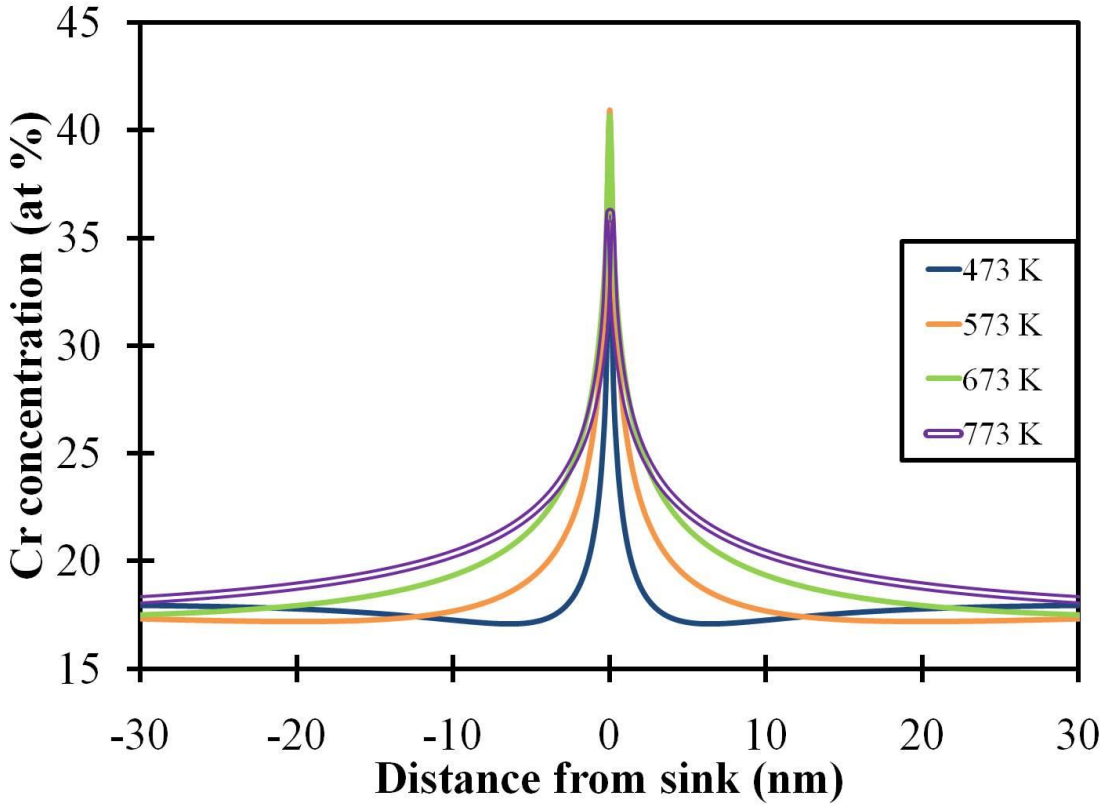

Figure 2.6: Cr concentration profiles near a grain boundary predicted by the DFT-based RIS model in an irradiated Ni-18Cr alloy.

Fig. 2.7 depicts Cr segregation as a function of dose and temperature, as well as experimental results [11]. For these and all other figures, Cr segregation is defined as the difference between the concentration at the sink and the nominal alloy concentration, where a positive value indicates enrichment and a negative value indicates depletion. The Cr sink concentration is defined as the average Cr concentration in a 2 nm region about the sink. This value differs from the Cr concentration in the sink plane by 1-2% and is intended to provide an approximation of the finite measurement width effects that occur in experimental RIS measurements by STEM or AES [39].

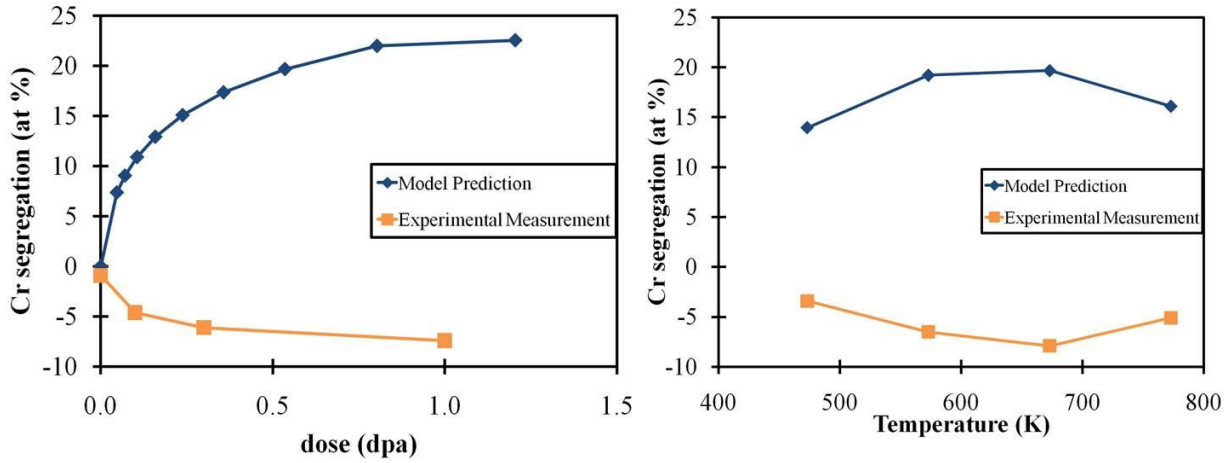

Figure 2.7: RIS model predictions and experimental measurements [11] of Cr segregation in a Ni-18Cr alloy. The left figure depicts Cr segregation as a function of dose at 673 K , while the figure on the right depicts Cr segregation as a function of irradiation temperature at after a dose of 0.5 dpa.

With this RIS model certain features of the RIS phenomenon are accurately captured, such as steady state dose and maximum RIS temperature, however the sign of the predicted segregation does not agree with experimental measurement.

In the Ni-18Cr alloy, the RIS model erroneously predicts Cr enrichment. According to Fig. 2.2, this result is due to the dominance of fast Cr interstitial diffusion in the model. The relative contributions of vacancies and interstitials may be clarified by investigating the effects of interstitial and vacancy diffusion on RIS in the Ni-18Cr alloy separately. The effect of one type of defect may be isolated by setting the Ni and Cr diffusivities of the other type of defect equal to one another. For example, to isolate the effect of interstitial diffusion on RIS, we set d_{Cr}^{*Vac} equal to d_{Ni}^{*Vac} (or equivalently, $d_{Cr}^{*Vac} / d_{Ni}^{*Vac} = 1$). An analogous operation is performed to isolate the effect of vacancy diffusion. Fig. 2.8 depicts the Cr concentration profiles at 673 K and 0.5 dpa produced by the isolated mechanisms of interstitial and vacancy diffusion, as well as the profile produced by their aggregate effects.

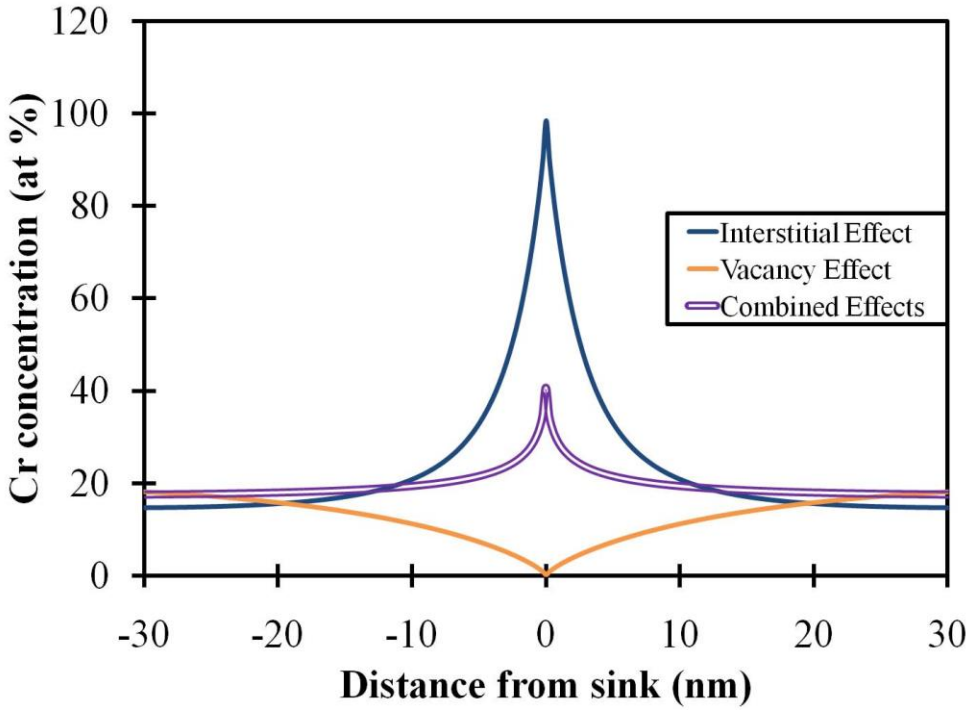

Figure 2.8: Model predicted Cr profiles at 0.5 dpa and 673 K for the isolated effects of interstitial and vacancy diffusion, as well as their combined effect.

Vacancy diffusion clearly leads to Cr depletion, while interstitial diffusion causes Cr enrichment. When their effects are combined, interstitial diffusion dominates and results in overall Cr enrichment in this set of model calculations.

Fast Cr diffusion by vacancies is often cited as the dominating effect that causes Cr depletion during RIS in fcc Ni and Fe alloys [18, 20], and adjusting the ratio $d_{Cr}^{*Int} / d_{Ni}^{*Int}$ to be equal to 1 produces the RIS profile that results from vacancy diffusion alone. However, it is evident from Fig. 2.8 that invoking the vacancy effect alone in the DFT-based model results in complete Cr depletion at the sink, whereas much milder Cr depletion is observed experimentally [11].

The DFT-based RIS model presented here produces qualitatively inaccurate RIS predictions, and we have considered possible sources of this significant discrepancy. First, we

investigated the potential role of errors in the DFT calculations used to determine the Cr vacancy and interstitial diffusivities used in the model (the diffusion energetics for Ni seem to agree well with experiments [22] so we focus on possible errors associated with Cr). In the multifrequency approach used in [22], both d_{Cr}^{*Int} and d_{Cr}^{*Vac} are functions of several distinct migration barriers. To determine whether errors in the determination of these migration barriers can fully account for the discrepancy between model prediction and experimental measurement, we selected four of the vacancy migration frequencies (following the conventions of [22] denoted w_1, w_2, w_3, w_4) and four of the interstitial migration frequencies (w_R, w_I, w_3, w_2') and treated their associated migration barriers as adjustable parameters. These barriers were selected because they were found to have the most significant impact on the Cr vacancy and interstitial diffusivities. We then fit these barriers through a least-squares optimization of the difference between the model results and the experimental Cr segregation measurements at 473 K, 573 K, 673 K, and 773 K [11], using the original DFT values from[22] as the initial guesses for these parameters. As we are fitting eight parameters with only four data points, the resulting fit will likely not be unique. However, by using the DFT values as initial guesses, we can determine how much these barriers would need to change to bring the model into agreement with experiment, and whether this change is within the expected error of the DFT calculations from [22].

Fig. 2.9 depicts experimentally measured Cr segregation as a function of temperature as well as the results of the best-fit model.

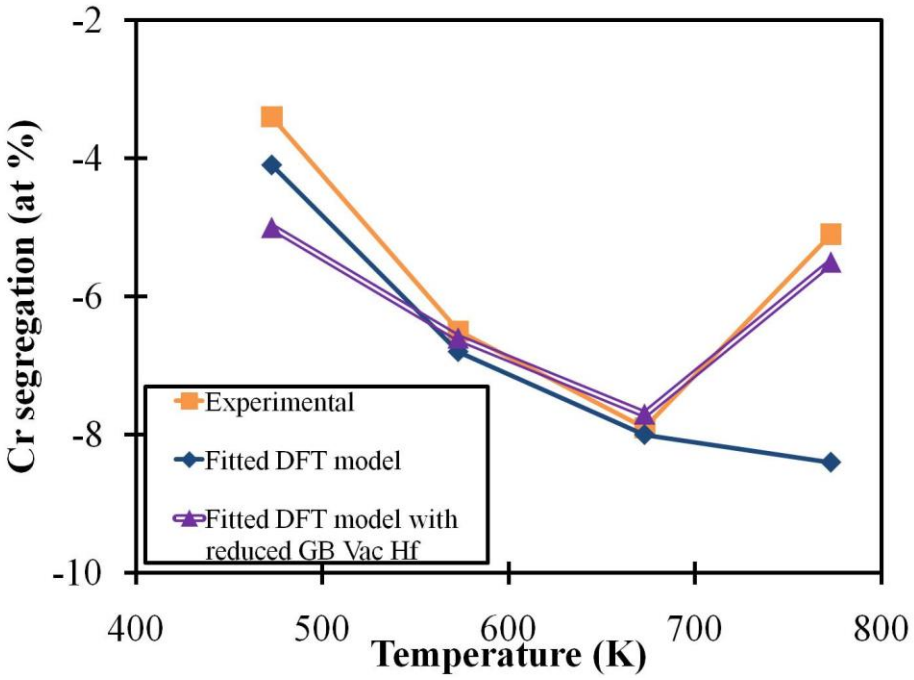

Figure 2.9: Cr segregation at 0.5 dpa from experimental measurement, from the best fit model, and the best fit model including the effect of reduced GB enthalpy of formation.

While the agreement with experiment at low temperatures is much better after fitting, the turnaround in RIS behavior at higher temperature is not captured by the basic model. The MIK model invokes a locally reduced vacancy formation enthalpy at the sink, which helps significantly in capturing this effect. Including this effect and using the sink vacancy formation enthalpy of 1.4 eV as recommended in [11] results in improved model agreement with experimental measurement. The DFT calculated values of the eight adjustable migration barriers and their values in the best fit model of Fig. 2.9 are summarized in Table 2.2.

Table 2.2: Values of the eight migration barriers used as adjustable parameters in the best fit model as calculated in [10] by DFT, values used in the best fit model of fig. 5, and the absolute difference between the two values.

Vacancy Barrier	DFT Value (eV)	Fitted Value (eV)	Absolute Difference (eV)	Interstitial Barrier	DFT Value (eV)	Fitted Value (eV)	Absolute Difference (eV)
w_1	0.980	0.943	0.037	w_R	0.750	0.735	0.015
w_2	0.828	0.821	0.007	w_I	0.310	0.345	0.035
w_3	1.018	0.988	0.030	w_3	0.260	0.285	0.025
w_4	1.054	1.061	0.007	w_2'	0.000	0.016	0.016

The largest difference between the DFT calculated values and the best fit values is 0.037 eV, while the error in the DFT values associated with convergence alone was estimated in [22] to be 0.035 eV. Thus, it is possible to bring the model predictions into agreement with experimental measurement by adjusting some of the input parameters by an amount commensurate with the expected error in the DFT parameters. This result serves to illustrate how sensitive the DFT-based RIS model is to the input parameters, however it does not necessarily demonstrate that DFT errors are the source of the discrepancy between the model predictions and experimental measurements. Other sources of error associated with physical mechanisms neglected in the basic formulation of the model will be explored in subsequent sections.

Fig. 2.10 depicts the ratios $d_{Cr}^{*Vac}/d_{Ni}^{*Vac}$ and $d_{Cr}^{*Int}/d_{Ni}^{*Int}$ as a function of temperature for both the best fitted model and as determined by DFT in [22].

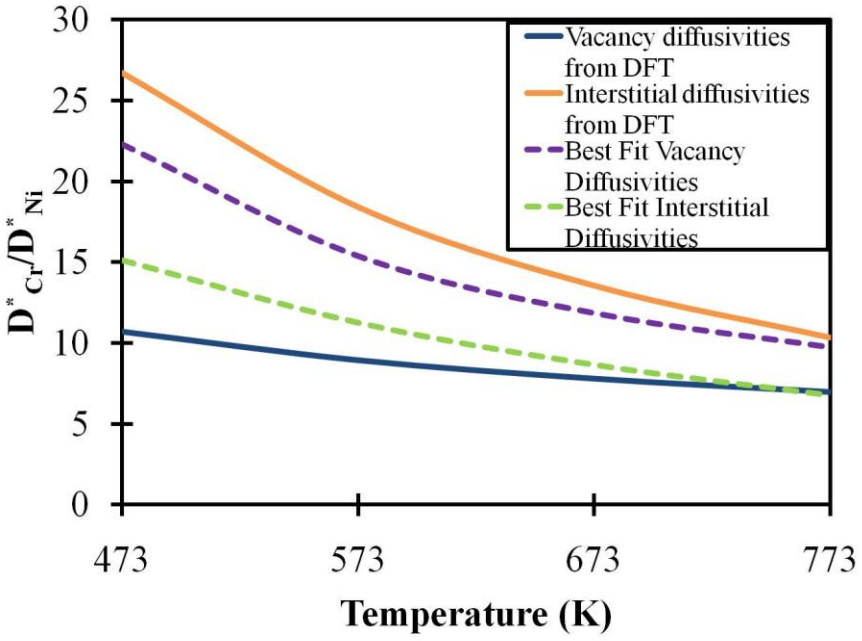

Figure 2.10: Cr and Ni tracer diffusivity ratios as calculated by DFT in [10] and as calculated using the best fit model parameters in table 1.

It is important to note that even after adjusting the model input parameters to reproduce experimental data, the tracer diffusivity ratios for vacancy and interstitials still reflect the primary conclusions reached in [22]; namely, that Cr diffuses much faster by both vacancies and interstitials, and the final RIS behavior is the result of the competition between these effects. Consequently, there is some evidence from this model that interstitials play a significant role in RIS. However contrary to the model of Nastar *et al* [23] the effect of interstitials in this model leads to Cr enrichment, rather than Ni enrichment. Furthermore, the DFT-based RIS model suggests that the disparity between the Cr and Ni vacancy diffusivities is much larger than has been proposed in all previous RIS models of which we are aware. Therefore, rather than corroborating one or more of the previously established Ni-Cr RIS models, the model developed here represents a significantly different physical description of the mechanisms underlying RIS.

In the next section, we will consider two additional physical phenomena absent from the basic DFT-based RIS model that may also contribute to the discrepancy between model predictions and experimental measurements: Cr-Cr interstitial trapping and biased defect sinks.

2.5.2 RIS model predictions with Cr-Cr interstitial trapping and biased defect sinks

Independent of the ratios $d_{Cr}^{*Vac}/d_{Ni}^{*Vac}$ and $d_{Cr}^{*Int}/d_{Ni}^{*Int}$, the RIS model predictions can be altered by reducing the flux of one type of defect with respect to the other. In this section we will consider two phenomena that may reduce the interstitial flux, thereby inhibiting the effect of interstitials on RIS and strengthening the effect of vacancies. The first phenomenon is Cr-Cr interstitial trapping. Interstitials are known to bind strongly to Cr solutes in Ni-based fcc alloys [23, 28]. The strong binding between a single Cr and an interstitial (in a local environment of pure Ni) is already accounted for in the calculation of the diffusivities [22] and the formulation of the system free energy (Sec. 2.2). However, Cr-Cr interactions are not included in the dilute model of Ref. [22] and have been shown to be significant [23], and it was suggested by Tucker *et al* [22] that the loss of mobile interstitials as they become trapped as strongly bound Cr-Cr interstitial dumbbells could have a significant impact on RIS. The second phenomenon we will consider is the effect of biased microstructural defect sinks, such as dislocations, which preferentially capture interstitials [9, 40]. We will note here that a third phenomenon which may alter the balance of vacancies and interstitials is defect production bias [9]. During irradiation damage cascades both interstitials and vacancies can form immobile defect clusters, and there is evidence from experiment [41] and simulations [42] that more interstitials are lost to these clusters than vacancies, resulting in an unbalanced effective production rate of mobile defects. The possibility of such a production bias playing a role in RIS has been mentioned in both Refs.

[22] and [24]. However, production bias is a phenomenon that occurs only when defects are produced in cascades, and does not occur when defects are produced as single Frenkel pairs, such as under electron irradiation. If production bias has a substantial effect on RIS, one would therefore expect RIS behavior to depend strongly on irradiation type. Such a dependence is not observed experimentally, as similar alloys irradiated with electrons [43] and protons [11] exhibit very similar segregation. These results suggest that production bias does not play a significant role in RIS and we will therefore not consider it further here.

In reality, some fraction of the excess vacancies that result from the loss of interstitials to biased sinks cluster together to form voids rather than diffusing to a grain boundary. For example, the interstitial dislocation bias is often linked to radiation-induced swelling in fcc metals [9, 40] associated with void formation. However, in our models we will assume that all excess vacancies diffuse to the sink plane, thereby providing an approximation for the maximum impact of the effects being considered on RIS. In the model any process that suppresses the interstitials and leaves excess vacancies results in a flux of excess vacancies to the sink plane with respect to interstitials, and there is a corresponding small net loss of mass in the sink plane:

$$\frac{dC_{Cr}^{1}}{dt}+\frac{dC_{Ni}^{1}}{dt}<0=K_{loss} \tag{2.13}$$

In a physical system, we hypothesize that these excess vacancies would diffuse along the grain boundary and ultimately coalesce into grain boundary voids or be annihilated at surface sinks. Mass balance in the first lattice plane is then restored by the flux of atoms corresponding to this diffusion of vacancies along the grain boundary to other sinks. To simulate this atom flux, we add the following terms to the concentration evolution of atomic species in the first lattice plane:

$$\frac{dC_{Cr}^{1}}{dt} \rightarrow \frac{dC_{Cr}^{1}}{dt} + K_{Cr}$$
$$\frac{dC_{Ni}^{1}}{dt} \rightarrow \frac{dC_{Ni}^{1}}{dt} + K_{Ni} \quad (2.14)$$

where the restoration rates K_{Cr} and K_{Ni} are defined such that they balance the total loss rate K_{loss}:

$$K_{Cr} + K_{Ni} = -K_{loss} \quad (2.15)$$

If the restoration of mass occurs via grain boundary diffusion, then it is reasonable to suppose that these rates are proportional to the nearby grain boundary concentrations of Cr and Ni. This constraint combined with the fact that $C^{1}_{Cr} + C^{1}_{Ni} \approx 1$ and Eqn. 2.13 yields

$$K_{Cr} = -C_{Cr}^{1} K_{loss}$$
$$K_{Ni} = -C_{Ni}^{1} K_{loss} \quad (2.16)$$

We now consider the necessary alterations to the basic DFT-based RIS model to implement the effect of Cr-Cr interstitial trapping. This approach follows that given in Ref.[44]. The traps in the RIS model are selected to be pairs of Cr atoms sitting on a lattice as nearest-neighbors. In dilute Ni-Cr alloys Cr-Cr dumbbells are extremely stable and may therefore serve as a temporary trap for interstitials. If the alloy is dilute, a Cr-Cr dumbbell will very likely have to dissociate the two Cr to form a Ni-Cr dumbbell to hop. The energy landscape of dissociation is such that minimum energy to completely dissociate a Cr-Cr dumbbell is the binding enthalpy, 0.92 eV [23].This trapping mechanism is implemented by introducing two new defect species into our rate model: trapped Cr-Cr interstitials and unoccupied Cr interstitial traps, defined as any Cr with at least one Cr in a nearest neighbor position. The equations that describe the time evolution of these new species are

$$\frac{dC_{Int}^{T}}{dt} = K_{Int}^{T} C^{T} C_{Int} - \tau_{Int} C_{Int}^{T} - R_{Int}^{T} C_{Int}^{T} C_{Vac}$$
$$\frac{dC^{T}}{dt} = -K_{Int}^{T} C^{T} C_{Int} + \tau_{Int} C_{Int}^{T} + R_{Int}^{T} C_{Int}^{T} C_{Vac} \quad (2.17)$$

where C_{Int}^{T} is the concentration of trapped interstitials and C^{T} is the concentration of unoccupied traps. R_{Int}^{T} and K_{Int}^{T} are the recombination and trapping coefficients, respectively given by

$$R_{Int}^{T} = \frac{4\pi r_{VT}}{\Omega} D_{Vac}$$
$$K_{Int}^{T} = \frac{4\pi r_{IT}}{\Omega} D_{Int} \quad (2.18)$$

where r_{VT} is the recombination radius for a vacancy and a trapped interstitial, given by the normal vacancy-interstitial recombination radius, and r_{IT} is the trapping radius, equal to the 3rd nearest neighbor distance. The dissociation coefficient τ_{Int} determines how strongly interstitials are bound to traps, and is given by

$$\tau_{Int} = \frac{d_{Int}}{a^{2}} \exp\left[\frac{-E_{bind}}{k_{b}T}\right] \quad (2.19)$$

where E_{bind} is the binding enthalpy of the trap. Note that only one of the two equations in Eqn. 2.17 needs to be solved, as the two new trapping species are trivially related by

$$C^{T} = C_{0}^{T} - C_{Int}^{T} \quad (2.20)$$

Here C_{0}^{T} is the initial concentration of unoccupied traps, approximated by the number of Cr-Cr nearest neighbor pairs assuming a random distribution on an fcc lattice. A probability calculation yields the expression

$$C_{0}^{T} = C_{Cr}(1 - C_{Ni}^{\varepsilon}) \quad (2.21)$$

C_{Cr} and C_{Ni} are the nominal alloy concentrations of Cr and Ni, and the power z = 12 is the number of nearest-neighbors in the fcc lattice.

The introduction of the trapping species requires the following alterations to the continuity equations for vacancies and (unbound) interstitials:

$$\begin{aligned} \frac{dC_{Vac}}{dt} &= G - R_{IV}C_{Int}C_{Vac} - R_{Int}^{T}C_{Int}^{T}C_{Vac} - \frac{dJ_{Vac}}{dx} \\ \frac{dC_{Int}}{dt} &= G - R_{IV}C_{Int}C_{Vac} - K_{Int}^{T}C^{T}C_{Int} + \tau_{Int}C_{Int}^{T} - \frac{dJ_{Int}}{dx} \end{aligned} \tag{2.22}$$

The new terms are the recombination rate of vacancies with trapped interstitials $R_{Int}^{T}C_{Int}^{T}C_{Vac}$, the loss rate of free interstitials to traps $K_{Int}^{T}C^{T}C_{Int}$, and the release rate of trapped interstitials $\tau_{Int}C_{Int}^{T}$.

In Fig. 2.11, the bulk concentration evolution of freely migrating interstitials is plotted both with and without the effects of interstitial binding.

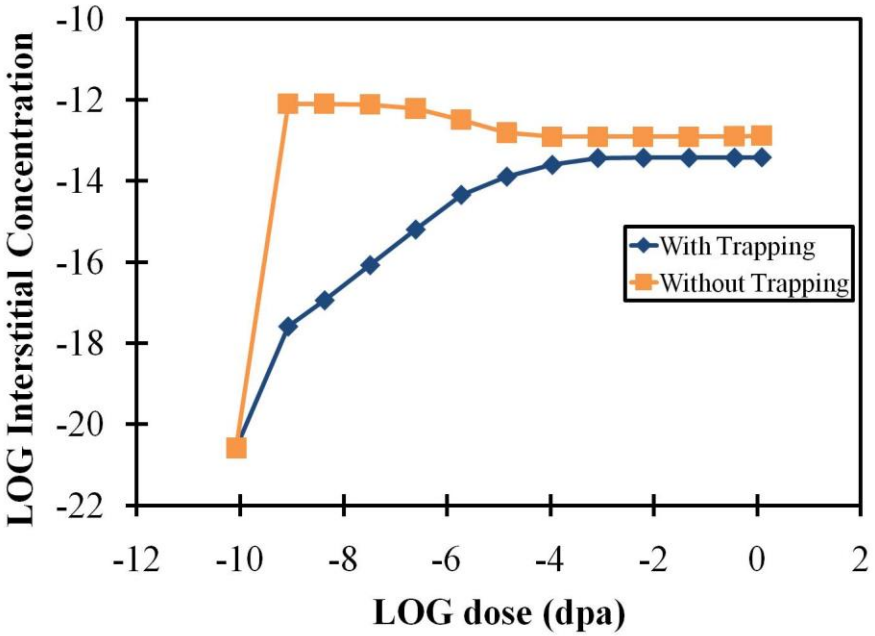

Figure 2.11: Model predicted bulk interstitial concentration at 673 K with and without trapping as a function of dose.

Evidently the primary effect of Cr interstitial trapping is to temporarily suppress the buildup of mobile radiation-induced interstitials in the bulk. Eventually, however, the rate of interstitial loss to trapping becomes equal to the rate at which trapped interstitials manage to escape, at which time build up of interstitials proceeds rapidly. The final steady state interstitial concentration is only slightly reduced with respect to the system with no interstitial trapping.

To implement the effect of biased defect sinks, the following alterations to concentration evolution equations for interstitials and vacancies (Eqns 2.1) are necessary:

$$\frac{dC_{Vac}}{dt} = G - R_{IV}C_{Int}C_{Vac} - R_{VD}C_{Vac} - \frac{dJ_{Vac}}{dx}$$
$$\frac{dC_{Int}}{dt} = G - R_{IV}C_{Int}C_{Vac} - R_{ID}C_{Int} - \frac{dJ_{Int}}{dx} \qquad (2.23)$$

The new terms associated with loss to dislocations are $R_{VD}C_{Vac}$ and $R_{ID}C_{Int}$, which describe the rate of vacancy and interstitial loss to dislocations, respectively. The rate coefficient R_{jD} is determined by the following equation [9]:

$$R_{jD} = Z_{jD} 4\pi r_{iD} \frac{\rho_D}{\delta} d_j \tag{2.24}$$

where r_{jD} is the radius of capture for defect species j, r_D is the dislocation density, δ is the interplanar distance, and d_j is the diffusivity of defect species j. The biased defect loss is captured by the bias factor Z_{jD}, where $Z_{jD} > 1$ results in biased loss of defect species j.

RIS was simulated in the Ni-18Cr model alloy using a constant dislocation density of 10^{12} m/m^3, a reasonable value for an annealed fcc metal [35]. The self-interstitial dislocation bias in Ni has been estimated by Wolfer to be as high as approximately 1.3 [40]. While this value is higher than more generally accepted values in the range of 1.1-1.2 [9], we will utilize it in this analysis to provide an upper bound for the effect of sink bias.

Fig. 2.12 depicts the DFT-based model predicted Cr segregation at 0.5 dpa as a function of temperature for four different scenarios: first, using only the basic model, second, including the effects of interstitial trapping, third, including biased sinks, and finally, including both trapping and biased sinks.

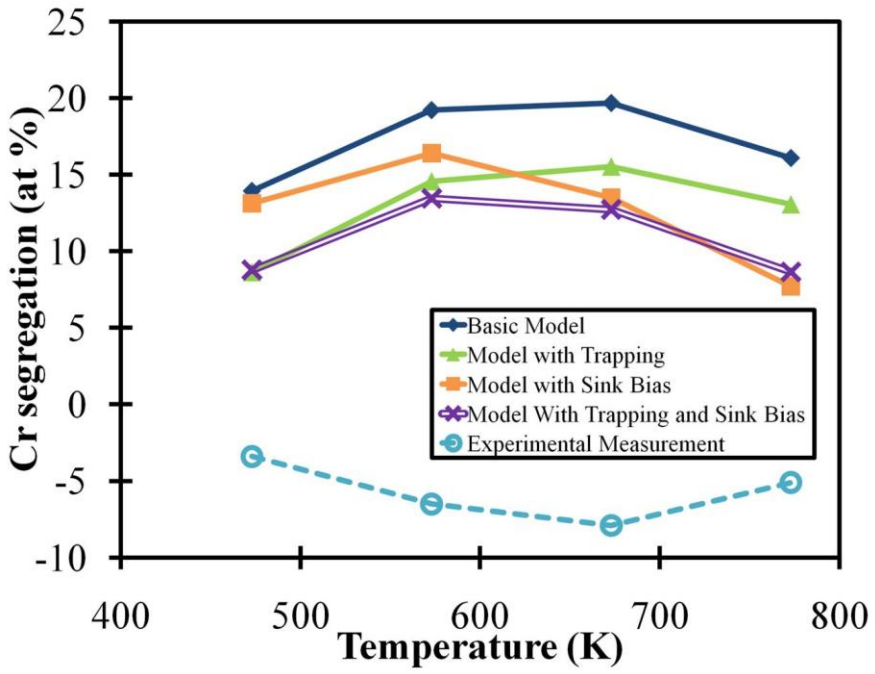

Figure 2.12: Cr segregation at 0.5 dpa as a function of temperature for 4 scenarios: The basic model, the model with trapping, the model with biased sinks, and the model with both trapping and biased sinks.

While both trapping and biased sinks result in reduced Cr enrichment relative to the basic model, their effects, even when combined, are insufficient to bring the model prediction into agreement with experiment.

In contrast with the result in the Fe-Cr system, the basic DFT-based RIS model has failed to capture the basic RIS tendencies in the Ni-Cr system. This discrepancy is due to the fast Cr interstitial diffusion effect predicted by the DFT-based diffusion theory of Tucker et al. [22], which results in significant Cr enrichment in the RIS model. Two effects which may reduce this effect, Cr-Cr trapping and biased defect sinks, were found to be insufficient to account for this discrepancy. A third possible source of the discrepancy is the lack of concentration dependence in the tracer diffusivities used in the RIS model. The basic formulation of the RIS model uses vacancy and interstitial diffusivities determined via DFT in the limit of Cr in dilution in Ni.

Experimental measurements indicate that the ratio $d_{Cr}^{*Vac} / d_{Ni}^{*Vac}$ is approximately constant with respect to composition in the range of 0-30 at% Cr [45], therefore using the dilute limit values for the vacancy diffusivities is a reasonable approximation and introducing concentration dependence into these diffusivities would not significantly alter the RIS model predictions. However, there is presently no available information regarding interstitial diffusivities in the concentrated Ni-Cr alloys. Furthermore, DFT calculations have indicated that Cr atoms interact strongly with self-interstitial defects in Ni-Cr alloys [28], in contrast with the Fe-Cr system where a relatively weak interaction is observed [46]. Therefore, the missing concentration dependence in the interstitial tracer diffusivities d_{Cr}^{*Int} and d_{Ni}^{*Int} is a likely source of the discrepancy between the basic DFT-based RIS model predictions and experimental measurements of RIS in Ni-Cr alloys. The use of first principles-based molecular dynamics simulations to determine interstitial diffusivities in the concentrated Ni-Cr system and their impact on RIS predictions is the subject of the next section.

2.6 Ab initio molecular dynamics simulation of interstitial diffusion in Ni-Cr alloys and implications for radiation induced segregation

Under most conditions, diffusion in metals is dominated by the concentration and mobility of vacancy defects. While interstitial defects are typically far more mobile than vacancies, their high formation energy results in very small thermal equilibrium concentrations under most conditions and their contribution to atomic mobility is often negligible. An important exception is presented by metals exposed to radiation, in which both vacancies and interstitials are produced in approximately equal proportions and far in excess of their thermal equilibrium concentrations. Under such circumstances interstitial diffusion is not negligible and

has significant consequences for diffusion-related microstructural processes. Consequently, a detailed understanding of interstitial diffusion is fundamental for the prediction of long-term microstructural evolution of metals under irradiation.

One microstructural effect of radiation in which the role of interstitials is not yet fully understood is RIS. As discussed in Sec 2.1, models for understanding and predicting RIS of Ni and Cr have for the most part neglected the effect of interstitial diffusion, due to a lack of information regarding the species-dependent interstitial diffusivities, particularly as a function of concentration [18, 20, 21, 47, 48]. Some attempts have been made to incorporate the impact of the interstitial flux on RIS of Cr and Ni in Ni-Cr-Fe alloys by assuming that Ni interacts preferentially with interstitial dumbbells, with limited success [23, 37, 49, 50]. Because of the dearth of experimental information regarding interstitial dumbbell diffusion, such models rely heavily on fitting to segregation data and assumptions that are difficult to validate. For instance, it is most often assumed that Cr will interact repulsively with the interstitial dumbbells because it is oversized with respect to Ni. Under such an assumption, the interstitial flux will have a tendency to cause some enrichment of Ni and depletion of Cr near grain boundaries. Recent density functional theory (DFT)-based modeling of interstitial diffusion coefficients in dilute Ni-Cr alloys by Tucker et al. [22] has demonstrated that the opposite is true; Cr in fact exhibits a very strong binding interaction with interstitial dumbbells. The results of this model have indicated that interstitial diffusion exhibits strong species dependence in Ni-Cr alloys, and that the interstitial flux should lead to Cr enrichment at grain boundaries. The model of Tucker et al. is however strictly limited to the dilute alloy regime, and using it to predict RIS in concentrated Ni-Cr alloys produces erroneous results [51]. An accurate description of RIS in Ni-Cr alloys

therefore requires detailed, quantitative knowledge of Ni and Cr interstitial diffusion in the concentrated alloy regime. The goal of the research presented in this section was to utilize molecular dynamics simulations of interstitial diffusion in the fcc Ni-Cr crystal to determine interstitial mediated diffusivities for Ni and Cr in the Ni-18 Cr model alloy, and to assess the impact of interstitial diffusion on RIS in this material.

Because interstitial dumbbell defects have a very low migration barrier in most metals (on the order of 100 meV in pure Ni), interstitial diffusion occurs on a time scale that is easily accessible to molecular dynamics simulations. Composition-dependent interstitial diffusion coefficients may therefore be determined directly from such simulations. This approach has been used extensively to study interstitial diffusion in Fe-Cr alloys and bcc metals [52-58]. However, such simulations often rely upon empirical potentials to describe atomic interactions. As there is almost no experimental interstitial diffusion data available to aide in benchmarking or fitting, the accuracy of such empirical methods is difficult to assess. As an alternative to empirical potentials, density functional theory (DFT) can be used to determine atomic interactions *ab initio*. This approach is significantly more computationally intensive than conventional empirical potential molecular dynamics, and is consequently limited to much smaller simulated systems and shorter simulation times. Despite these limitations, it has been used successfully to study interstitial He diffusion in alpha Fe [59] and Si self-interstitial diffusion [60], as well as ionic conductivity in superionic α-CuI [61].

In the research presented in this section, we utilize ab initio molecular dynamics (AIMD) simulations to investigate interstitial diffusion in Ni-Cr alloys. Our results provide quantitative, first principles-based information regarding the species-dependent dumbbell interstitial diffusion

in a concentrated Ni-Cr alloy for the first time. Furthermore, our results indicate that interstitials do play an important role in RIS in Ni-Cr alloys, specifically in moderating the strong tendency for Cr to be depleted by vacancy diffusion. Finally, these results show that diffusion of metal interstitial dumbbells can be studied by direct AIMD.

2.6.1 Molecular Dynamics Simulations of Interstitial Diffusion

Interstitial diffusion was simulated in this study by ab initio molecular dynamics, wherein the atomic interactions are determined via density functional theory (DFT). All simulations were performed using the Vienna Ab Initio Simulations Package (VASP) [62-65] in the generalized gradient approximation using the Perdew-Burke-Ernzerhof [66] exchange-correlation functional, and using the projector-augmented wave method [67]. A 2×2×2 k-point mesh and an energy cutoff of 350 eV were used, and all calculations were spin polarized. Simulation cells consisted of a 2×2×2 cubic supercell of the fcc conventation cell, with a single [100] interstitial dumbbell placed randomly on one of the lattice sites. All other lattice sites were occupied by a single Ni or Cr atom, for a total of 33 atoms in the system. Simulations were performed in the NVT ensemble using a Nosé-Hoover [68] thermostat, with a Nosé mass parameter of 1.5 a.m.u. which corresponds to a Nosé frequency of approximately 3×10^{13} Hz. This frequency is on the same order of magnitude as the phonon spectrum in pure Ni [69]. The cell size was given by the pure Ni lattice parameter of 3.53 Å. Pure Ni interstitial diffusion coefficients were collected from a schedule of simulations spanning temperatures from 800 to 1400 K. Ni and Cr interstitial diffusion coefficients were also determined in a Ni-18Cr alloy, for temperatures from 1200 to 1800 K. This composition was chosen to match the model alloy studied in the RIS measurements of Allen et al. [11], in which the basic RIS model predictions showed significant

discrepancies with experimental measurements (see Sec. 2.5.1). A higher temperature range was used for the Ni-18Cr alloy than for the pure Ni alloy due to Cr-interstitial binding effects, which reduce interstitial mobility and are challenging to resolve at lower temperatures. At each temperature and composition, 5 simulations were performed of 20 ps in length, with a time step of 1.5 fs and an initial equilibration period of 5 ps. Position data for each atom was collected after each time step, and this position data was subsequently used to determine the interstitial diffusion coefficients for Ni and Cr atoms in the simulation.

In order to estimate possible errors due to convergence, a number of static calculations were performed using identical settings to those used in our AIMD simulations for system size, k-point density, and cutoff energy (32-33 atoms, 2×2×2 k-point mesh, 350 eV cutoff), and these calculations were then compared to well-converged literature values for Cr-interstitial interaction energies and interstitial migration energies. Where no comparison value could be found, a value was calculated using the methodology of Tucker et al. [22] (108 lattice sites, 3×3×3 k-point mesh, 279 eV cutoff). The results of these calculations are presented in Table 2.3.

Table 2.3: Comparison of binding and migration energies calculated with the DFT parameters used in the AIMD simulations of this study to the better- converged calculations of Tucker et al. [22, 28].

Cr-Interstitial arrangements	Binding Energy (eV)	Comparison Value [28] (eV)
NiNi-Cr	-0.20	-0.18
NiCr-Ni	-0.50	-0.50
NiCr-Cr	-0.72	-0.76
CrCr-Ni	-0.88	-0.92
[110] to [010] migration in Ni	Migration Energy (eV)	Comparison Value (eV)
NiNi-Ni to NiNi-Ni	0.14	0.14 [22]
NiCr-Ni to NiCr-Ni	0.06	0.08 [22]
NiNi-Ni to NiNi-Cr	0.10	0.15 [28]
CrNi-Ni to NiNi-Cr	0.30	0.32 [28]
CrCr-Ni to NiCr-Cr	0.14	0.14 [28]
CrCr-Cr to CrCr-Cr	0.08	0.13
CrNi-Cr to CrNi-Cr	0.12	0.14

The notation *AB-C* specifies an interstitial dumbbell composed of atoms of type *A* and *B*, with a nearest neighbor atom type *C* on a site that is eligible for dumbbell migration forming a *CB-A* dumbbell without an onsite rotation. Binding energies are defined relative to a Ni-Ni dumbbell in pure Ni and single, solute Cr atoms in Ni. The errors in binding energies relative to the comparison values are 40 meV or below. The migration barriers calculated using 32 lattice site cells are on average 23 meV lower than the comparison values, with a standard deviation in the errors of 21 meV. While this is not an insignificant convergence error, it is small relative to the interstitial binding energies and the measured effective activation energy for the interstitial diffusivities. At 1000 K a 23 meV average reduction in migration energies would correspond to a change of just 23% in the measured diffusion coefficients, if it appeared directly in the total effective migration energy (see Sec. 2.6.4). We therefore argue that the migration barriers are sufficiently captured to simulate realistic interstitial diffusion, although robust quantitative

convergence is not achieved to the normal standards of DFT studies of defect migration energetics, due to the high computational cost of AIMD relative to static calculations.

Two of the most significant approximations utilized in the simulation methodology of this study are the use of a constant lattice parameter for all simulations and the assumption that a 32 atom unit cell is sufficiently large to meaningfully capture measured interstitial diffusion. In order to assess the validity of the use of a fixed lattice parameter, a large set of AIMD simulations of interstitial diffusion were performed in pure Ni at 1000 K over a range of lattice parameter values between 3.49 and 3.64 Å. From experimental measurements, the lattice parameter might be expected to increase to 3.59 Å at 1000 K in pure Ni [70] and 3.62 Å in the Ni-18Cr alloy [71], which lie within the ranged tested here. Fig. 2.13a depicts the resulting measured interstitial diffusivity normalized by lattice parameter squared as a function of lattice parameter used in the simulation, where interstitial diffusivity has been determined according to the method detailed in Sec. 2.6.2.

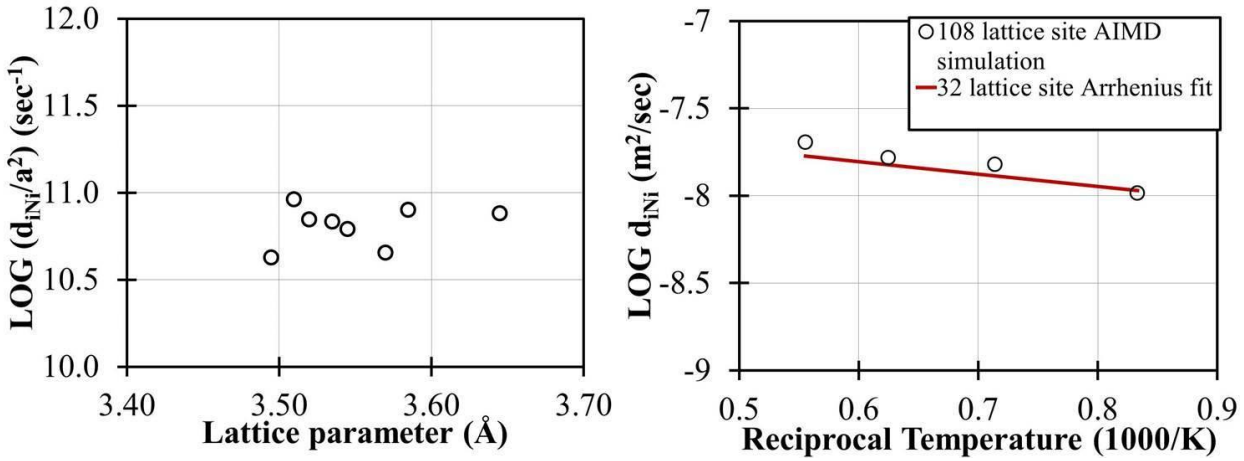

Figure 2.13a (left): Interstitial tracer diffusivity of pure Ni at 1000 K measured from AIMD simulations using a range of lattice parameter values. Diffusivity measured in each simulation has been normalized by the lattice parameter squared. b (right): Interstitial tracer diffusivity in pure Ni as measured from AIMD simulations in 108 lattice site cells and the Arrhenius fit to the results of the 32 lattice site simulations

Normalizing the diffusivity in this way removes the geometric dependence of the diffusivity coefficient on the lattice parameter, and should isolate only the dependence of the migration barrier and attempt frequency on the simulated system size. The normalized diffusion coefficients are nearly flat over a wide range of lattice parameter values, increasing only slightly between 3.49 Å and 3.64 Å. This result indicates that the measured diffusion coefficient is only weakly affected by the choice of system volume. We therefore conclude that the choice of lattice parameter, within a reasonable range of the pure Ni value, appears to have little impact on the measured diffusivity coefficient.

A large number of static calculations were performed to assess possible convergence errors with respect to supercell size, as described above. In addition, a small set of AIMD simulations of interstitial diffusion in pure Ni were performed using a 3×3×3 fcc supercell containing 108 lattice sites. In Fig. 2.13b, the pure Ni diffusivities measured from these simulations are compared to the Arrhenius fit obtained from the larger set of simulations using 32 lattice sites (details of these results may be found in Sec. 2.6.3). The measured diffusivities are very close to the Arrhenius fit. Combined with the results of the static calculations, these results suggest that the simulations using the 32 site system size should be well enough converged to draw meaningful conclusions.

2.6.2 Determination of interstitial diffusion coefficients

During the course of a simulation, the Ni and Cr atoms migrate away from their initial lattice positions due to the sequential hops of the dumbbell interstitial defect. A measurement of this displacement as a function of time is used to determine the diffusion coefficients of Ni and Cr according to a finite time approximation of the Einstein relation [72]:

$$D_s = \frac{\left\langle r_s^2(t) \right\rangle}{2dt} \tag{2.25}$$

Here D_s is the diffusion coefficient of species *s*, *d* is the dimensionality of the motion, and *t* is time. The quantity $\left\langle r_s^2(t) \right\rangle$ is the average of the square displacement of species *s*, computed as follows:

$$\left\langle r_s^2(t) \right\rangle = \frac{1}{N_s N_t} \sum_{j=1}^{Nt} \sum_{i=1}^{Ns} \left[r_i(o_j + t) - r_i(o_j) \right]^2 \tag{2.26}$$

The outer summation is over N_t time origins and the inner summation is over N_s atoms of species *s*. The quantity $r_i(o_j + t) - r_i(o_j)$ is the net displacement of atom *i* over the time span between time origin o_j and $o_j + t$. A simulation consisting of *N* time steps will have a total of *N* possible time origins over which to perform the above summation. However, when taking every time step as a possible time origin, evaluations of $\left\langle r_s^2(t) \right\rangle$ at times near the maximum simulation time will have only a few time origins contributing to them, resulting in poor statistical averaging. To ensure that an equal number of time origins are used in the evaluation of $\left\langle r_s^2(t) \right\rangle$ at all times *t*, we take the number of time origins N_t to be half the total number of time steps, $N/2$, and we evaluate $\left\langle r_s^2(t) \right\rangle$ for all times between 0 and $\delta t\, N/2$, where δt is the time step [73]. Once the values of $\left\langle r_s^2(t) \right\rangle$ have been gathered for Ni and Cr from a given simulation, the diffusion coefficients D_s may be obtained from a linear fit to a plot of $\left\langle r_s^2(t) \right\rangle$ vs *t*. Only times after 3 ps were used in the fitting to avoid the transient non-diffusive motion which occurs at the start of the simulation [73]. The resulting diffusion coefficient is dependent upon the artificial interstitial

site fraction C_{Int} of 1/32 used in the simulations; to remove this dependence we recast the diffusion coefficient as diffusivity d_s using the following relationship:

$$d_s = \frac{D_s}{C_{Int}} \tag{2.27}$$

Eqns. 2.25 and 2.26 yield the tracer diffusion coefficient, which is distinct from the jump diffusion coefficient. The latter is computed from the mean squared displacement of the center of mass of the diffusing particles, rather than from the displacement of the individual particles themselves. The values of these two diffusion coefficients are similar but are not in general equivalent [74]. In this case, it has been found that the tracer diffusion coefficients are 30-40% smaller than the corresponding jump diffusion coefficients. The tracer diffusion coefficient was the focus of this study as it is the tracer diffusion coefficients specifically that are used in the random alloy approximations of Manning [32] and Bocquet [33, 75] to compute phenomenological coefficients *Lij*, (Eqns 2.10), as discussed in Sec. 2.2.

The full matrix of coefficients *Lij* can in principle be measured from the simulation results using the following expression [27, 76]:

$$L_{ij} = \frac{\left\langle \sum_\alpha r_i^\alpha(t) \sum_\beta r_j^\beta(t) \right\rangle}{2dtN_s\Omega k_B T} \tag{2.28}$$

where $r_i^\alpha(t)$ is the vector describing the position of atom α of species *i* at time *t* relative to its initial position and Ω is the atomic volume. In practice, the off-diagonal term ($i \neq j$) appears to be particularly is slow to converge and would require significantly longer simulations than we can practically use to adequately capture with acceptable statistical precision. Fig. 2.14 depicts the values of the reduced phenomenological coefficient $\tilde{L}_{NiCr}$ (where $\tilde{L}_{NiCr} = \Omega k_B T L_{NiCr}$)

measured directly from the AIMD simulations in the Ni-18Cr alloy between 1200 and 1800 K, as well as values computed using the random alloy theory of Bocquet.

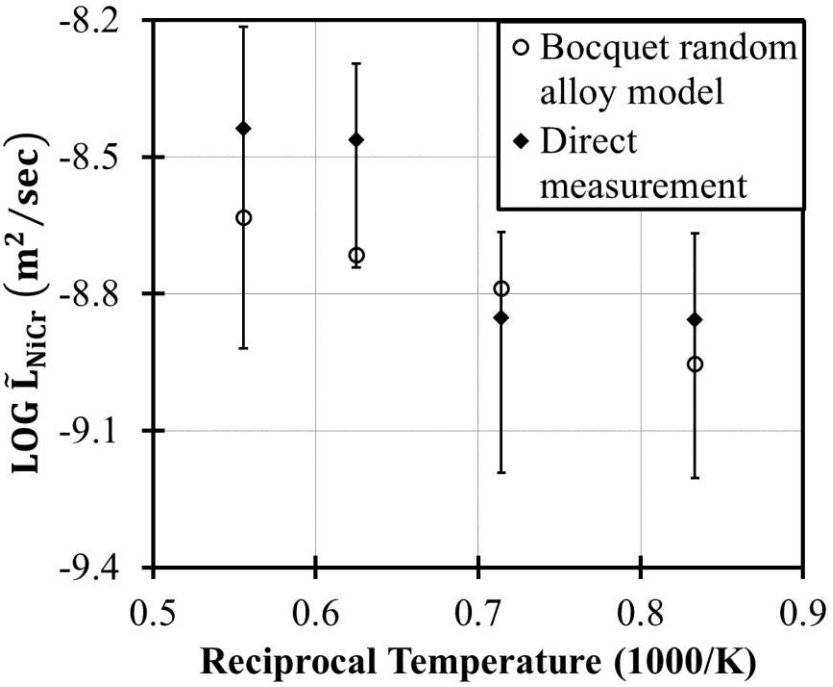

Figure 2.14: Off-diagonal reduced phenomenological coefficient $\tilde{L}_{NiCr}$ as measured from AIMD simulation and as computed using the random alloy theory of Bocquet [33, 75], based upon the measured Ni and Cr tracer diffusivities. The error bars represent the standard error in the mean of 5 measurements at each temperature

The generally acceptable agreement shows that both approaches can be used to estimate $\tilde{L}_{NiCr}$. However, the error bars on the AIMD determined values are quite large, and therefore it is difficult to use this approach to yield a robust value. We will therefore assume that the values of these off-diagonal terms are reasonably well captured by the random alloy theory of Bocquet, and with better statistical precision than is feasible via direct simulation.

To assess the role of concentration dependent interstitial diffusion in RIS, the rate theory model approach formulated in Sec. 2.2 was used to simulate RIS in a Ni-18Cr model alloy. The basic formulation of the model used the dilute alloy values of d_{Cr}^{*Int} and d_{Ni}^{*Int} determined by

Tucker et al. [22], whereas in this section the concentrated alloy values determined from AIMD simulation are used.

2.6.3 Comparison of diffusion theory and simulation results in pure Ni

While no experimental values of Ni and Cr interstitial diffusion coefficients are available, the AIMD simulation results can be benchmarked by comparing to the values determined for pure Ni from diffusion theory. For pure Ni, the interstitial tracer diffusivity can be calculated using the following expression [22].

$$d_{Ni} = \frac{2}{3} a^2 f_0 \nu_{m,Ni} \exp\left[\frac{-\Delta H_{m,Ni}}{k_B T}\right] \tag{2.29}$$

where a is the Ni lattice parameter, f_0 is the correlation factor for interstitial self-diffusion, $\nu_{m,Ni}$ is atomic migration attempt frequency, and $\Delta H_{m,Ni}$ is the enthalpy of atomic migration by interstitial dumbbell. Rigorously, the correlation factor f_0 is a temperature-dependent term that is determined by the relative frequencies of the [100] dumbbell migrating hop and rotating hop. In the limit where the rotating hop has a much higher frequency than the migrating hop the correlation factor approaches 1, while in the opposite limit where the rotating hop has a much lower frequency than the migrating hop the correlation factor approaches the lower bound value of 5/11 [22]. First principles calculations reveal that the latter limit is observed in pure Ni at all temperatures below melting [22]; we will therefore take f_0 to be a constant equal to 5/11 in Eqn. 2.29. The dumbbell migration enthalpy has been measured experimentally via resistivity recovery [77] and determined from first principles using DFT [22], with both approaches yielding a value of 0.14 eV. The migration attempt frequency is generally taken to be

approximately equal to the atomic vibrational frequency, and estimates vary between 1×10^{12} and 5×10^{12} Hz [19-22, 48].

Fig. 2.15 depicts the interstitial diffusivity of pure Ni as determined analytically from Eqn. 2.29 and as measured from AIMD simulations.

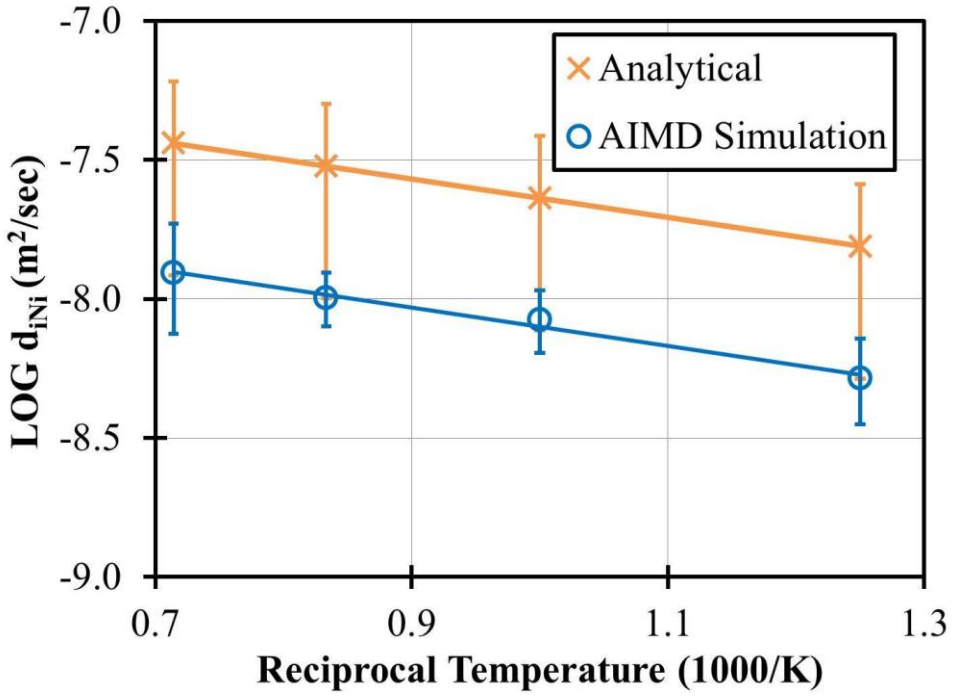

Figure 2.15: Interstitial tracer diffusivity in pure Ni as a function of reciprocal temperature, as determined analytically and as measured from AIMD simulations. Temperatures range from 800 K to 1400 K.

The error bars on the analytical values represent the spread in reported values for the attempt frequency, and the error bars on the simulation results are equal to the standard error in the mean calculated from 5 simulations at each temperature. Taking $f_0 = 5/11$, $a = 3.53$ Å, and fitting $\Delta H_{m,Ni}$ and $\nu_{m,Ni}$ to the AIMD data yields $\Delta H_{m,Ni} = 0.14\pm0.03$ eV and $\nu_{m,Ni} = 1.1^{+0.21}_{-0.17}\times10^{12}$ Hz. These uncertainties arise from the standard errors in the slope and the intercept of a linear fit of

$\log(d_{iNi})$ vs 1/T for all AIMD simulation results for pure Ni. This value of the activation energy is in excellent agreement with experiment and previous first principles calculations [22, 77, 78]. The migration attempt frequency is near the low end of typical estimates, though within the expected range of 1×10^{12} - 5×10^{12} Hz. The low value of the migration attempt frequency is consistent with the lower part of the analytical data range and the upper end of the simulation data range just overlapping.

2.6.4 Interstitial diffusivities in Ni-18Cr

In order to assess the species-dependent Ni and Cr interstitial diffusivities in the Ni-18Cr alloy, interstitial diffusion was simulated in a Ni-18Cr alloy at temperatures between 1200 K and 1800 K. Fig. 2.16 presents the ensemble averaged mean squared displacement for Ni and Cr in the simulated Ni-18Cr alloy as a function of time for four temperatures.

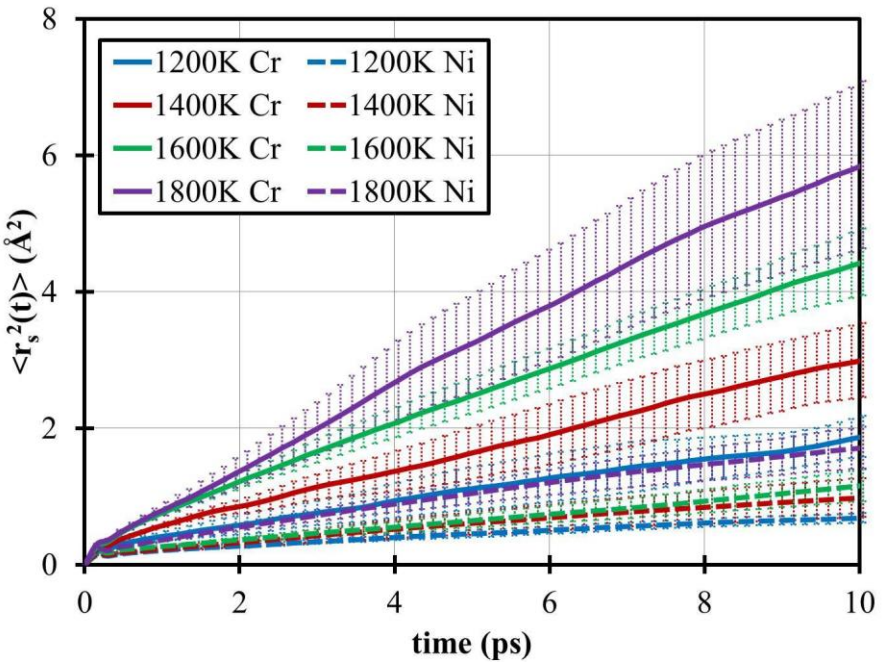

Figure 2.16: Mean squared displacement for Ni and Cr in the Ni-18Cr alloy for temperatures between 1200 and 1800 K, measured from AIMD simulations.

The error bars represent the standard error in the mean of 5 independent simulations. The regions beyond 3 ps for each curve were fit to linear regressions, with an R^2 value greater than 0.99 in all cases. The slopes of these lines are then used to determine diffusion coefficients according to Eqn. 2.25. The resulting Ni and Cr interstitial diffusivities are depicted as a function of the reciprocal temperature in Fig. 2.17.

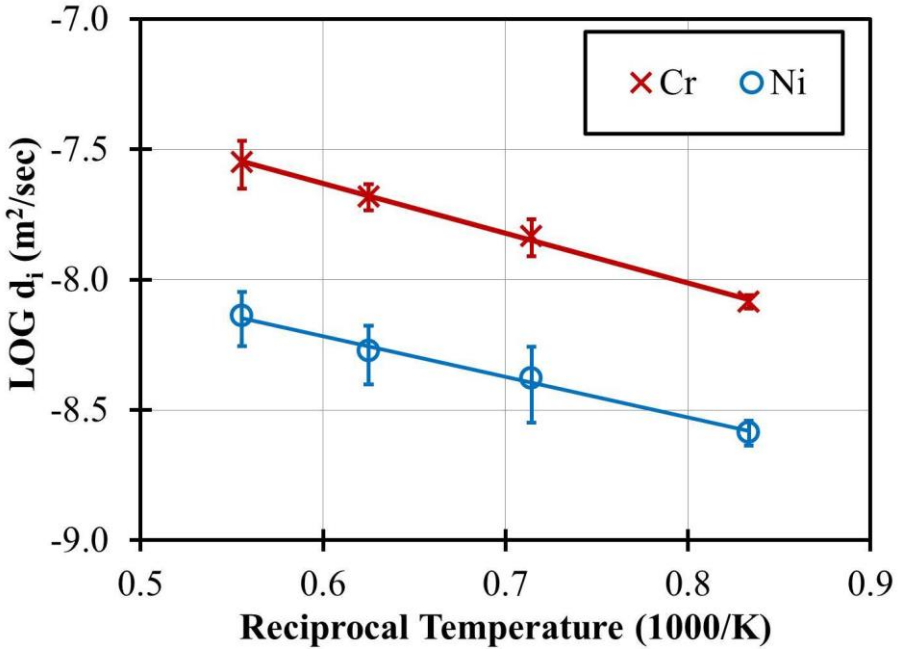

Figure 2.17: Interstitial tracer diffusivity of Ni and Cr in the Ni-18Cr alloy as a function of reciprocal temperature, as determined from mean squared displacements measured from AIMD simulations

The logarithms of both the Ni and Cr diffusivities show linear behavior vs reciprocal temperature and may be fit with an Arrhenius functional form. The preexponential factors and activation energies for the Arrhenius fits are provided in Table 2.4.

Table 2.4: Arrhenius fit parameters for Ni and Cr interstitial diffusivity in the Ni-18Cr alloy. The uncertainties arise from the standard errors in the slope and intercepts of Arrhenius fits to the d_{iCr} and d_{iNi} data collected from AIMD simulations.

Species	d_0 (m^2/sec)	E_a (eV)
Ni	$5.04^{+2.7}_{-1.7} \times 10^{-8}$	0.31 ± 0.05
Cr	$3.2^{+0.9}_{-0.7} \times 10^{-7}$	0.37 ± 0.03

The uncertainties on these Arrhenius parameters are incurred from the standard errors in the slope and intercepts of an Arrhenius fit to the d_{iCr} and d_{iNi} data collected from AIMD simulations.

The activation energies for both the Ni and Cr interstitial diffusivities in Table 2.4 are 2-4 times higher than the dilute alloy values for interstitial migration (0.14 and 0.08 eV, respectively). The simulation results therefore indicate that interstitial diffusion is much slower in the concentrated Ni-18Cr alloy than in the dilute regime, in qualitative agreement with the results of resistivity recovery measurements in concentrated Fe-Ni-Cr alloys [78]. From these measurements Dimitrov et al. estimated an effective activation energy of around 0.4 eV for interstitial dumbbell migration in Ni-16Cr, in reasonably good agreement with the activation energies in Table 2.4.

DFT calculations have revealed strong binding interactions between interstitial dumbbells and solute Cr atoms in Ni-Cr alloys [28], which may be the cause of the reduced interstitial diffusion in the Ni-18Cr alloy with respect to pure Ni. A CrCr dumbbell configuration exhibits a dramatic binding energy of -0.9 eV with respect to a NiNi dumbbell and isolated Cr atoms. Tucker [28] hypothesized that this CrCr dumbbell configuration would act as a trap for interstitial diffusion in dilute Ni-Cr alloys, according to the following argument: if the environment around the CrCr dumbbell is pure Ni, then the dumbbell defect must undergo the

following sequence of changes in configuration in order to execute long range diffusion, with a total increase in binding energy of 0.9 eV:

$$CrCr-Ni \overset{+0.14eV}{\rightarrow} NiCr-Cr \overset{+0.26eV}{\rightarrow} NiCr-Ni \overset{+0.3eV}{\rightarrow} NiNi-Cr \overset{+0.2eV}{\rightarrow} NiNi-Ni\ldots$$

Here, the interstitial configuration notation is the same as used in Sec. 2.6.1. This binding effect could conceivably be less severe in more concentrated Ni-Cr alloys. If the lattice in the vicinity of the CrCr dumbbell is sufficiently decorated with Cr atoms, then the escape of the dumbbell from the CrCr trap could be accomplished with the following series of changes in configuration:

$$CrCr-Ni \overset{+0.14eV}{\rightarrow} NiCr-Cr \overset{+0.21eV}{\rightarrow} CrNi-Cr \overset{+0eV}{\rightarrow} CrNi-Cr\ldots$$

where the total increase in binding energy is only 0.36 eV. The hop sequences for these two scenarios are illustrated schematically in Fig. 2.18.

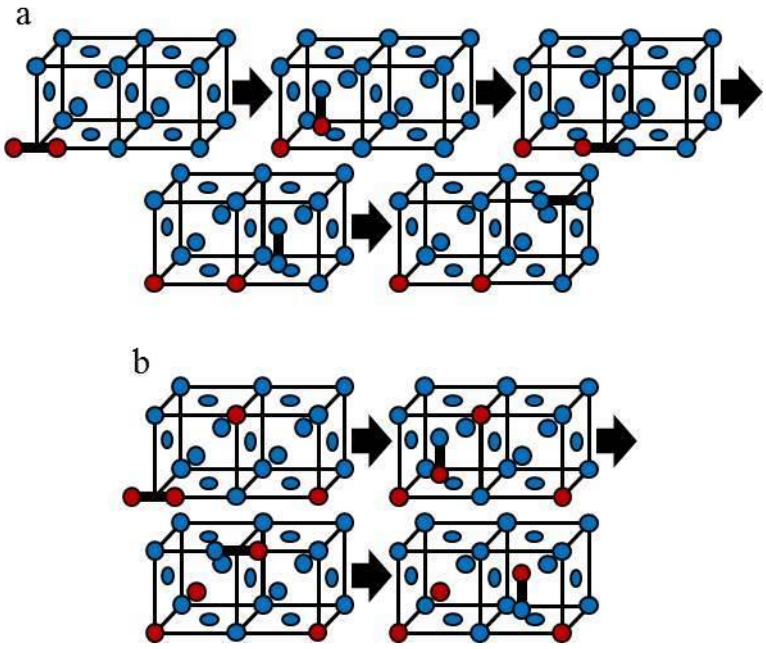

Figure 2.18: (top) Sequence of jumps required to dissociate an interstitial dumbbell from a CrCr trapping configuration in a dilute Ni-Cr alloy. (bottom) Sequence of jumps necessary to dissociate an interstitial dumbbell from a CrCr trapping configuration in a more concentrated Ni-Cr alloy.

In the second scenario, after escaping from the CrCr trap, long-range diffusion is accomplished by a sequence of alternating Ni and Cr interstitial hops that maintain the CrNi-Cr configuration after each hop. This sequence of jumps would be possible if there is an interconnected pathway of lattice sites that have at least one Cr nearest neighbor in a site accessible to the interstitial dumbbell. Assuming a random distribution of Cr atoms, the fraction of sites with at least one Cr neighbor is given by $1-C_{Ni}^{12}$, where C_{Ni} is the site fraction of Ni atoms. For a Ni-18Cr alloy, this yields a site fraction of 0.91, far greater than the site percolation threshold on an fcc lattice, which is approximately 0.2 [79]. Therefore, the CrCr interstitial trapping effect is a plausible cause of the reduced interstitial diffusion in the Ni-18Cr alloy, especially given that the untrapping energy of 0.36 eV in the scenario posited above is reasonably commensurate with both the fitted activation energies in Table 2.4 and the activation energy of interstitial migration in a Ni-16 Cr alloy, determined to be about 0.4 eV via resistivity recovery [78].

2.6.5 Implications for radiation-induced segregation

In the foregoing section, the results of AIMD simulations were used to determine interstitial diffusivities for both Ni and Cr in the Ni-18Cr model alloy. In this section, these diffusivities will be utilized in conjunction with the rate theory RIS model formulated in Sec. 2.2 to assess the role of interstitial diffusion in RIS in Ni-Cr alloys. In conventional Weidersich-type models [17] like the model developed in this study, qualitative RIS behavior is controlled by the ratios of the interstitial and vacancy diffusivities of the alloy species according to Eqn 2.11. Fig. 2.19 depicts interstitial and vacancy diffusivity ratios in Ni-Cr from multiple sources as a function of temperature, in a temperature range relevant to RIS.

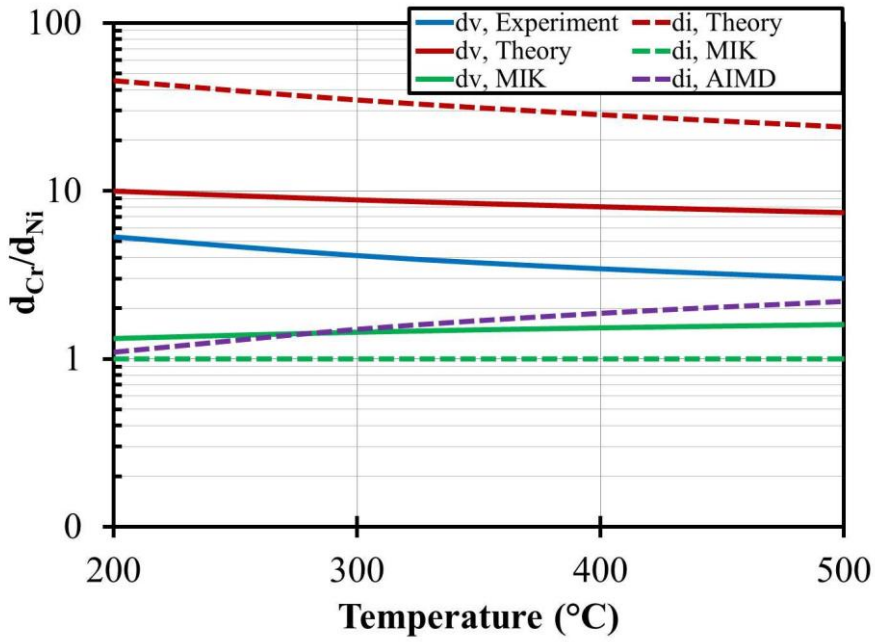

Figure 2.19: Interstitial and vacancy tracer diffusivity ratios in Ni-Cr determined from multiple sources (references in text).

The vacancy diffusivity ratios are depicted with solid lines, and the interstitial diffusivity ratios with dashed lines. The ratio of vacancy diffusivities from experimental measurements was determined from an Arrhenius fit to the average of available experimental data for Ni and Cr tracer diffusion in Ni [80, 81]. Ruzickova et al. [81] have demonstrated that the vacancy diffusivity ratio in Ni-Cr is independent of concentration up to 30 at% Cr; values determined in the dilute Ni-Cr regime are therefore a good approximation for all alloys within this composition range. The interstitial and vacancy diffusivity ratios from dilute alloy theory are taken from the work of Tucker et al. [22]. The interstitial diffusivity ratio in the Ni-18Cr alloy was obtained from the Arrhenius fit to simulation results of the present work, as described in Sec. 2.6.4. Finally, the modified Inverse Kirkendall (MIK) values for the diffusivity ratios were taken from the MIK model for RIS in Ni-18Cr [20].

For the vacancy diffusivities, in all cases the ratio is greater than one, indicating a tendency for vacancy diffusion to cause Cr depletion near defect sinks under irradiation. This tendency is predicted to be strongest by the dilute alloy theory results of Tucker et al. and weakest in the MIK model. There is no consensus regarding the role of interstitial diffusion in RIS in Ni-Cr alloys. In the MIK model, the interstitial diffusivity ratio is equal to 1 at all temperatures. This reflects a core assumption of the MIK model: that the interstitial flux shows no bias for either Cr or Ni and hence plays no role in RIS. Consequently, according to Eqn. 2.11, in the MIK model RIS is determined entirely by the vacancy diffusivity ratio. The interstitial diffusivity ratio from the dilute alloy theory result is greater than 1 at all temperatures, and is also greater than any value of the vacancy diffusivity ratio. According to Eqn. 211 and as demonstrated in Sec. 2.5, the dilute alloy theory diffusivity ratios would result in a prediction of significant Cr enrichment by RIS, in qualitative opposition to experimental measurements. The interstitial diffusivity ratio from the AIMD results is also greater than 1 at all temperatures, indicating a tendency for interstitial diffusion to cause Cr enrichment near defect sinks. This is in qualitative agreement with the dilute alloy theory, however the tendency is predicted to be much weaker from the AIMD results.

From Fig. 2.19, the AIMD results of this work combined with experimental measurements of tracer diffusion in Ni-Cr suggest the following physical description of RIS in Ni-Cr alloys: the interstitial flux exhibits a small bias for Cr transport, resulting in a tendency for Cr to be enriched near defect sinks. This bias is slightly weaker than the bias of the vacancy flux for Cr transport, which results in a counterbalancing tendency for Cr to be depleted near defect sinks. The net effect is moderate Cr depletion, driven by vacancy-mediated diffusion, in general

agreement with previous models for RIS [18, 20, 21, 23, 37, 48]. However, contrary to previous models for RIS in Ni-Cr, the AIMD results indicate that interstitial diffusion does in fact play an important role in RIS; namely, to moderate the Cr-depleting effect of vacancy diffusion and to reduce the observed Cr depletion.

In order to validate this physical description of RIS against experimental observations, RIS has been simulated using the rate theory RIS model formulated in Sec. 2.2. Fig. 2.20 depicts Cr depletion at 0.5 dpa as a function of temperature in a Ni-18Cr alloy, with experimental data from Allen et al. [11] and model predictions for three different model cases.

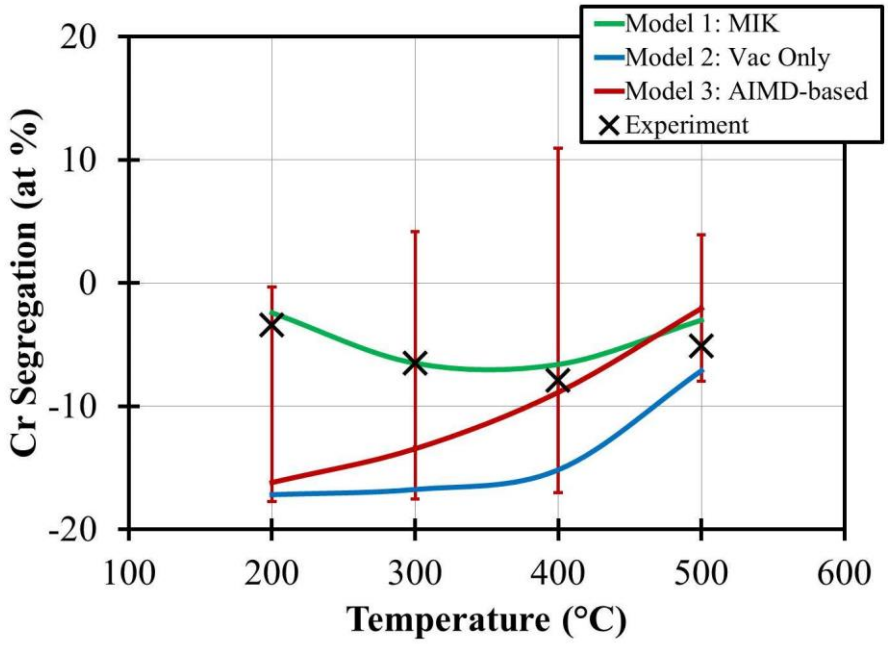

Figure 2.20: Cr segregation in a Ni-18Cr alloy after 0.5 dpa, as measured experimentally [11] and as predicted for 3 different model cases.

The first model case is the vacancy-only MIK model, in which the interstitial diffusivity ratio is equal to 1 at all temperatures, and the Ni and Cr vacancy diffusivities are determined via the MIK framework [20]. The second model case is also a vacancy-only description, however in this case the vacancy diffusivities are those determined from available experimental

measurements of Ni and Cr tracer diffusion [80, 81]. In the third model case, the experimental values for vacancy diffusivities are again used, however in this case the interstitial diffusivities are given by the Arrhenius fit to the AIMD simulations performed in this study. The uncertainty in the AIMD-based model predictions was determined as follows. The variances in d_{iCr} and d_{iNi} were first determined according to

$$\sigma^2(\ln d_{ik}) = \sigma^2(\ln d_{0k}) + \frac{1}{T^2}\sigma^2\left(\frac{E_{ak}}{k_b}\right) + \frac{2}{T}\sigma^2\left(\ln d_{0k}\cdot\frac{E_{ak}}{k_b}\right) \tag{2.30}$$

where $\sigma^2(\ln d_{ik})$ is the variance in $\ln d_{ik}$, $\sigma(\ln d_{0k})$ and $\sigma\left(\frac{E_{ak}}{k_b}\right)$ are the standard errors in the intercept and slope, respectively, of an Arrhenius fit to values of d_{ik} measured between 1200 and 1800 K via AIMD, and $\sigma^2\left(\ln d_{0k}\cdot\frac{E_{ak}}{k_b}\right)$ is the covariance between the intercept and the slope. These variances were then propagated to the variance in the ratio d_{iCr}/d_{iNi} via the following expression:

$$\sigma^2\left(\ln\frac{d_{iCr}}{d_{iNi}}\right) = \sigma^2(\ln d_{iCr}) + \sigma^2(\ln d_{iNi}) \tag{2.31}$$

The error bars in Fig. 2.20 reflect the extremes in RIS predictions that result from this variance in the ratio d_{iCr}/d_{iNi}.

From Fig. 2.20, it is clear that the MIK model provides the most accurate prediction of RIS as a function of temperature in the Ni-18Cr alloy. However, it is apparent from Fig. 2.19 that the Ni and Cr vacancy diffusivities used in the MIK model are not identical to the averages of the available experimental values for d_{vCr} and d_{vNi}, though they are within the experimental

uncertainty of these measurements. When the experimental values are used in a similar vacancy-only model, the result is a dramatic overprediction of Cr depletion. Including the interstitial diffusivities determined from AIMD simulations significantly reduces the predicted Cr depletion, resulting in reasonably accurate RIS predictions at high temperatures. At low temperatures, the AIMD-based model also overpredicts the Cr depletion, though not as drastically as the experimental vacancy-only model.

The experimental RIS measurements in Fig. 2.20 show a maximum in Cr segregation at 400 °C, with less severe Cr segregation at temperatures above and below. In the MIK framework, the ratio d_{vCr}/d_{vNi} approaches 1 at low temperatures, and as a result the MIK model captures this qualitative behavior quite well. This trend in the ratios is not observed in the AIMD-based model or the experimental vacancy-only model. Consequently, a significant qualitative discrepancy is observed between model cases two and three and experimental measurements: at temperatures below 400 °C, RIS measurements show gradually decreasing Cr segregation with decreasing temperature, while the AIMD-based model and the experimental vacancy-only model predict increasing Cr segregation as temperature decreases. One plausible explanation for this discrepancy is the treatment of the defect sink boundary condition in the RIS model cases presented in Fig. 2.20. For all three model cases, it has been assumed that the sink boundary is a grain boundary or free surface that behaves as a perfect defect sink, maintaining equilibrium defect concentrations in the vicinity of the sink. During the simulation, this means that every point defect that arrives at the sink boundary is instantaneously annihilated. As discussed in Sec. 2.4.1, Duh et al. [34] have derived an alternative boundary condition that includes the kinetics of this defect annihilation explicitly. In the model of Duh et al., the grain

boundary is described as an array of dislocations, and the efficiency of the defect annihilation is controlled by the flux of defects to the cores of these dislocations. At moderate and high temperatures and for large angle grain boundaries, this flux is very rapid relative to normal bulk diffusion and the sink approaches ideal sink behavior. However, for low temperatures or small angle grain boundaries, this flux is slower and the resulting RIS is suppressed with respect to the perfect sink case.

In order to assess whether this boundary condition effect can account for the qualitative discrepancy between the AIMD-based model and experimental measurements below 400 °C, the boundary condition formulation of Duh et al. has been applied to model cases 2 and 3. Fig. 2.21 depicts the model predictions of the AIMD-based model and the experimental vacancy-only model, respectively, utilizing the grain boundary condition derived by Duh et al. as well as the perfect sink boundary condition.

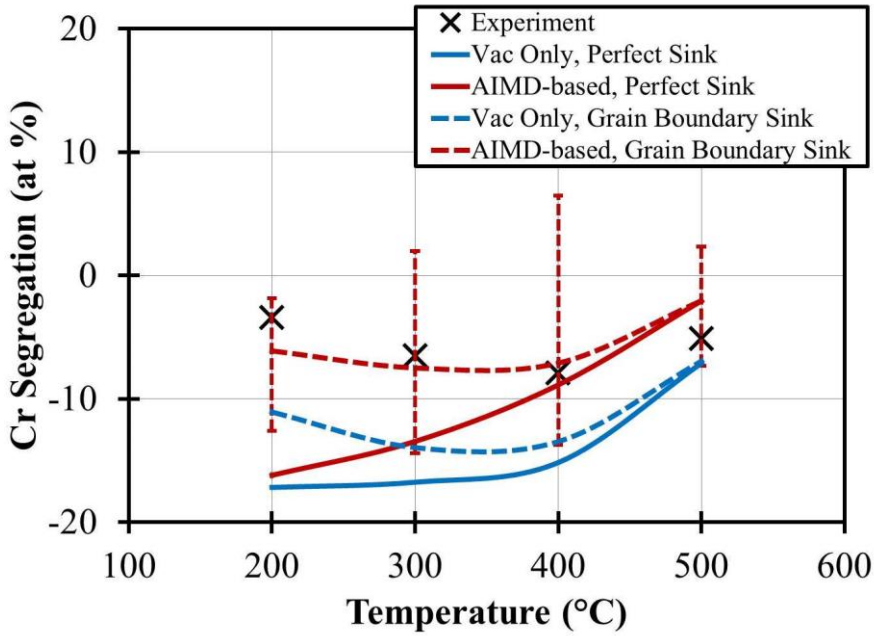

Figure 2.21: RIS model predictions using the ideal sink boundary condition and the grain boundary approximation boundary condition of Duh et al. [34]. The later boundary condition evaluates the defect flux into the grain boundary explicitly, while the former assumes that this flux is instantaneous. The boundary condition of Duh et al. yields much better agreement between model predictions and experimental measurements at low temperatures.

The model of Duh et al. was originally constructed to treat RIS in austenitic stainless steels and used grain boundary energies appropriate for that system. In this study, we instead use a grain boundary of 1 J/m^2, corresponding to the energy of a 30° tilt angle boundary in pure Ni, determined by Rittner and Seidman via EAM potentials [82]. A 30° boundary was chosen because it is a high energy boundary for which the model results should be most comparable to experimental measurements, in which general high angle grain boundaries are targeted for RIS measurement [34]. The high temperature model predictions are only very slightly affected by the change of the boundary condition, however at lower temperatures the Cr segregation is substantially reduced, in better qualitative agreement with experimental RIS measurements. The

AIMD-based model again predicts less severe Cr depletion and shows better overall agreement with RIS measurements than the experimental vacancy-only model.

We note that this modeling exercise suggests a very specific origin for the maximum in the magnitude of the RIS as a function of temperature and we reiterate the possible explanations here. At elevated temperatures, the vacancy concentration gradient near the grain boundary begins to disappear. Consequently, any non-equilibrium segregation near the grain boundary is counterbalanced by thermal vacancy diffusion and RIS is diminished. All models seem to reproduce this effect well. Then the RIS is expected to increase as temperature is lowered and the vacancy gradient grows. However, the observation that the magnitude of the RIS then decreases again at lower temperatures, leading to a maximum at intermediate temperature values (around 400 °C in Ni-Cr), has not been clearly explained. One possible explanation for this decrease in RIS at lower temperatures is that the diffusivity biases approach zero at low temperature, as was found for the MIK model. However, this explanation supposes essentially identical activation energies for the species responsible for RIS, which is unlikely in general and not consistent with DFT predictions in Ni-Cr. It is also possible that the reduced mobility of vacancy defects at lower temperatures simply shuts down the flux of vacancies to the boundary, thereby reducing RIS. However, while this flux is reduced at low temperatures, it is still significant enough to lead to measurable RIS from vacancy diffusion, as shown in Fig. 2.20. Vacancies must therefore not be entirely immobile at this temperature. What is proposed here is a new explanation, which is that the efficiency of the grain boundary as a defect sink is reduced at low temperatures, so that it can no longer be treated as an ideal sink. The defect gradients near the grain boundary are therefore less severe, and the resulting RIS is reduced. Model results

based upon this explanation are far more consistent with experimental measurements than when the ideal sink boundary condition is used.

The very large span of the error bars on the AIMD-based model predictions in Figs. 2.20 and 2.21 illustrates the highly sensitive nature of the Weidersich-type rate theory RIS model to the interstitial and vacancy diffusivities used as model parameters. Although the uncertainties on the parameters in Table 2.4 are not particularly large, small changes within the ranges of those uncertainties lead to dramatic changes in model predictions. It is evident from these error bars that the precision of the interstitial diffusivities determined in Sec. 2.6.4 is insufficient to produce a truly quantitative RIS model. Furthermore, additional uncertainty is introduced by the extrapolation of the Arrhenius function from high temperature simulation data to the temperature range relevant to RIS. At such low temperatures, non-Arrhenius contributions to the diffusion coefficient can become significant [22]. Furthermore, because the value of k_BT at the chosen simulation temperatures is commensurate with some of the interstitial migration energies, correlation effects that may play a strong role at low temperatures may not be well represented by the Arrhenius extrapolation. The uncertainty introduced by this extrapolation is not captured by the error bars in Figs. 2.20 and 2.21, which reflect only the uncertainty in the Arrhenius parameters. Additional errors inherent to the DFT method will also contribute to errors in the RIS predictions and are not included in the shown error bars.

Despite these significant quantitative uncertainties, the AIMD-based RIS model shows substantially better agreement with experimental RIS measurements than the experimental vacancy-only model, providing compelling evidence for the mediating role of interstitial

diffusion in RIS. We therefore conclude that the AIMD-based RIS model represents the most plausible qualitative physical description of RIS in Ni-Cr alloys to date.

2.7 Key Results and Conclusions

This chapter discussed the development of a model for simulating RIS and the application of this model to the Fe-Cr and Ni-Cr alloy systems, with parameters drawn from first principles calculations. The basic formulation of the model used an ideal sink boundary conditions and dilute alloy values for all tracer diffusivities. In the Fe-9Cr model alloy, this model predicted moderate Cr enrichment due to RIS, in good agreement with experimental measurements. In the model this enrichment was driven by fast Cr interstitial diffusion, providing evidence that interstitial defects play an important role in RIS in Fe-Cr and should not be neglected out of hand.

In the Ni-18Cr model alloy, the model predicted more severe Cr enrichment due to the same mechanism; however this was in contradiction of experimental measurements, in which moderate Cr depletion near grain boundaries was observed. In an effort to reconcile the model predictions with experimental observations, Cr-Cr interstitial trapping and interstitial-biased defect sinks were added to the model. While these had the effect of reducing the predicted Cr enrichment by a small amount, it was insufficient to bring the model into agreement with experiment. The lack of Cr-concentration dependence on the interstitial diffusivities in the Ni-Cr system was identified as a likely source of the errant model predictions, and AIMD simulations were utilized to determine concentrated alloy values of these parameters. When these parameters were used in lieu of the dilute alloy values, the RIS model predicted moderate Cr depletion in the Ni-18Cr model alloy, in reasonably good agreement with experiment. This modeling exercise

suggested the following mechanism for RIS in Ni-Cr alloys: vacancy diffusion tends to drive strong Cr depletion near grain boundaries, while interstitial diffusion drives a slightly weaker counterbalancing Cr enrichment, resulting in moderate Cr depletion overall. This description of RIS as a balance between vacancy and interstitial effects is novel and is the most physically plausible description of RIS in Ni-Cr alloys to date.

In both the Fe-Cr and Ni-Cr alloy systems, it was found that agreement with experimental measurements could be improved with a modified boundary condition that treated the defect sink as a true grain boundary, rather than as a perfect sink. In the Fe-9Cr alloy, this modification allowed the model to adequately capture the grain boundary angle effect on RIS, where high angle grain boundaries exhibited the strongest segregation, while low angle and CSL boundaries showed a weaker RIS effect. In the Ni-18Cr alloy, this modified boundary condition was necessary to reproduce the observed maximum in RIS magnitude occurring at intermediate temperatures. This modeling result suggests that the reduction in RIS magnitude at low temperatures is likely due to reduced sink strength in the grain boundary, a novel explanation for this phenomenon. When combined with the results of the Fe-Cr simulations, this result indicates that the defect sink kinetics should be treated explicitly in RIS modeling efforts, even if the grain boundaries of interest are high angle or high energy boundaries.

Chapter 3: Atomistic modeling of the order-disorder phase transformation in Ni-Cr alloys

3.1 Introduction and background

Alloys based on the Ni-Cr binary system are an important class of structural materials due to their strength, toughness, and excellent corrosion resistance. Alloys such as alloy 690 and

its weld metals are used extensively for structural components (e.g. piping) in nuclear power systems, where they can face service lifetimes exceeding 60 years. The long-term thermal stability of these alloys is therefore of critical importance. The Ni-Cr system exhibits an ordered phase at low temperatures (below about 570 °C) at the stoichiometry Ni_2Cr, and the evolution of this phase is one mode of thermal degradation that may be cause for concern. Ordering in this system can lead to hardening and embrittlement [83], as well as an increased susceptibility to environmentally assisted cracking [84, 85]. Furthermore, the molar volume of the ordered phase is smaller than the disordered alloy phase, and the lattice contraction associated with the phase transformation can lead to elevated stresses or the loss of dimensional tolerances [71, 86].

In addition to the binary Ni-Cr system, both short and long range ordering associated with the Ni_2Cr phase have been detected in Ni-Cr-Fe model alloys [87], and commercial grades (e.g., alloy 690) have shown evidence of Ni_2Cr-like short range ordering when aged above typical operating temperatures to accelerate their kinetics [86, 88-90]. The Ni_2Cr ordering transformation and the resulting impact on material properties is therefore of potential concern in commercial Ni-Cr alloys. However, due to the considerable breadth of components and compositions spanned by this class of alloys, the Ni-Cr model system alone, upon which many commercial grades are based, has been the focus of the present study . While the Ni-33Cr model alloy is itself not an alloy of interest for engineering applications, it may provide a lower bound for the timescale of the formation of Ni_2Cr-like long-range order. If it can be demonstrated that ordering is of no concern in Ni-33Cr, then ordering can most likely be dismissed for more complex commercial alloys in which the kinetics are generally slower at temperatures relevant to PWR operation [87, 88, 91].

The kinetics of the disorder-order phase transformation are relatively slow. In stoichiometric binary alloy Ni-33Cr, the ordering reaction takes on the order of 1,000 hours to proceed to completion at 450 °C [71, 86], while in more complex alloys aging times of tens of thousands of hours may be required before there is any evidence of Ni_2Cr associated long range ordering [90]. At typical pressurized water reactor (PWR) operating temperatures near 325 °C, the kinetics are much slower and the ordering process may take decades or more. It is therefore quite difficult from an experimental standpoint to study ordering kinetics at operating temperatures directly to determine whether it will be of concern on the timescale of the operational lifetime of a nuclear power system. Instead, the strategy has been to collect data at higher temperatures where the kinetics are significantly faster, and then use this data to fit empirical models to predict the timescale of the ordering transformation at the lower temperatures of interest [89, 90].

The ordering kinetics in such models typically depend upon an exponential term with an effective activation energy, and model predictions are highly sensitive to this parameter: values for Ni_2Cr ordering models are typically on the order of 100-200 kJ/mol (about 1-2 eV/atom), and a variation of only 10 kJ/mol (0.10 eV/atom) can result in a factor of 5-10 difference in predicted ordering times between 325 and 450 °C if all other model parameters are fixed [90]. Even near 450 °C, well above typical operating temperatures of interest, the ordering reaction may take many months or years depending upon alloy composition [88, 90]. It is therefore difficult to generate enough data to sufficiently constrain the model parameters, even for relatively simple empirical models. In a study of the ordering kinetics in alloy 690 (Ni-30Cr-10Fe), Delabrouille et al. [90] found that it was possible obtain a similar quality of fit to ordering data at 420 °C and

360 °C with activation energy values ranging from 78.5 to 124 kJ/mol, depending on the value of the athermal preexponential term. However, at 325 °C, this same range in model parameters results in predicted ordering times spanning approximately 30 to 110 years. As the lifespan of a typical PWR is 40 to 80 years, the need for a more rigorous prediction is clear.

The research discussed in this chapter was undertaken to provide a more robust model as well as to gain a better physical understanding of the kinetics of the ordering process in Ni-Cr alloys. The goal of this study is to utilize density functional theory (DFT) calculations combined with Monte Carlo simulations to develop a simple model for ordering in the Ni-33Cr alloy that is based upon first principles. This computational approach allows for the generation of a large body of simulated ordering data that covers a wide range of temperatures and has resulted in a well-constrained model that shows good quantitative agreement with data available in the literature as well as experimental data generated as a part of this study. Furthermore, insights gained from the atomic-level resolution of the simulations lend physical significance to the resulting model parameters and provide guidance for future model development.

The remainder of this chapter is organized as follows: in Sec. 3.2, the ordering model is described, and the details of the computational and experimental methods are recounted. Sec. 3.3 presents the significant thermodynamic and kinetic results derived from the Monte Carlo simulations. These simulation results are then used to construct the full first principles-based ordering model, and model predictions are compared with experimental measurements. Finally, concluding remarks are presented in Sec. 3.4 regarding the success and limitations of the model, and the implications for component lifetimes in PWR systems.

3.2 Theory, computation, and experimental method

The model framework developed in this project combined first principles-based Monte Carlo simulations with phase transformation theory to describe the kinetics of the disorder to order phase transformation in the Ni-33Cr model alloy. The steps involved in assembling this framework are detailed in this section. Experimental measurement of ordering kinetics is also discussed.

3.2.1 Kolmogorov-Johnson-Mehl-Avrami model for ordering kinetics in Ni-33Cr

The model used in this study to describe ordering in the Ni-33Cr alloy has the form of a Kolmogorov-Johnson-Mehl-Avrami (KJMA) equation [92-96]. This expression is used to describe a variety of phase transformations and related phenomena, and has the following general form:

$$S(t,T) = 1 - \exp\left[-(k(T)t)^n\right] \tag{3.1}$$

where $S(t,T)$ is a progress variable that varies continuously from 0 to 1 as the transformation proceeds from start to completion. The term $k(T)$ is a kinetic coefficient which is typically described by an Arrhenius form [93]

$$k(T) = k_0 \exp\left[\frac{-Q}{k_B T}\right] \tag{3.2}$$

Here, k_0 is the preexponential factor and Q is the effective activation energy for the ordering transformation. The time exponent *n* is known as the Avrami exponent, and typically relates to the nucleation and growth mechanism and the geometry of the newly growing phase. This parameter often assumes an integer value, though this is not always the case [97]. The ordering model thus has three adjustable parameters (k_0, Q, and *n*).

In principal the KJMA equation can be used to compute the extent of the disorder-order phase transformation at any time and temperature. Therefore, predicting the transformation kinetics during very long service lifetimes is straightforward once the KJMA equation has been parameterized. However, for these predictions to be accurate the parameters k_0, Q, and n must be determined by fitting Eqn. 3.1 to measurements of the ordered phase fraction that span a large breadth of temperatures and aging durations. At present, experimental measurements of the transformation kinetics below 450 °C are not available. We will therefore utilize atomistic simulations to generate a large set of measurements of the ordered phase fraction across several temperatures. Values of k_0, Q, and n are then obtained from fitting to these simulation results. This process is described in greater detail in section 3.3.

A complete description of the ordering process requires consideration of both the thermodynamic and kinetic aspects of the phase transformation. In this study, these aspects are addressed separately by distinct but related simulation techniques: the thermodynamics are treated using grand canonical Monte Carlo (GCMC) [98], while the kinetics are treated using kinetic Monte Carlo (KMC) [99]. Both simulation techniques were performed using the Cluster Assisted Statistical Mechanics (CASM) software package [100-102]. CASM is an integrated tool suite that is used to assemble a Hamiltonian in the cluster expansion formalism [103-105] and then use this Hamiltonian to implement lattice-based GCMC and KMC simulations. The requisite steps for implementing these tools are described in the following subsections.

3.2.2 Construction of the Ni-Cr-Vacancy cluster expansion

The GCMC and the KMC simulations, as implemented here, are fixed lattice methods in which the simulated system consists of atoms and vacancies occupying sites on a perfect, rigid

lattice. However, they are capable of representing any systems which are topologically equivalent to the fcc lattice, which includes the disordered Ni-Cr and Ni_2Cr ordered alloy. Because the ordering transformation occurs via vacancy-mediated atomic migration, vacant sites on the fcc lattice must also be included in the model. Thus, the simulated system consists of Ni atoms, Cr atoms, and dilute monovacancies distributed on an fcc lattice. The GCMC and the KMC simulations require a method to rapidly calculate the energy of any arbitrary arrangement of these occupants, and the means to do this is provided by the cluster expansion Hamiltonian.

In order to generate the cluster expansion Hamiltonian, it is first necessary to determine the energies of a finite representative set of Ni-Cr structures. This was done via density functional theory (DFT) calculations using the Vienna Ab Initio Simulations Package (VASP) [62-65]. All calculations were performed in the generalized gradient approximation (GGA) with the Perdew-Burke-Ernzerhof exchange-correlation functional [66] and the projector-augmented wave method [67]. An energy cutoff of 479 eV and k-point meshes of between 5000 and 7000 k-points per reciprocal atom in the Monkhorst Pack scheme were used, and all calculations were spin polarized. By this method, formation energies (from reference states of pure fcc Ni and pure fcc Cr) of 111 structures ranging in size from 1 to 108 atoms and spanning compositions from 0 to 50 % Cr were calculated. These formation energies were then used to fit the Ni-Cr cluster expansion in the occupation basis using CASM. The resulting cluster expansion Hamiltonian consists of 8 effective cluster interactions (ECIs), and has a cross validation (CV) score and root mean square (RMS) error of 0.039 and 0.023 eV per atom, respectively. The former value captures the ability of the cluster expansion to predict energies of structures not included in the fitting, while the latter is a measure of the error between predicted and calculated

energies when all structures are included in the fitting. Both the CV score and RMS error are on the order of 10-20% of the formation energy of the Ni_2Cr ordered structure. Fig. 3.1 depicts the formation energies of all Ni-Cr structures as predicted by the cluster expansion and as calculated via DFT as a function of alloy composition.

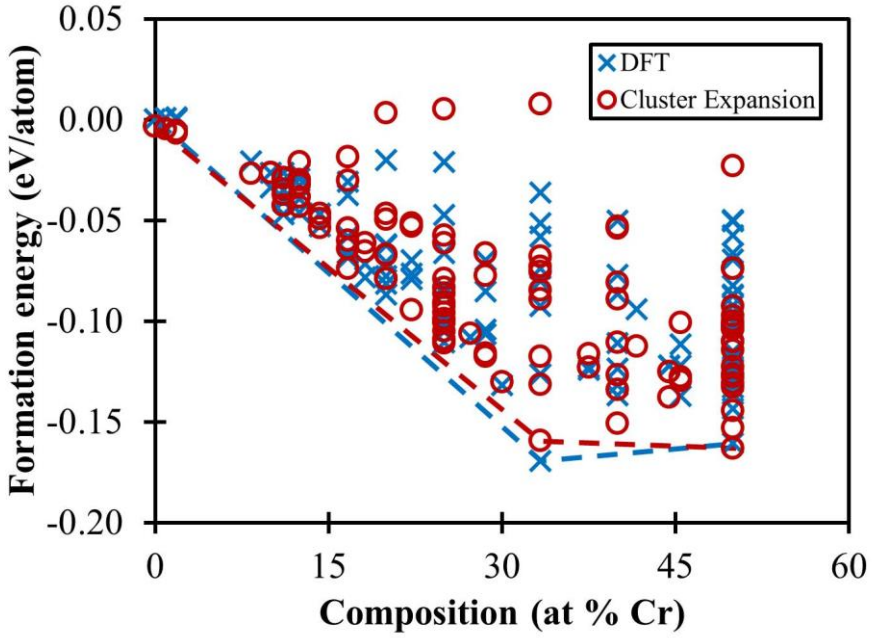

Figure 3.1: Comparison of cluster expansion predictions and DFT calculations of formation energies for all structures included in the Ni-Cr cluster expansion, as a function of at % Cr. The dashed lines represent the convex hulls of energies for the DFT values and the cluster expansion predictions.

In most cases the predictions of the cluster expansion and the DFT values are reasonably close, especially for structures near the convex hull. Both the DFT calculations and the cluster expansion Hamiltonian correctly predict the ground state at Ni-33Cr.

To capture interactions involving a vacancy, a separate cluster expansion was assembled to describe the vacancy formation energy following an approach similar to that used by Van der Ven et al. [106]. The vacancy formation energy is defined as the formation energy difference between a given Ni-Cr structure with a single vacancy and the same structure where the vacancy

has been replaced by a Ni atom, where again the structure formation energies are taken with respect to pure Ni and pure Cr reference states. Because the energy of the defected structure is taken with respect to a non-defected structure containing the same atomic interactions, the resulting cluster expansion captures only the atom-vacancy interactions. The vacancy formation energies of 15 structures were calculated and used to fit the vacancy cluster expansion in the occupation basis. The resulting cluster expansion Hamiltonian consists of 4 additional ECIs not already contained within the Ni-Cr cluster expansion, and has a CV score and RMS error of 0.0037 and 0.0003 eV, respectively. The CV score is on the order of 10 % of the Cr-vacancy interaction energies, which are around 50 meV in magnitude or smaller. The complete Ni-Cr-vacancy cluster expansion Hamiltonian thus contains 12 ECIs. These are presented in Table 2.1.

Table 3.1: ECIs in the Ni-Cr-Vacancy cluster expansion Hamiltonian for formation energies referenced to pure fcc phases. The Ni-Cr cluster expansion is in the spin basis, the Cr-Vac cluster expansion is in an occupation basis.

Composition	Number of constituents	Max Length (Å)	Multiplicity	ECI (meV)	ECI/multiplicity (meV)
Empty	0	0	1	-3	-3
Vac	1	0	1	0	0
Cr	1	0	1	-141	-141
Cr-Vac	2	2.51	12	643	54
Cr-Cr	2	2.51	6	304	51
Cr-Vac	2	3.55	6	136	23
Cr-Cr	2	3.55	3	-266	-89
Cr-Cr	2	4.35	12	-847	-71
Cr-Cr-Vac	3	2.51	24	-907	-38
Cr-Cr-Cr	3	4.35	24	938	39
Cr-Cr-Cr	3	4.35	24	806	34
Cr-Cr-Cr-Cr	4	3.55	12	-789	-66

3.2.3 Grand canonical Monte Carlo simulations

Once a suitable cluster expansion has been generated, it can be used to perform GCMC simulations in the CASM suite. Simulations were performed using a supercell consisting of 12x12x12 primitive fcc cells, for a total of 1,728 lattice sites. This supercell was initialized with all lattice sites occupied by Ni, and 10,000 passes were set aside for equilibration. During each pass, each lattice site is visited, on average, once to consider changing lattice occupancy based on the Metropolis algorithm for determining the correct probability for accepting or rejecting the occupancy change. After equilibration, an additional 80,000 passes were performed to compute thermodynamic averages.

The remaining input parameters for the GCMC simulations are the temperature and the reference state chemical potentials for each species in the system (μ_{Ni}, μ_{Cr}, and μ_{Vac}), which altogether define the coordinates in thermodynamic space of a given simulation. The reference state chemical potentials are used to determine the internal energy of a given configuration of the simulation cell, defined as the difference between energy of the configuration given by the cluster expansion and the sum of the energies of the constituents at their reference state chemical potentials. Because the number of lattice sites is fixed, the numbers of Ni, Cr, and vacancies are not independent variables. Consequently the three reference state chemical potentials for these species do not constitute three degrees of freedom. Therefore, one chemical potential is generally kept constant. In this study, we have chosen to consider Ni as the solvent species, and Cr and vacancies as solutes. The chemical potential of Ni is therefore fixed, and the remaining degrees of freedom are the chemical potential differences $\tilde{\mu}_{Cr} = \mu_{Cr} - \mu_{Ni}$ and $\tilde{\mu}_{Vac} = \mu_{Vac} - \mu_{Ni}$.

The difference $\tilde{\mu}_{Cr}$ largely determines the equilibrium alloy composition of the simulated system: as it is increased, the equilibrium composition will become more Cr-rich. In general, for a fixed value of $\tilde{\mu}_{Cr}$ the equilibrium alloy composition of the disordered phase will vary as a function of temperature, however in this case this variation was quite small: using a constant value chosen to yield a composition of Ni-33Cr at just above the order-disorder transformation temperature, the equilibrium simulated alloy composition remained within ±1 at% of Ni-33Cr between 600 and 1400 K (i. e., from well below the critical transformation temperature to well above it).

For a fixed value of $\tilde{\mu}_{Cr}$, the chemical potential difference $\tilde{\mu}_{Vac}$ determines the vacancy concentration in the simulated alloy. In real alloys at equilibrium, vacancies are not a conserved species, they may be emitted or absorbed freely by internal vacancy sources and sinks such as dislocations. Consequently, the equilibrium vacancy chemical potential is equal to zero and in principle the value $\tilde{\mu}_{Vac}$ of should be selected such that this condition for equilibrium is satisfied [27, 107]. However, equilibrium vacancy concentrations in real alloys are generally very dilute and computationally challenging to resolve via GCMC simulations. In this study, we have instead chosen $\tilde{\mu}_{Vac}$ such that there are many times the equilibrium concentration from real alloys but still, on average, fewer than one vacancy in the GCMC simulation cell at all temperatures. This is to avoid any vacany-vacancy interactions, which are not fit in the cluster expansion, and enable the approximations used below. The following additional manipulations were then used to estimate the vacancy concentration in the real Ni-33Cr alloy based upon the GCMC simulation results.

Van der Ven et al. [107] have derived the following expression for the vacancy fraction in GCMC simulations where the vacancies are sufficiently dilute that lattice configurations with more than one vacancy can be neglected:

$$C_{Vac} = -\frac{1}{Mk_BT}\left\langle \Delta\Phi_{Vac}(\vec{p})\right\rangle \tag{3.3}$$

where the quantity $\Delta\Phi_{Vac}(\vec{p})$ is referred to by Van der Ven et al. [107] as the coarse-grained vacancy free energy. This quantity is defined by

$$\Delta\Phi_{Vac}(\vec{p}) = -k_BT\sum_{\vec{q}(\vec{p})\neq\vec{p}}\exp\left[-\frac{\Delta\Omega(\vec{q}(\vec{p}))}{k_BT}\right] \tag{3.4}$$

Here, $\vec{p}$ specifies a binary Ni-Cr lattice configuration, $\vec{q}(\vec{p})$ specifies a configuration where a single vacancy has been inserted into configuration $\vec{p}$, and $\Omega(\vec{q}(\vec{p}))$ is the grand canonical energy of configuration $\vec{q}(\vec{p})$. The grand canonical energy is determined from the cluster expansion Hamiltonian, and is defined as

$$\Omega(\vec{s}) = E(\vec{s}) - N_{Cr}(\vec{s})\tilde{\mu}_{Cr} - N_{Vac}(\vec{s})\tilde{\mu}_{Vac} \tag{3.5}$$

where $N_{Cr}(\vec{s})$ and $N_{Vac}(\vec{s})$ are the numbers of Cr atoms and vacancies in configuration $\vec{s}$, respectively, and $E(\vec{s})$ is the cluster expansion energy of configuration $\vec{s}$. The change in grand canonical energy $\Delta\Omega(\vec{q}(\vec{p}))$ is the energy associated with introducing a vacancy into configuration $\vec{p}$, and is defined as

$$\Delta\Omega(\vec{q}(\vec{p})) = E(\vec{q}(\vec{p})) - N_{Cr}(\vec{q}(\vec{p}))\tilde{\mu}_{Cr} - \tilde{\mu}_{Vac} - \Omega(\vec{p}) \tag{3.6}$$

In Eqn. 3.6, we have implicitly assumed that the number of vacancies in all configurations $\vec{q}(\vec{p})$ is equal to 1. Combining Eqns. 3.3-3.6, we may now write the vacancy fraction as

$$C_{Vac} = \frac{1}{M}\exp\left[\frac{\tilde{\mu}_{Vac}}{k_B T}\right]\left\langle \sum_{\vec{q}(\vec{p})\neq\vec{p}} \exp\left[-\frac{E(\vec{q}(\vec{p})) - N_{Cr}(\vec{q}(\vec{p}))\tilde{\mu}_{Cr} - \Omega(\vec{p})}{k_B T}\right]\right\rangle \tag{3.7}$$

Let $C^*_{Vac}(C_{Cr})$ be the vacancy fraction determined via GCMC simulation in an alloy of Cr composition C_{Cr}, for an arbitrary value of $\tilde{\mu}_{Vac}$ chosen to yield a sufficiently dilute vacancy fraction. Further, let $R^*(C_{Cr})$ be the ratio $C^*_{Vac}(C_{Cr})/C^*_{Vac}(0)$ evaluated for a fixed value of $\tilde{\mu}_{Vac}$. From Eqn. 3.7 it is evident that the value of $R^*(C_{Cr})$ will be independent of the chosen value of $\tilde{\mu}_{Vac}$ due to cancelation. The vacancy fraction corresponding to any value of $\tilde{\mu}_{Vac}$ can be expressed as

$$C_{Vac}(C_{Cr}) = R^*(C_{Cr})C_{Vac}(0)\exp\left[\frac{\tilde{\mu}_{Vac}(C_{Cr}) - \tilde{\mu}_{Vac}(0)}{k_B T}\right] \tag{3.8}$$

where $\tilde{\mu}_{Vac}(C_{Cr})$ is the value of $\tilde{\mu}_{Vac}$ that results in the vacancy fraction $C_{Vac}(C_{Cr})$.

Because the equilibrium vacancy chemical potential is equal to zero, the chemical potential difference $\tilde{\mu}_{Vac}$ at equilibrium is equal to $-\mu_{Ni}$. By inserting this substitution into Eqn. 3.8, the equilibrium vacancy concentration in the Ni-33Cr alloy can be expressed as

$$C_{Vac}\left(\tfrac{1}{3}\right) = R^*\left(\tfrac{1}{3}\right)C_{Vac}(0)\exp\left[\frac{-\Delta\mu_{Ni}\left(\frac{1}{3}\right)}{k_B T}\right] \tag{3.9}$$

The value of $R^*\left(\frac{1}{3}\right)$ may be determined from GCMC simulations of pure Ni and the Ni-33Cr alloy, using a fixed value of $\tilde{\mu}_{Vac}$ that results in a sufficiently dilute vacancy fraction, and $C_{Vac}(0)$ can be drawn from experimental measurements of the vacancy concentration in pure Ni. The quantity $\Delta\mu_{Ni}\left(\frac{1}{3}\right) = \mu_{Ni}\left(\frac{1}{3}\right) - \mu_{Ni}(0)$ is the difference between the chemical potential of Ni in pure

Ni and in the Ni-33Cr alloy. Because the GCMC simulations are performed at fixed values of $\tilde{\mu}_{Cr}$ and $\tilde{\mu}_{Vac}$ the value of μ_{Ni} is not a controlled parameter. It can however be determined from GCMC simulation results in the Ni-Cr binary system (i. e., without vacancies) via thermodynamic integration according to the following method [108].

In a Ni-Cr alloy consisting of a fixed number of lattice sites, the chemical potentials of Ni and Cr can be expressed as follows [27]:

$$\begin{aligned} \mu_{Ni}(C_{Cr}) &= g(C_{Cr}) - C_{Cr}\frac{\partial g(C_{Cr})}{\partial C_{Cr}} \\ \mu_{Cri}(C_{Cr}) &= g(C_{Cr}) + (1 - C_{Cr})\frac{\partial g(C_{Cr})}{\partial C_{Cr}} \end{aligned} \tag{3.10}$$

where $g(C_{Cr})$ is the free energy per lattice site of the alloy. This free energy can be determined by the following integration:

$$g(C_{Cr}) = g(0) + \int_0^{C_{Cr}} \frac{\partial g(C'_{Cr})}{\partial C'_{Cr}} dC'_{Cr} \tag{3.11}$$

Inspection of Eqn. 3.10 reveals that the partial derivative $\frac{\partial g(C_{Cr})}{\partial C_{Cr}}$ is equal to the chemical potential difference $\tilde{\mu}_{Cr} = \mu_{Cr} - \mu_{Ni}$, which is fixed for any given GCMC simulation. Therefore, in practice the free energy can be evaluated by first performing a large number of GCMC simulations on a grid of $\tilde{\mu}_{Cr}$ values in order to populate a table of $\tilde{\mu}_{Cr}$ vs. C_{Cr} up to the alloy composition of interest, fitting a polynomial function $\tilde{\mu}_{Cr}(C_{Cr})$ to this data set, and computing the integral in Eqn. 3.11. Once the free energy $g(C_{Cr})$ has been determined, Eqn. 3.10 can be used to evaluate the chemical potential $\mu_{Ni}(C_{Cr})$. By following this procedure, the chemical

potential difference $\Delta\mu_{Ni}\left(\frac{1}{3}\right)$ can be calculated and subsequently used in Eqn. 3.9 to determine the equilibrium vacancy fraction in the real Ni-33Cr alloy.

In addition to the vacancy concentration, the GCMC simulations provide two other pieces of information that we make use of in this study. The first is the average grand canonical energy of the simulated Ni-Cr alloy as a function of temperature. While not of interest in itself, it is possible to identify the order-disorder transition temperature by observing the discontinuity in the average grand canonical energy of the simulated Ni-33Cr alloy, which is associated with the phase transformation. The second set of useful outputs are sample lattice arrangements of the equilibrated system, which can be used to calculate an ordering parameter and quantify the actual ordering of the simulated alloy. We define an ordering parameter as follows. In the ordered phase, all Ni atoms have 7 Ni neighbors and 5 Cr neighbors, while all Cr atoms have 10 Ni neighbors and 2 Cr neighbors. In this study, we consider the atoms in the system that have the "correct" neighbors to be "ordered atoms," and the extent of ordering is quantified by the fraction X_O of ordered atoms in the system. This leads to the following definition of the KJMA progress variable in Eqn. 3.1:

$$S(t,T)=\frac{X_O(t,T)-X_{O,\min}}{1-X_{O,\min}} \tag{3.12}$$

where $X_{O,\min}$ is the fraction of ordered atoms in the disordered phase just above the Ni_2Cr order-disorder critical temperature, and $X_O(t,T)$ is the ordered fraction in the system at time t and temperature T. While time is not a meaningful parameter in the GCMC simulations, it is included here for clarity, as this same definition of the progress variable will be used for analyzing the results of the KMC simulations. Note that this variable changes from 0, for the

equilibrium state of the disordered phase at just above the critical temperature, to 1, for the perfect ordered phase.

3.2.4 Kinetic Monte Carlo simulation

The KMC functionality of the CASM software package was used to study the kinetic aspects of the ordering transformation in Ni-33Cr. The KMC method as implemented in CASM simulates the time evolution of the system that occurs due to the migration of a single vacancy, thus the vacancy concentration in the simulation is implicitly determined by the selection of the system size. In the present study, the KMC simulation supercell consisted of 27x27x27 primitive fcc cells, for a total of 19,683 lattice sites. Unlike in the GCMC simulations, for KMC simulations the atomic composition of the simulated system is entered by the user explicitly; for all simulations, a composition of Ni-33Cr was used in a random initial lattice arrangement.

The frequencies of atomic migration events are determined by the KMC algorithm using the familiar expression from standard transition state theory [109]:

$$\omega_{i\to j} = \nu \exp\left[-\frac{E_{i\to j}}{k_B T}\right] \tag{3.13}$$

where $\omega_{i\to j}$ is the hopping frequency for a given atom from configuration *i* to configuration *j*, ν is the attempt frequency, and $E_{i\to j}$ is the migration energy for the hop. Most estimates for attempt frequencies in metals range from 10^{12}-10^{13} Hz. In this study we have used an approximate value of 10^{13} Hz for all events. The migration barrier $E_{i\to j}$ is approximated dynamically by the kinetically resolved activation barrier (KRA) method [74, 110]:

$$E_{i\to j} = E_0 - \frac{1}{2}\left(E_i - E_j\right) \tag{3.14}$$

where E_0 is the baseline migration barrier, and E_i and E_j are the energies of the initial and final state configurations as determined by the cluster expansion Hamiltonian. The determination of the KRA barrier is depicted geometrically in Fig. 3.2.

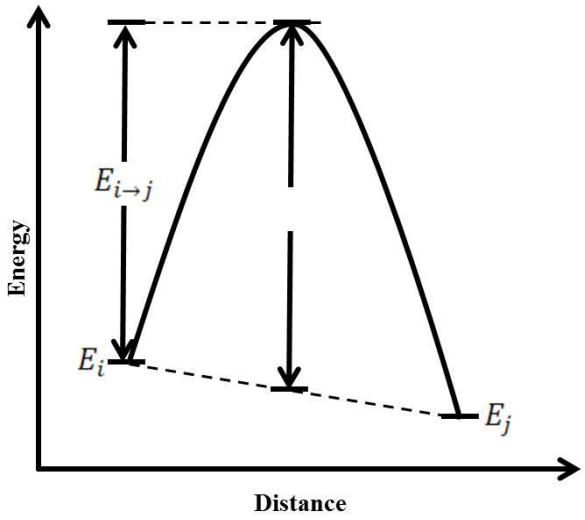

Figure 3.2: Geometric depiction of the kinetically resolved activation barrier.

E_0 values of 1.04 eV and 0.83 eV were used for Ni and Cr, respectively. The former is the experimentally determined value for pure Ni self-diffusion [111], and the latter is the migration barrier for Cr in pure Ni determined via DFT [22]. While this neglects any potential effect of the local chemical environment on the baseline migration barrier, we assume that the majority of the effect of the local environment will be captured by the KRA treatment. This approach has been demonstrated to be a reasonable approximation in other systems [112].

Simulations were run of lengths varying from 1 to 100 passes, in increments of 5 passes, where a pass is defined as one vacancy hop for every lattice site in the system. At the end of each simulation, the final simulation time was collected and the final configuration of the lattice was used to compute the value of the progress variable $S(t,T)$. Thus, each point in S-time-

temperature space represents a separate, independent simulation. Simulations were performed at 327 °C, 375 °C, 423 °C, and 471 °C, with 5 sets of simulations at each temperature, for a total of 105 simulations. The resulting values of $S(t,T)$ as a function of time and temperature were used to fit the values of the parameters k_0, Q, and n in Eqn. 3.1.

3.2.5 Experimental measurement of the ordering kinetics in Ni-33Cr

In order to provide a benchmark for the model results, a set of experimental data on the ordering kinetics of Ni-33Cr was gathered between 333 °C and 470 °C for aging times up to 10,000 hours. While sufficient experimental data exists for temperatures above 450 °C [71, 88] the present study will provide critical lower temperature data points, so that model predictions can be validated across a wider temperature range. Because ordering is an atomic scale phenomenon, it can be difficult to characterize by direct observation techniques such x-ray diffraction due to the close scattering properties of Ni and Cr. It is therefore most often characterized indirectly by measuring some other property of the material that changes in response to the ordering process, such as hardness, fracture properties, or electrical resistivity [86]. In this study, the change in the lattice parameter is used to quantify the ordering process.

The model alloy was fabricated by arc melting 300 g buttons at the nominal composition Ni-33Cr. After melting, the buttons were annealed for 24 hours at 1093 °C and hot rolled between 982-1093 °C from approximately 10 mm to 5 mm in thickness in three passes, with the rolling direction of the second pass aligned perpendicular to the first and third passes. Following rolling, the buttons were annealed at 1093 °C for one hour and then quenched.

Once the specimens were fabricated, 1.25 cm square samples were machined and grouped for isothermal aging at 4 temperatures: 333 °C, 373 °C, 418 °C, and 470 °C. The cubic

lattice parameters of select samples were measured prior to aging, and all samples were measured after aging increments of 10, 30, 100, 300, 1,000, 3,000, and 10,000 hours. Lattice parameters were determined via X-ray diffraction, performed with a PANalytical X'Pert Pro Theta-Theta diffractometer and Cu Kα radiation. Parallel beam optics and high angle diffraction peaks (the (3,3,1) and (4,2,0) planes at ≈140° and ≈150° 2θ, respectively) were used to minimize instrumental errors. In addition, an Alloy 690 external standard was tested periodically to check for instrumental errors.

3.3 Results and discussion

3.3.1 Determination of the critical temperature and the fraction of ordered atoms from GCMC simulations

One immediate assessment of accuracy of the cluster expansion Hamiltonian is the predicted critical temperature T_C for the order-disorder transition. Fig. 3.3 depicts the grand canonical energy of the simulated Ni-33Cr alloy as a function of temperature, as determined via GCMC simulations.

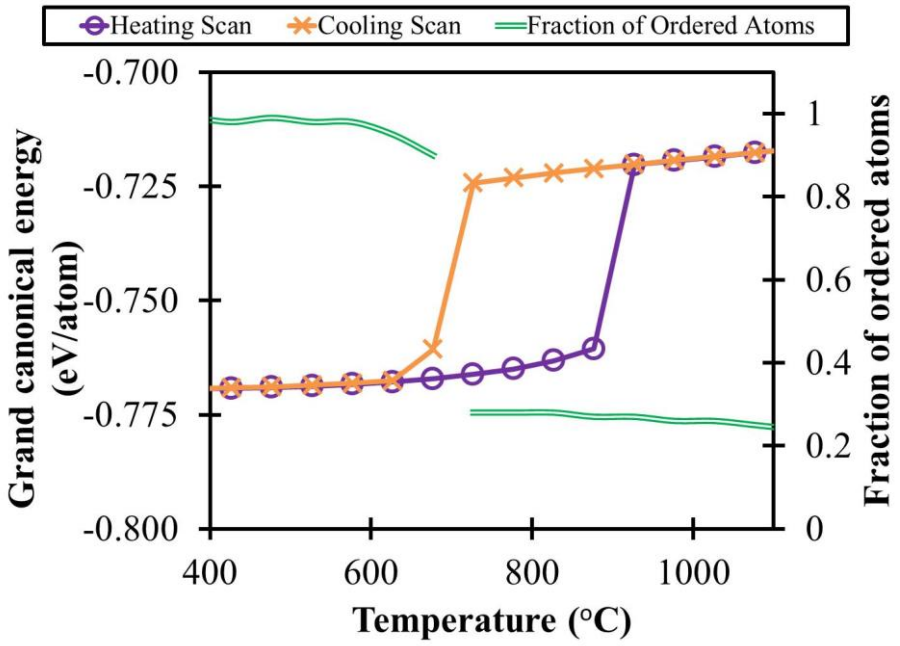

Figure 3.3: Grand canonical energy and ordered fraction as functions of temperature, determined via GCMC for the simulated Ni-33Cr alloy

Temperatures were sampled with both heating and cooling scans in order to place upper and lower bounds on the simulated critical temperature. The sharp discontinuities at 677 °C for the cooling scan and 877 °C for the heating scan indicate phase transformations during the simulations. On the secondary vertical axis in Fig. 3.3 the fraction of ordered atoms in the system is plotted as a function of simulation temperature during the cooling scan. The sharp increase from 0.28 to near 1 as the system is cooled through approximately 677 °C verifies that this phase transformation is the transition between the disordered alloy phase and the ordered Ni_2Cr phase. The predicted value for T_C is thus between 677 and 877 °C. This is higher than the experimental values of 570-590 °C [71, 88, 113]. This discrepancy may be due to errors in the ab initio energies, the cluster expansion, or vibrational and magnetic contributions to the free energy that are neglected in the computation of the grand canonical potential. In light of these

approximations the predicted value of T_C is reasonable, and indicates that the cluster expansion Hamiltonian adequately describes the phase transformation.

In a truly random Ni-33Cr alloy, the average fraction of atoms having the "correct" numbers of Ni and Cr neighbors by happenstance is about 0.17. It is noteworthy that the ordered fraction just above the critical temperature $X_{O,\min}$ in Fig. 3.3 is about 0.28, which is somewhat higher than the random alloy value. This reflects the persistence of some degree of short-range order above the critical temperature.

3.3.2 Determination of the KJMA parameters from KMC simulations

In order to construct the first principles-based KJMA model, we first introduce a slightly altered form of the kinetic coefficient $k(T)$:

$$k(T) = k_0 C_{Vac} \exp\left[-\frac{Q_{mig}}{k_B T} \right] \tag{3.15}$$

where C_{Vac} is the vacancy concentration in the simulated Ni-33Cr alloy. We assume that the order-disorder phase transformation proceeds via discrete atom-vacancy exchanges [114], so we assume here that the kinetic coefficient is proportional to the vacancy concentration. The activation energy Q_{mig} is then the portion of the activation energy associated with these atom-vacancy exchanges. In a real alloy, the vacancy concentration will have a strong temperature dependence that will be reflected in the total effective activation energy Q in Eqn. 3.2, however in the KMC simulations the vacancy concentration is determined implicitly by the selection of the system size, as discussed in Sec. 3.2.4.

The first principles-based KJMA model was constructed by performing a least squares fit of Eqn. 3.1 to values of the order parameter $S(t,T)$ determined from KMC simulations, using pre-exponential factor k_0, the activation energy Q_{mig}, and the Avrami exponent *n* as fitting parameters. Values of the order parameter as a function of time are plotted in Fig. 3.4 for four different temperatures.

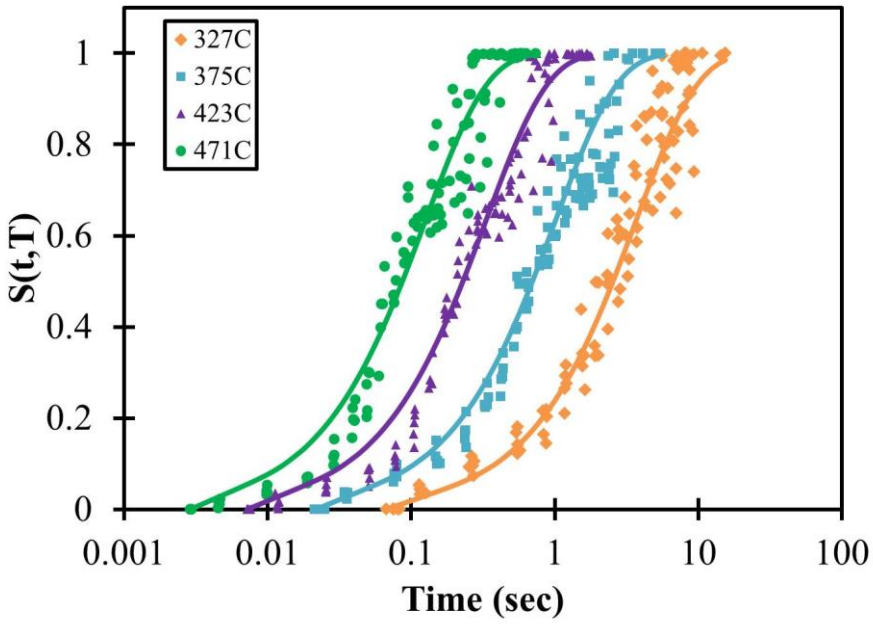

Figure 3.4: KMC simulations results for order parameter $S(t,T)$ as a function of time, at 4 different temperatures. Solid lines are the best-fit KJMA model to the simulation data.

The data points represent values measured from KMC simulations, while the solid lines are values from the best-fit KJMA model. The best fit model in Fig. 3.4 produces the following values for the KJMA parameters: k_0 = 2.04×10^{11} Hz, Q_{mig} = 0.9 eV, and *n* = 1. Because these parameters are independent of the system size, the results of this model may be compared directly to experimental measurements of the ordering kinetics by inserting the vacancy concentration of the real Ni-33Cr alloy into Eqn. 3.15. A precise value of this vacancy

concentration is unavailable for the Ni-33Cr alloy, however GCMC simulations can be utilized to estimate how much this value might differ from the vacancy concentration in pure Ni, which has been determined experimentally. This estimation approach will be demonstrated in section 3.3.4.

3.3.3 Physical interpretation of the KJMA model

The value of the Avrami exponent *n* is often interpreted in terms of the nucleation and growth mechanism of the growing phase. For instance, for site saturated nucleation and diffusion controlled growth, *n* is equal to 1, 2, or 3 and reflects the dimensionality of the growth [94-96]. In this section, we posit a simple model for the kinetics of the ordering transformation to provide a physical interpretation of the KJMA model assembled in Sec. 3.3.2.

In keeping with the original derivation of the KJMA equation [92], we first define a fictitious extended fraction of ordered atoms, X_{ext}, as the fraction of ordered atoms that would result if the growing domains of the ordered phase never impinged upon one another. We assume that the ordering transformation proceeds by a series of atom-vacancy exchanges that rearrange the disordered atomic structure to the ordered structure at some constant, effective rate. Furthermore we assume that, to a first approximation, vacancies remain for the most part in the disordered phase, and do not spend significant time in diffusing through ordered material. Consequently, the volume growth rate of the ordered phase domains is independent of the domain size. This is in contrast with the volume growth rate under diffusion controlled growth conditions, where the growth rate is proportional to a flow of material across the interface of the domain of the newly growing phase. This flow is proportional to the interfacial area of the domain; as the domain grows, the growth rate increases according to some power law of time,

depending on the dimensionality of the growth. A disorder-order transformation rate that is constant with respect to time was also proposed by Dienes [115] for a place-exchange mechanism and Vineyard [114] for a vacancy mechanism, with greater theoretical rigor than the simple model proposed here.

Subject to these assumptions, the differential change of the extended ordered fraction can be expressed as

$$dX_{ext} = C_{Vac} k_{ord} dt \tag{3.16}$$

where k_{ord} is the average rate at which a one atom is transformed from a disordered atom to an ordered atom by a series of atom-vacancy exchanges. The differential extended ordered fraction is related to the differential real ordered fraction X_O by

$$dX_O = (1 - X_O) dX_{ext} \tag{3.17}$$

After combining Eqns. 3.16 and 3.17 and integrating, and recalling that $X_O(0) = X_{O,\min}$ we arrive at the following expression for the ordered fraction as a function of time:

$$X_O(t) = 1 - \exp\left[-C_{Vac} k_{ord} t\right](1 - X_{O,\min}) \tag{3.18}$$

Combining Eqns. 3.18 and 3.12, we recover the original functional form of the KJMA equation:

$$S(t) = 1 - \exp\left[-C_{Vac} k_{ord} t\right] \tag{3.19}$$

The value of 1 for the Avrami exponent that resulted from the least squares fitting in Sec. 3.3.2 is evidently a consequence of the physical growth mechanism reflected in Eqn. 3.16; namely, that the volume of the extended ordered phase fraction grows at a constant rate. It is therefore not related to the dimensionality of the growing domains, as is conventionally assumed for diffusion-controlled phase transformations described by the KJMA equation.

3.3.4 Estimation of the vacancy concentration in the Ni-33Cr alloy

Before the results of the KJMA model obtained in Sec. 3.3.2 can be used to predict the ordering transformation kinetics in a real Ni-33Cr model alloy, a value of the vacancy concentration in the alloy must be determined. The method described in Sec. 3.2.3 was used to determine the parameters $R^*\left(\frac{1}{3}\right)$ and $\Delta\mu_{Ni}\left(\frac{1}{3}\right)$ on the temperature range between 950 and 1200 K. The results of these calculations are presented in Fig. 3.5.

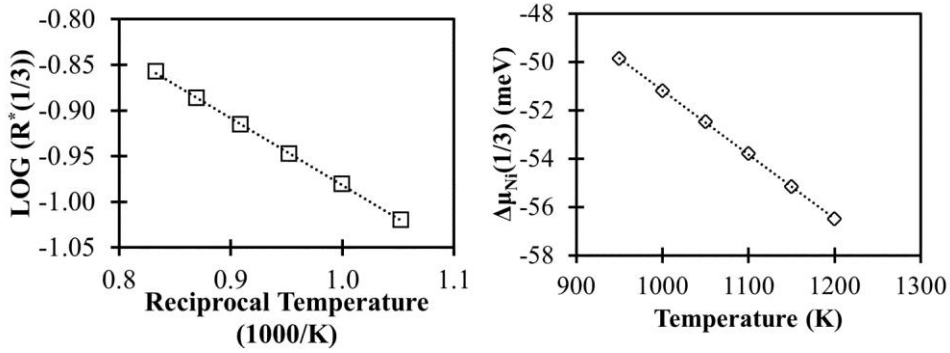

Figure 3.5: (left) Ratio $R^*\left(\frac{1}{3}\right)$ determined from GCMC simulations. b (right): chemical potential difference $\Delta\mu_{Ni}\left(\frac{1}{3}\right)$ determined from thermodynamic integration of GCMC simulations in the Ni-Cr binary system.

The values of the ratio $R^*\left(\frac{1}{3}\right)$ are consistent with the Arrhenius expression

$$R^*\left(\tfrac{1}{3}\right) = R_0^* \exp\left[-\frac{E_R}{k_B T}\right] \tag{3.20}$$

where R_0^* = 0.57 and E_R = 0.15 eV. The values of $\Delta\mu_{Ni}\left(\frac{1}{3}\right)$ follow the form

$$\Delta\mu_{Ni}\left(\tfrac{1}{3}\right) = A + BT \tag{3.21}$$

with parameter values A = -0.024 eV and B = -2.68×10^{-5} eV/K. We have used these functional forms to extrapolate the value of the vacancy fraction to the temperature range where the disorder to order phase transformation occurs. This extrapolation from higher temperature was

performed because the kinetics of the phase transformation are likely governed by the vacancy concentration in the solid solution phase, while direct evaluation by GCMC at low temperature would yield information only about the vacancy concentration in the ordered phase.

The ratio $C_{Vac}\left(\frac{1}{3}\right)/C_{Vac}(0)$ is equal to the product $R^*\left(\frac{1}{3}\right)\exp\left[-\frac{\Delta\mu_{Ni}\left(\frac{1}{3}\right)}{k_BT}\right]$, and from Eqns. 3.20 and 3.21this ratio has a value between about 0.15 and 0.23 over the temperature range 950 to 1200 K. The vacancy concentration in the Ni-33Cr alloy is therefore predicted to be lower than in pure Ni. This result is in qualitative agreement with experimental diffusion measurements, which show that Ni and Cr diffusion coefficients decrease with increasing Cr concentration, down to a minimum near 30 at% Cr [45].

In order to complete the evaluation of the vacancy concentration in the Ni-33Cr alloy, the vacancy concentration in pure Ni must be established. We assume that this vacancy concentration can be described by the general form

$$C_{Vac}(0) = \exp\left[\frac{-H_{Vac}(0)}{k_BT}\right]\exp\left[\frac{S_{Vac}(0)}{k_B}\right] \tag{3.22}$$

where $H_{Vac}(0)$ and $S_{Vac}(0)$ are the vacancy formation enthalpy and entropy in pure Ni. Suggested values of these parameters range from 1.55-1.8 eV [22, 111, 116-121] and from 1 – 5 k_B [22, 116, 119, 121], including both experimental measurements and theoretical calculations. Values of 1.6 eV and 1.1 k_B from within this range were chosen to yield the best model agreement with experimental measurements of ordering kinetics.

3.3.5 Determination of the lattice parameters of the ordered and disordered phases

In order to relate the model predictions to experimental measurements of the change in lattice parameter as a function of aging time and temperature, the order parameter $S(t,T)$ must be related to a change in lattice parameter $\Delta a(t,T)$. As a first approximation, we assume that the lattice parameter changes linearly as the order parameter progresses from 0 to 1. In order to complete the model, lattice parameters of the disordered and ordered phases must be therefore determined. This information cannot be obtained from the GCMC or KMC simulations, however the lattice parameters can be calculated directly via DFT. To best capture the lattice parameter of the disordered phase, the structure produced by the GCMC simulations at 1000 °C was utilized. Because the GCMC simulation cell itself is far too large for a DFT calculation, several small cubic samples of this structure were carved out, each consisting of a 3×3×3 cubic fcc supercell and containing 108 atoms. The lattice parameters of these cubic sample cells were averaged to obtain the lattice parameter of the disordered phase. A supercell with the Ni_2Cr lattice arrangement of the same size and dimensions was used to determine the lattice parameter of the ordered phase. The cubic lattice parameters were calculated by first relaxing each of these supercells internally, then relaxing the volumes of the supercells without allowing the shape to change. By this method, the change in lattice parameter due to complete phase transformation from the disordered to the ordered structure was determined to be -0.26±0.02 %.

3.3.6 Comparison of model predictions to experimental measurement

The complete first principles-based model can now be constructed, and the results compared directly to experimental measurements of the change in lattice parameter, *a*, as a function of time and aging temperature. The complete model may be expressed as follows:

$$\Delta a(t,T) = \Delta a_{D\to O}\left(1-\exp\left[-\left(k(T)t\right)^n\right]\right)$$
$$k(T) = k_{eff}\exp\left[-\frac{Q_{eff}}{k_B T}\right] \tag{3.23}$$

where Q_{eff} and k_{eff} are the effective preexponential factor and activation energy of the ordering reaction, defined as follows:

$$Q_{eff} = H_{Vac}(0) + E_R + A + Q_{mig}$$
$$k_{eff} = k_0 R_0^* \exp\left[\frac{S_{Vac}(0) - B}{k_B}\right] \tag{3.24}$$

The descriptions and values of the parameters in Eqns. 3.23 and 3.24 are summarized in Table 3.2.

Table 3.2: Parameter definitions and values for the complete first principles-based model

Symbol	Description	Value	Source
$\Delta a_{D\to O}$	Maximum lattice change	-0.26 %	DFT + GCMC
n	Avrami exponent	1	Fit of Eqn. 3.15 to KMC data
$k(T)$	KJMA kinetic coefficient		Eqn. 3.23
Q_{eff}	Effective activation energy	2.62 eV	Eqn. 3.24
k_{eff}	Effective preexponential factor	4.3×10^{11} Hz	Eqn 3.24
$H_{Vac}(0)$	Pure Ni vacancy formation enthalpy	1.6 eV	Best fit within range of experiments
E_R	Activation energy from Arrhenius fit to $R^*\left(\frac{1}{3}\right)$	0.15 eV	Fit of Eqn. 3.20 to GCMC results
A	Intercept from linear fit to $\Delta\mu_{Ni}\left(\frac{1}{3}\right)$	-0.024 eV	Fit of Eqn. 3.21 to GCMC results
Q_{mig}	Atomic migration component of the ordering activation energy	0.9 eV	Fit of Eqn. 3.15 to KMC data
$S_{Vac}(0)$	Pure Ni vacancy formation entropy	1.1 k_B	Best fit within range of experiments
k_0	KJMA preexponential factor	2.04×10^{11} Hz	Fit of Eqn. 3.15 to KMC data
R_0^*	Preexponential factor from Arrhenius fit to $R^*\left(\frac{1}{3}\right)$	0.57	Fit of Eqn. 3.20 to GCMC results
B	Slope from linear fit to $\Delta\mu_{Ni}\left(\frac{1}{3}\right)$	-2.68×10^{-5} eV/K	Fit of Eqn. 3.21 to GCMC results

Fig. 3.6 presents experimental measurements and model calculations of the change in lattice parameter in a Ni-33Cr alloy as a function of time during aging at temperatures between 333 °C and 470 °C (measurements of Marucco [88] taken at 475 °C).

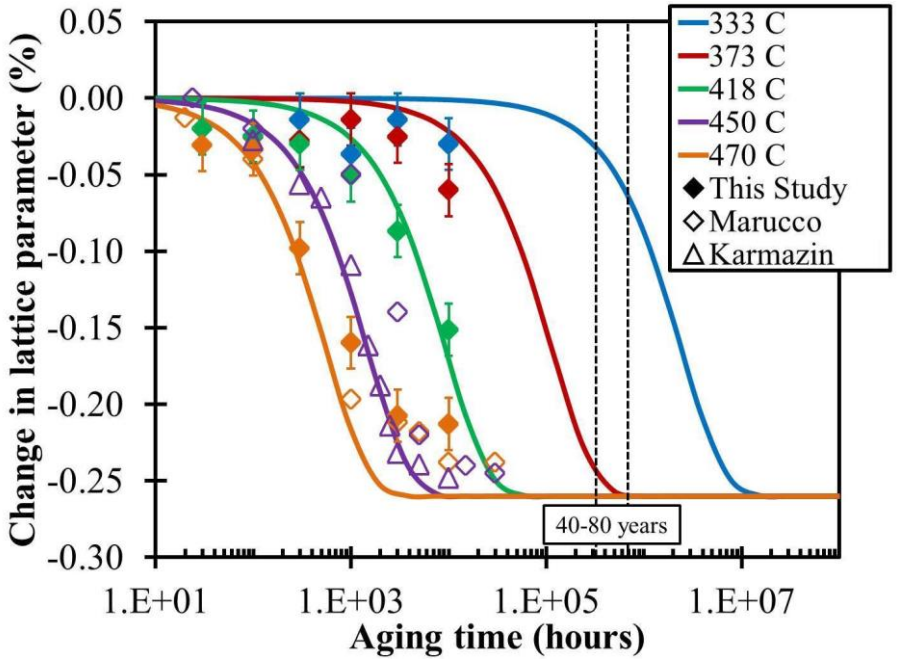

Figure 3.6: Change in lattice parameter of a Ni-33Cr model alloy as a function of time as measured experimentally, and corresponding predictions of the first-principles based model.

The data points represent experimental measurements generated in this study as well as data available from the literature [71, 88], while the solid lines depict the results of the model. The error bars in on the experimental data generated in this study represent a range of one standard deviation on the individual measurements, computed using a pooled variance estimate across replicate as-fabricated specimens from the various buttons.

Reasonable agreement between the model and experiment is observed for temperatures above 373 °C, and for aging times longer than 100 hours. For shorter aging times, there is some experimental evidence of a small lattice contraction that is not captured by the model. This initial decrease in lattice parameter may be due to the population of excess vacancies present in the alloy after quenching from the annealing temperature. These vacancies would temporarily accelerate the transformation until they have been annealed out. Notably, the smallest early

decrease in lattice parameter is observed in the data of Marucco [88], who heat treated specimens at 700 °C before quenching. Presumably, this would result in a much smaller population of excess vacancies compared to the present study and the study of Karmazin, in which heat treatments were performed at 1000 °C or above [71].

At 333 and 373 °C, the model predicts that there should be no significant change in the lattice parameter before 3,000 hours, in broad qualitative agreement with experimental measurements at these temperatures. While there is some measured change in lattice parameter at these temperatures, it is minor and does not follow a discernible consistent trend of increasing lattice contraction with longer aging. At 373 °C, the model predicts that a modest degree of lattice contraction will occur by 10,000 hours, in qualitative agreement with the experimental data, though the predicted lattice contraction is less than the measured amount. The model predicts that no significant lattice contraction will occur by 10,000 hours at 333 °C, although a very small contraction is measured for this aging condition. This measured lattice contraction is not significantly different from measurements taken after shorter aging times at 333 °C, and therefore does not appear to indicate that a significant degree of ordering transformation has yet occurred.

A notable discrepancy exists between the model predictions and many experimental measurements for lattice contractions larger in magnitude than about 0.2 %. This discrepancy may be attributed to the difference between the predicted value for the maximum change in lattice parameter and experimental measurement: the DFT calculations predict a change of -0.26±0.02 %, while in most cases the observed lattice contraction does not exceed about -0.24 % [71, 88]. Aside from DFT error in the lattice parameters, one other possible reason for this

discrepancy is that complete ordering is typically not achieved experimentally. In a real alloy, as ordered domains grow they interact with nearby domains elastically due to misfit strains at the order-disorder interface, and this interaction impedes further growth. Consequently some small phase fraction of disordered material remains [87] and the change in lattice parameter saturates at a value smaller in magnitude than the maximum theoretical value. These elastic effects are not included in the present modeling framework, and thus there is no such impediment to full ordering in the simulated alloy.

From Fig. 3.6 we conclude that the model developed here presents a qualitatively accurate description of the ordering transformation between 420 - 470 °C, however at lower temperatures the transformation may occur faster than predicted. Additional aging data is necessary to fully assess the model accuracy at the lower temperatures. At temperatures relevant to PWR conditions (about 330 °C), the model predictions in Fig. 3.6 indicate that while extensive ordering should not occur on the timescale of service lifetimes (40-80 years), the initiation of the ordering transformation will occur during this window.

3.3.7 Limitations of the first principles-based KJMA model

The model developed here has four main limitations. First, the effects of misfit strain between the ordered and disordered phases are not included. Any impact that this might have on the size or morphology of ordered domains in the real alloy will therefore not be manifested in the simulated alloy. This may contribute to the small overestimation of the maximum predicted change in lattice parameter with respect to most changes measured experimentally. Second, the KJMA model contains only a single kinetic term describing the ordering rate due to atomic migration. It is therefore only valid for conditions of sufficient undercooling that nucleation of

the ordered phase is homogeneous and transformation is rate-limited by atomic migration, and not nucleation rate, i.e., below the "nose" of the transformation diagram TEM characterization reveals that nucleation is homogenous at temperatures below 500 °C [71, 87]; above this temperature the assumptions of this model are not valid. Third, the model predictions are strongly dependent upon assumptions regarding the vacancy concentration. In this study we have estimated a value for this concentration based on GCMC simulations and the experimentally measured value of the vacancy concentration in pure Ni, and the uncertainty in the measured values in pure Ni alone amounts to more than 200 meV. This uncertainty corresponds to factors of 10 differences in the predicted ordering time. Furthermore, the model neglects the possible effects of excess vacancies that arise from water quenching or cold working. Finally, the simulation crystal is highly idealized with respect to the real material, and it contains no grain boundaries, dislocations, or other material defects. While these features can sometimes alter atomic migration mechanisms or provide nucleation sites for ordered domains, the experimental evidence of homogeneous nucleation suggests that the ideal, defect free crystal is a reasonable approximation of the real system, at least below 500 °C.

3.4 Key results and conclusions

In the study reviewed in this chapter, a first principles-based atomistic modeling framework has been developed for studying the disorder-order phase transformation in the Ni-33Cr model alloy. The alloy energetics are obtained via density functional theory calculations, which are used to construct a cluster expansion Hamiltonian. This Hamiltonian is then leveraged by grand canonical and kinetic Monte Carlo methods to simulate both the thermodynamic and kinetic aspects of the phase transformation. Based upon the results of these simulations, a

Kolmogorov-Johnson-Mehl-Avrami model was assembled that allows a direct comparison to experimental measurements of the change in lattice parameter in a Ni-33Cr model alloy arising from the disorder-order phase transformation. The model exhibits reasonable agreement with experimental data available in the literature below 500 °C, as well as new data generated in this study at 418 and 470 °C. Additional long-time, low-temperature data are desirable to assess the accuracy of the model at lower temperatures.

The predictions of the model developed in this study indicate that while complete transformation should not occur in the Ni-33Cr model alloy at operating temperatures during 40-80 year service lifetimes of PWRs, the early stages of the ordering transformation will occur on this timescale. There is some experimental evidence that even a small degree of ordering may have a significant impact on susceptibility to hydrogen embrittlement [85], and that the maximum embrittlement may occur well before the ordering transformation has completed [84]. Furthermore, experimental measurements at 373 °C indicate that the ordering transformation may occur even faster at low temperatures than predicted by the model developed here. Therefore, this result suggests that ordering cannot be readily dismissed as a long-term concern in near-stoichiometric Ni-Cr alloys in PWRs. However, many engineering alloys of interest are far from the Ni_2Cr stoichiometry and contain other alloying constituents such as Fe, which appears to delay the ordering transformation or prohibit it altogether [87, 88, 90]. Further study is therefore warranted on the effects of alloy composition on the order-disorder transformation kinetics, particularly near PWR operating temperatures where there is no experimental data available.

Chapter 4: Thermodynamic and kinetic modeling of oxide precipitation in nanostructured ferritic alloys

4.1 Introduction and background

The next generation of advanced nuclear energy systems are expected to place demands on structural materials that are beyond the capabilities of materials used in current designs. In particular, structural materials in proposed fusion and advanced fission reactor designs will be subject to significantly higher operating temperatures and larger radiation doses than in current generation light water reactors. To meet these demands, new classes of materials are required that can withstand radiation doses reaching hundreds of displacements per atom and operate at high temperatures for decades without losing mechanical integrity. Nanostructured ferritic alloys (NFAs), also referred to as oxide dispersion strengthened (ODS) steels, are one promising candidate for a class of materials that are able to meet these demanding requirements [1, 2, 122, 123].

NFAs are broadly similar in composition to other ferritic stainless steels, typically containing 12-16 wt% Cr and up to 0.5 wt% Mo or 3 wt% W [124], however they are differentiated by the additions of small amounts of Ti, Y, and O, which coalesce during processing to form a high density of nanometer scale T-Y-O nanoparticles throughout the ferrite matrix. The Y and nominally the O are most often introduced in the form of Y_2O_3 powder, which is mechanically alloyed with the ferritic steel powder via high energy ball milling [125]. The mechanically alloyed powder is then consolidated by hot isostatic pressing or extrusion to produce the NFA stock material.

The oxygen-rich nanoparticles confer a number of attractive properties to NFAs. Most significantly, they are highly effective in pinning dislocations [8], which grants these alloys high tensile strength at elevated temperatures [126] as well as excellent creep resistance [127, 128]. Furthermore, these nanoparticles constitute a high density of defect sinks, which inhibit the accumulation of radiation-produced point defects and suppress many types of long-term radiation damage [1]. There is also evidence that these nanoparticles are effective at trapping transmutant helium, thereby mitigating the helium-assisted void swelling and grain boundary embrittlement that can occur under irradiation, especially in fusion environments [2].

Because both the attractive mechanical properties and innate radiation damage resistance of NFAs are derived from the Y-Ti-O nanoparticles, the stability of these nanoparticles during component service is a critically important issue facing the adoption and implementation of NFAs for nuclear power applications. More specifically, a decline in the nanoparticle density caused by thermally-activated nanoparticle coarsening would have a dramatic impact on NFA mechanical properties [8, 124, 129]. Therefore, detailed knowledge of the kinetics of this coarsening process is crucial for establishing the time and temperature envelope within which NFAs are practically applicable. However, at proposed operating temperatures for NFAs measurable coarsening may take years or even decades to occur. It is therefore very challenging to assess the possible impact of nanoparticle coarsening kinetics from direct experimental measurement alone; some model-assisted extrapolation is critical.

A primary motivation for the research presented in this chapter is the need for such a model that can provide qualitative and quantitative insight into the rates and key mechanisms of nanoparticle coarsening that will limit NFA operating times and temperatures. Previous efforts

toward this goal have focused on empirical models fit to high temperature coarsening data [124, 129, 130]. This work has yielded crucial information, such as revealing the importance of dislocation or pipe diffusion in nanoprecipitate coarsening [124]. However, due to the empirical nature of these models, many physical properties and phenomena are combined into a small number of fitting parameters, which makes it difficult to tease out the important physical quantities that dominate the precipitation process in NFAs. The goal of the work described in this chapter was to develop a more physically-based model that incorporates known thermodynamic and kinetic material properties and one in which each fitting parameter is assigned to a single, well-defined quantity. Such a model is valuable for fundamental understanding of active mechanisms during NFA precipitate evolution, practical prediction of how Y-Ti-O composition and thermal history determine precipitate phases, sizes, and number density, and establishing a foundation for modeling other NFA alloy compositions and effects of irradiation. The construction of this model based upon DFT calculations, thermodynamic assessments, and rate theory-based precipitation modeling is the subject of this chapter.

This chapter is separated into two broad sections. The first section focuses on an *ab initio* study of the clustering energetics of Y, Ti, and O in Fe, with a goal of gaining fundamental insights into the nature of the smallest nanoprecipitates in NFAs. Building upon this fundamental guidance, the second section details the assembly of a model framework for describing the thermodynamic and kinetic aspects of oxide precipitation in NFAs.

4.2 First principles-based study of Y-Ti-O nanocluster energetics in NFAs

The overall goal of the work presented in this chapter was to develop a modeling framework for describing oxide precipitation in NFAs, however before such a model can be

assembled, the nature of these nanoprecipitates must be better understood. Due to the very small size of the Y-Ti-O nanoparticles in NFAs, some uncertainty remains regarding their typical structures and compositions. Many high resolution TEM images suggest that these nanoparticles are crystalline in nature with structures that are consistent with equilibrium Y, Ti and Y-Ti oxides [131-135], specifically Y_2O_3, TiO_2, $Y_2Ti_2O_7$, and Y_2TiO_5. Small angle neutron and x-ray scattering [124, 131, 136] and x-ray diffraction measurements [137, 138] are also consistent with this conclusion. Detailed atom probe tomography (APT) measurements have repeatedly indicated that the smallest Y-Ti-O nanoparticles in NFAs do not appear to be bulk-like oxide precipitates, and have compositions far from any known stoichiometric oxide phase [122, 131, 139-145]. However, it is likely that these atom probe measurements are affected by artifacts associated with the process of reconstructing the sample structure and may be misleading when it comes to determining precipitate stoichiometry [124].

Atomistic simulations based on DFT provide a powerful tool for investigation of the identity of the smallest nanoprecipitates in NFAs. DFT can be used to model small clusters of Ti, Y, and O of any configuration in a host Fe matrix and determine their formation energies, thereby revealing which types of small clusters are most stable and thus the most likely to initially form. Here we use the term clusters to describe the computational unit representing the initial stage of nanoprecipitate nucleation and growth. This approach has been utilized in several recent studies of solute clustering in NFAs: Fu *et al* [146] considered the effect of vacancies on the Fe lattice on the energetics of Ti, Y, and O clustering in bcc Fe, concluding that strong O-vacancy binding could play a crucial role in stabilizing Ti-Y-O nanoprecipitates with respect to oxide phases such as FeO and TiO_2. Jiang *et al* [147] demonstrated that stable Ti-Y-O clusters

could be formed in bcc Fe without appealing to vacancies, while recognizing the an O-O dumbbell structure sharing a lattice site is one key building block around which stable vacancy free clusters can be assembled. In a study focused on clustering behavior of Y and O in fcc Fe, Gopejenko *et al* [148] found that Y-Y interactions were uniformly repulsive, and both O atoms and vacancies were required to form stable on-lattice clusters. Murali *et al* [149] examined the possible effects of Cr on the clustering behavior of Ti, Y, and O in bcc Fe, as well as the potential for creating more stable clusters by replacing Ti with Zr. As the authors of Refs. [146, 148] reported, Murali *et al* [149] found that, if present, vacancies are an important component for creating stable clusters at very small sizes, and that Y-vacancy binding is particularly strong as is O-vacancy binding.

While DFT calculations are generally computationally limited to clusters that are far smaller than the nanoprecipitates found in NFAs, it is evident that they can nevertheless lend valuable information about the energetics and clustering tendencies of Ti, Y, and O in Fe during the earliest stage of precipitation in NFAs. However, as the number of different clusters of Ti, Y, and O that can be assembled is combinatorial, one is faced with the question of which clusters to investigate. In the aforementioned studies, clusters were assembled using a so-called "on-lattice" method, which means that solute metal atoms are placed exclusively on Fe substitutional sites and O atoms on Fe octahedral interstitial sites. This is an intuitive method for searching for stable nanoclusters: as isolated species, the solute M and O atoms exist as substitutional or octahedral interstitial impurities, respectively, so it is not unreasonable to expect that they occupy these sites during the earliest stages of clustering. Furthermore, on-lattice clusters are fully coherent with the Fe matrix, which should tend to minimize interfacial energy when

compared to incoherent clusters. For very small clusters, the interface can contribute a large portion of the total energy, and its minimization can therefore play a dominant role in particle structure, composition, and morphology. Finally, as mentioned previously, some interpretations of APT results suggest that the smallest nanoprecipitates in NFAs are clusters enriched in the solutes Ti, Y, and O that may be coherent with the Fe lattice [1, 2]. Notably, however, recent TEM studies are not consistent with this conclusion [150].

In this study, we have assembled a large suite of Ti, Y, and O clusters and we calculate their formation energies via DFT. In addition to the on-lattice cluster assembly method utilized in the studies described above, we employ a new cluster assembly method by which clusters are matched to bulk oxide structures of Ti and Y, and then embedded in Fe in a manner that minimizes strain in the Fe and oxide. We will refer to this approach for identifying clusters as the "structure matching" method. Furthermore in this study we investigate a much wider range of cluster sizes than have been investigated previously, in order to identify trends of cluster morphology and stability with size. Because of the large number of possible arrangements of the atoms in nanoclusters containing Ti, Y, and O, a full exploration of the Ti-Y-O compositional space is currently not feasible using the methods presented in this paper. We therefore focus primarily on the Ti-O and Y-O clusters, and perform a smaller set of calculations on Ti-Y-O clusters at a fixed Y:Ti ratio of 1:1. This ratio was chosen to match that of the complex Y-Ti oxide $Y_2Ti_2O_7$. While other complex oxides such as Y_2TiO_5 have been observed in NFAs as well, the smallest nanoprecipitates observed by TEM are predominantly $Y_2Ti_2O_7$ [150]. It is important to emphasize that the DFT calculations are meant to illustrate trends and what are perhaps qualitative differences between potential decomposition paths. Due various limitations

of this, and essentially all other similar practical approaches, the quantitative results should be viewed with caution.

4.2.1 Cluster assembly and computational method

In this section, we first describe our methods for constructing Ti-O and Y-O clusters using specific examples to illustrate the details of the methodology. We then describe our formalism for calculating cluster formation energies and we provide details of the computational techniques.

In order to study nanoprecipitate stability in NFAs, we must first decide which clusters to test. To this end, we have employed two distinct methods for assembling Ti-O and Y-O clusters in bcc Fe. The first method, which we refer to as the "on-lattice" method, is the same as used in all previous DFT studies of nanocluster formation [146-149]. In this approach, clusters are assembled by placing Ti or Y atoms on the Fe substitutional sites and O atoms on the Fe octahedral interstitial sites, as depicted schematically in Fig. 4.1.

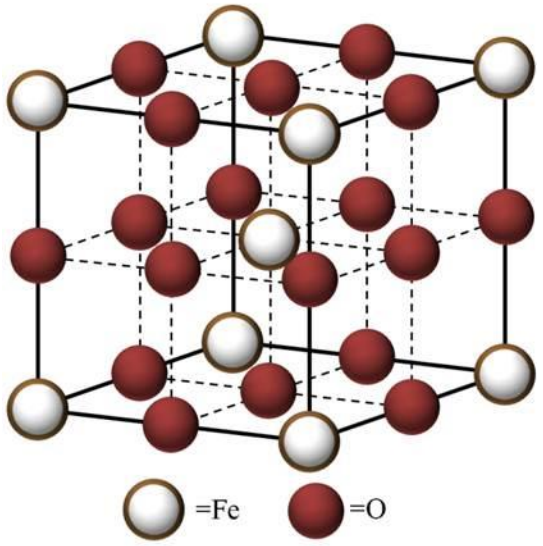

Figure 4.1: bcc scell illustrating the on-lattice cluster method. Red circles represent an interstitial lattice of sites available for O atoms, white circles represent bcc lattice sites available for Fe, Ti, or Y atoms.

These clusters are perfectly coherent with the host Fe lattice. The second method, which is referred to as the "structure matching" method, involves creating clusters of Ti-O and Y-O that mimic the structure of Ti and Y oxides, and then embedding them in the Fe matrix with as little distortion to the Fe or the oxide structure as possible. In this construction the Ti or Y atoms do not have to occupy the Fe lattice sites and any Fe atoms that impinge too closely upon the cluster are removed. This approach results in strained clusters that are volume matched with a strained host ferrite matrix. Since the oxides are less densely packed than the on-lattice clusters, volume matching with minimum strains also requires the removal of some net number of Fe atoms. For illustrative purposes, this process is depicted schematically for an arbitrary two-dimensional metal oxide in Fig. 4.2.

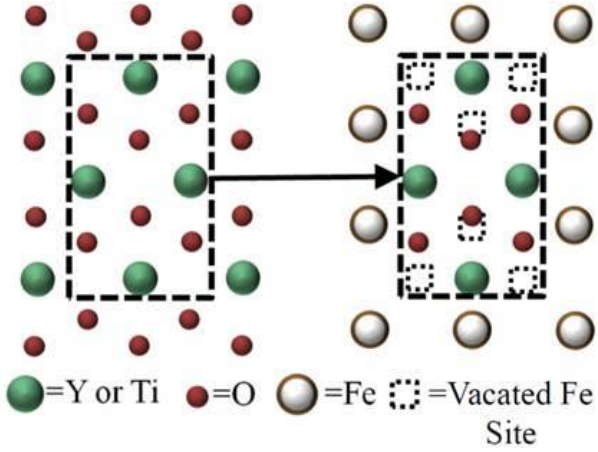

Figure 4.2: A two dimensional depiction of the structure matching method of cluster assembly.

The specific structure-matched clusters for the Ti-O and Y-O systems are discussed in subsequent paragraphs.

For the Ti-O system, we chose to match clusters to rutile TiO_2. While Ti forms a large number of stable oxides, rutile TiO_2 is the equilibrium phase in O-rich environments and is thus a reasonable selection [151-153]. In this structure, the Ti atoms occupy a bct structure with lattice parameters a = 0.459 nm and c = 0.296 nm [154], and each Ti atom is coordinated by 6 O atoms. In creating a Ti-O cluster in bcc Fe that matches this structure, it is simplest to imagine laying the (100) plane of the TiO_2 structure on top of the (110) plane of the bcc Fe crystal, such that the [010] and [001] directions of the TiO_2 structure are oriented along the [110] and [001] directions of the Fe crystal, respectively. This is sufficient to fully define the orientation relationship of the oxide and Fe lattices. To construct a structure-matched Ti-O cluster containing 6 Ti atoms, the 4 Fe atoms at the corners of the rectangle described by this plane are replaced by Ti atoms, and 2 additional Ti atoms are placed at the edge centers at positions (0,0,1/2) and (1,1,1/2) in the bcc Fe cell. The O atoms are then placed in appropriate positions

with respect to the Ti atoms, according to the rutile TiO_2 structure. The cluster constructed this way is depicted schematically in Fig. 4.3.

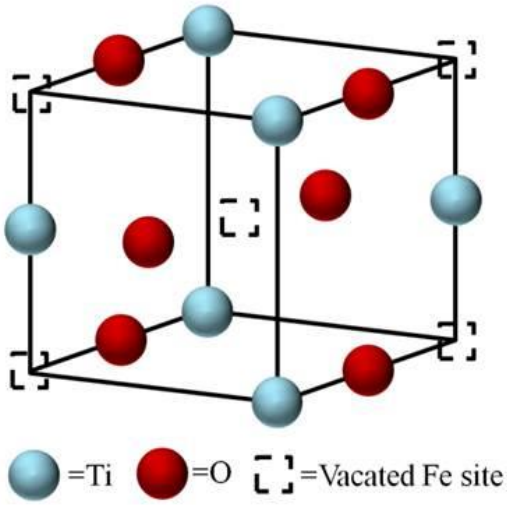

Figure 4.3: Structure-matched Ti-O cluster comprised of 6 Ti atoms and 6 O atoms arranged on a single bcc Fe unit cell

In Fig. 4.4, a structure-matched Ti-O cluster containing 6 Ti atoms and 6 O atoms after full relaxation is depicted along with the corresponding structure in bulk rutile TiO_2.

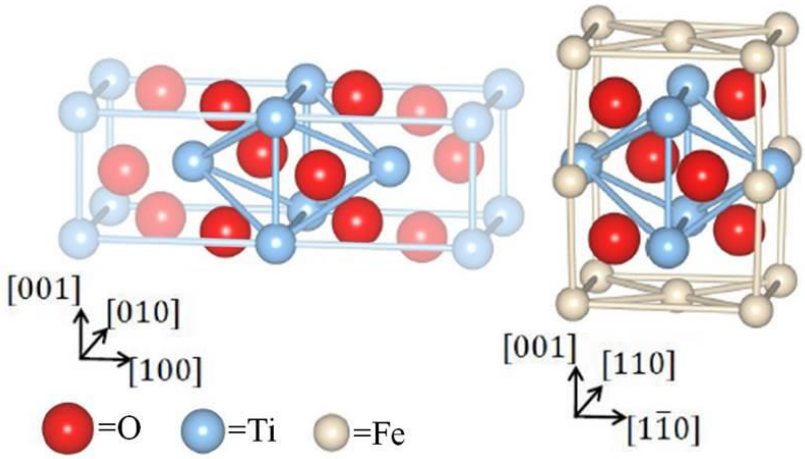

Figure 4.4: A 6Ti-6O stucture matched cluster as it appears in rutile TiO_2 (left) and embedded in Fe after full ionic relaxation (right). The Ti and O atoms in the cluster are highlighted for emphasis

For the Y-O system, we use the bixbyite phase of Y_2O_3 to generate structure-matched clusters. This structure may be described as a defected fluorite structure with ordered vacancies on the O sublattice. To account for the ordering of the O sublattice vacancies, the complete unit cell is quite large, with a lattice parameter 1.06 nm [155] and consisting of a 2×2×2 supercell of the Y fcc sublattice. For the purposes of generating structure-matched clusters, we build one eighth of the full bixbyite unit cell, which consists of a single fcc Y cell of length 0.53 nm and which contains 6 O atoms. When creating a Y-O cluster in bcc Fe that matches this structure, it is simplest to imagine that this fcc Y cell corresponds to a 2×2×2 bcc supercell of Fe with an edge length of twice the lattice parameter of Fe, or about 0.56 nm. If the Fe atoms residing on the corners and face centers of this supercell are replaced with Y atoms, and the Fe atoms on the edge centers and in the interior of the supercell are removed, the result is an fcc Y cell similar in size and shape to the fcc Y sublattice in bixbyite Y_2O_3. Thus, the lattice vectors of the cubic bcc Fe crystal and the cubic Y_2O_3 oxide crystal are parallel. To generate a structure-matched Y-O cluster consisting of 6Y and 6O, we replace the face centers of the aforementioned 2×2×2 bcc Fe supercell with Y atoms, resulting in a Y octahedron. The Fe atoms interior to this octahedron are removed, and O atoms inserted in appropriate positions with respect to the Y atoms. The cluster constructed this way is depicted schematically in Fig. 4.5.

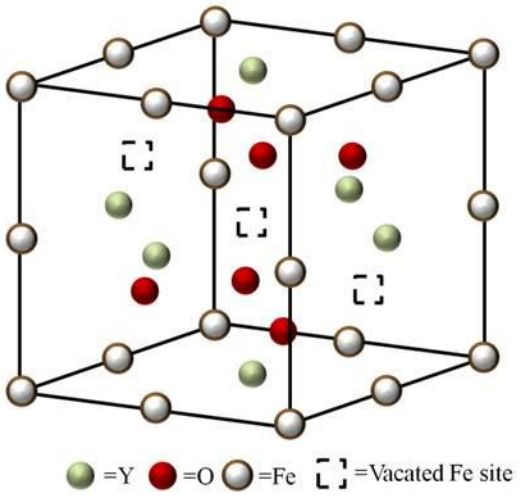

Figure 4.5: 6Y-6O structure-matched cluster configured on a 2x2x2 bcc Fe supercell

In Figure 4.6, this cluster is depicted after a full relaxation, along with the corresponding structure in bixbyite Y_2O_3.

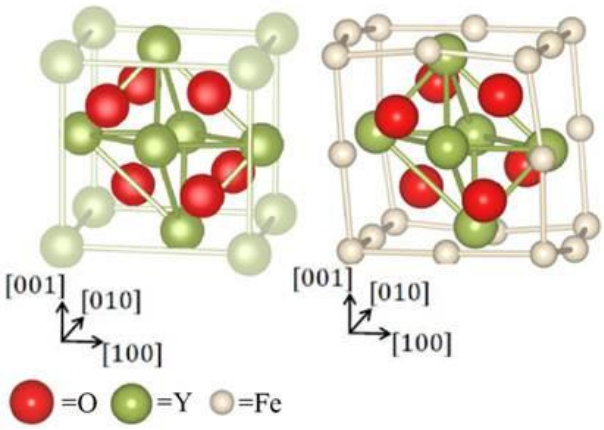

Figure 4.6: A 6Y-6O structure-matched cluster as it appears in bixbyite Y_2O_3 (left) and embedded in Fe after full ionic relaxation (right). The Y in the cluster are highlighted for emphasis.

Using the cluster assembly methods described above, we prepared a large set of Ti-O and Y-O clusters ranging in size from 3 to 30 atoms. We then categorized the clusters based upon the total number of Ti or Y atoms that they contain, with the intention of addressing the following question: given a fixed number of Ti or Y atoms, but allowing any number of O

atoms, what type of cluster configuration is most stable? Our focus on a system of fixed number of metal atoms but variable oxygen is motivated by the relative diffusivities of Ti, Y, and O in Fe, listed in Table 4.1 [156, 157].

Table 4.1: Diffusion coefficients of Fe, Y, Ti, and O in Fe at 1150 ^{o}C.

Species	Diffusion Coefficient (m^2/sec)
Fe	1.1×10^{-20}
Y	1.5×10^{-23}
Ti	1.7×10^{-20}
O	1.0×10^{-14}

Because O is able to diffuse many orders of magnitude faster than either Ti or Y, we make use of the standard assumption of local equilibrium, since compared to the time that it takes for individual Ti or Y atoms to come together and form a cluster, equilibration with the local O environment will be nearly instantaneous, and O-equilibrium is continuous as the precipitate grows. In other words, as a cluster grows one Ti or Y atom at a time, it has access to all the O atoms it requires to form its most stable configuration at any given moment.

The structure-matched clusters were further categorized based on their O content. Because the structure-matched clusters are constrained to the structure of a bulk oxide, the only way such a cluster can exhibit an overall O fraction that differs from the oxide stoichiometry is through the effect of surface termination: clusters that are O terminated will tend to be O-rich, or hyper-stoichiometric, while clusters that are Ti or Y terminated will tend to be O-poor, or hypo-stoichiometric. Thus, O content for the structure-matched clusters is determined by the choice of cluster surface termination. To obtain a reasonable sample of this range of O content, for each given cluster size category we constructed three different structure-matched clusters. All three have the same number of Ti or Y atoms in the same configuration, and differ only in O

content: one cluster is Ti or Y terminated (hypo-stoichiometric), one is of mixed termination (stoichiometric), and one is fully O terminated (hyper-stoichiometric).

Both the hypo-stoichiometric and hyper-stoichiometric conditions generally define a unique structure. The hypo-stoichiometric clusters contain only the O atoms that are closest to the interior of the cluster. Examples of this structure are shown in Figs. 4.4 and 4.6, which depict hypo-stoichiometric structure-matched clusters of 6 Ti and 6 Y atoms, respectively. Each cluster contains 6 O atoms that lie on the shell that is closest to the center of the cluster, and adding any additional O atoms would require placing them much further from the center of the cluster. In the hyper-stoichiometric clusters, each metal atom has the same O coordination that it would have in the bulk oxide phase, both in terms of the number of O nearest neighbors and their geometrical arrangement. This constraint defines both the number and positions of all the O atoms in the cluster. In contrast, the stoichiometric condition generally does not define a unique structure and there are many potential sites for the outer most O atoms in the cluster. When constructing the stoichiometric clusters, we first fill the inner most O shell as in the hypo-stoichiometric case and then place additional O atoms in the next available shell in such a way that they are as far apart as possible.

To calculate the formation energy of a given cluster, we use the following expression:

$$\Delta E_f = E(n_{Fe}, n_M, n_O) - (n_{Fe}\mu_{Fe} + n_M\mu_M + n_O\mu_O) \quad (4.1)$$

where $E(n_{Fe}, n_M, n_O)$ is the energy of a supercell containing n_{Fe} Fe atoms and a cluster containing n_M M atoms (where M = Ti or Y) and n_O O atoms and μ_i is the energy per atom of species *i* in its reference state. The reference state of Fe is pure Fe, the reference states for Ti and

Y are isolated substitutional Ti or Y atoms in otherwise pure Fe, and the reference state for O is an isolated octahedral interstitial O atom in otherwise pure Fe.

All DFT calculations were performed using VASP [62-65]. Computation details and parameters were selected based upon the methods developed by Jiang *et al* in a similar study [147]. These parameters are summarized in Table 4.2.

Table 4.2: Pertinent computational settings and details.

Supercell Size	4x4x4 bcc Fe supercell
Plane-wave cutoff energy	400 eV
k-point mesh	2x2x2 Monkhorst-Pack scheme
Pseudopotentials	PAW-GGA

While the results in Ref. [147] indicate that these settings (e.g., the supercell consisting of 128 Fe atoms) are sufficient for a small number of solute atoms, some of the clusters considered in this study are significantly larger than those in Ref. [147] and therefore our calculations may suffer from finite size effects. To estimate the magnitude of these effects, we recalculated the formation energy of a structure-matched Y-O cluster from the largest cluster size category containing 6 Y and 9 O atoms using a supercell nominally containing 250 Fe atoms (instead of 128 Fe atoms). The formation energy difference when using a nominal 250 Fe atom supercell compared to a 128 atom supercell was negative 0.346 eV per metal atom in the cluster. This compares with nominal values of between negative 0.66 and 1.33 eV per metal atom. Thus, the qualitative conclusions are likely to be independent of their system size.

4.2.2 Identity of the Most Stable Ti-O and Y-O Nanoclusters in Fe

In order to investigate the stability of Ti-O and Y-O nanoclusters in Fe, we have assembled large sets of clusters according to the two construction methods described in Sec. 4.2.1 and we calculated their formation energies. The nanoclusters considered here range in size

from 3 to 30 atoms, and the largest clusters have a diameter of about 0.6 nm. In Fig. 4.7 we plot formation energy of the Ti-O and Y-O clusters as a function of the cluster size.

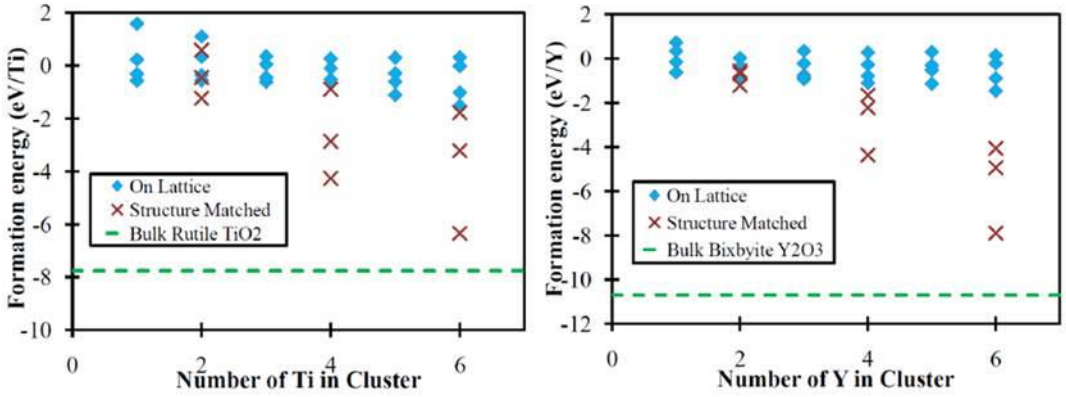

Figure 4.7: Cluster formation energies as a function of cluster size for Ti-O clusters (left) and Y-O clusters (right).

Across all cluster sizes, for both the Ti-O and Y-O systems, it is evident that the structure-matched clusters are more stable than the on-lattice clusters. This trend becomes significantly stronger as the cluster size increases, which suggests that for clusters larger than those studied here, the difference in formation energies between on-lattice type clusters and lattice matched clusters will be even greater. We thus conclude that clusters of Ti or Y with O that resemble bulk oxide structures are significantly more stable than on-lattice type clusters that are fully coherent with the Fe lattice. We note that the formation energy difference between the largest structure-matched clusters and on-lattice clusters is on the scale of several eV, which is considerably larger than our estimate for errors due to finite supercell size, and therefore the presented conclusions are qualitatively robust.

Among the structure-matched clusters represented in Fig. 4.7, those that are hyper-stoichiometric are most stable while those that are hypo-stoichiometric are the least stable, irrespectively of the cluster size. As discussed in Sec. 4.2.1, the apparent off-stoichiometry of

these clusters is due to surface termination, which has a significant impact on the stoichiometry of very small clusters, and is not an indication that the most stable structures are M-O clusters of different stoichiometry than known oxide phases, as has been suggested in previous studies [1, 131].

4.2.3 Stability of Ti-Y-O clusters with Y:Ti ratio of 1:1

In Sec. 4.2.2 we focused on the binary Ti-O and Y-O clusters, which calculations provided a foundation for understanding of the Ti-Y-O nanocluster system. In this section, we extend the approach described in Sec. 4.2.1 to clusters containing Y, Ti, and O. For the structure-matched clusters we match to the structure of $Y_2Ti_2O_7$ pyrochlore that is observed at the smallest nanoprecipitate sizes [150]. The structure of this oxide is very similar to the structure of bixbyite Y_2O_3 in that they may both be considered defected fluorite structures with ordered vacancies on the O sublattice [158]. The structure-matched Ti-Y-O clusters are therefore very similar to the structure-matched Y-O clusters, as discussed in Sec 4.2.2. A fully relaxed structure-matched Ti-Y-O cluster and the corresponding structure in bulk $Y_2Ti_2O_7$ pyrochlore are depicted in Fig. 4.8.

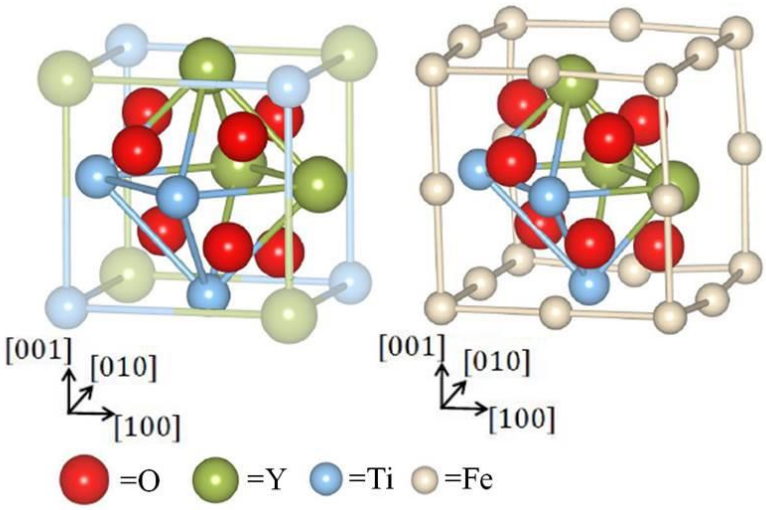

Figure 4.8: A 3Y-3Ti-6O structure-matched cluster as it appears in pyrochlore $Y_2Ti_2O_7$ (left) and embedded in Fe after full ionic relaxation (right). The Y, Ti, and O in the cluster are highlighted for emphasis

As with the Ti-O and Y-O cluster sets of Sec. 4.2.2, we assembled three structure-matched clusters for the 4 and 6 M atom cluster size categories, differing in their O terminations. The "stoichiometric" structure-matched Ti-Y-O cluster of 6 atoms is slightly sub-stoichiometric, as it is not possible to create a cluster containing 3 Ti and 3 Y atoms with the stoichiometry of $Y_2Ti_2O_7$. To be consistent with the composition of the structure-matched clusters, we constrain the Y:Ti ratio to 1:1 for all Ti-Y-O on-lattice clusters. A more full exploration of the Y-Ti compositional space is desirable but is beyond the scope of the present work.

In Fig. 4.9, cluster formation energies are plotted as a function of cluster size.

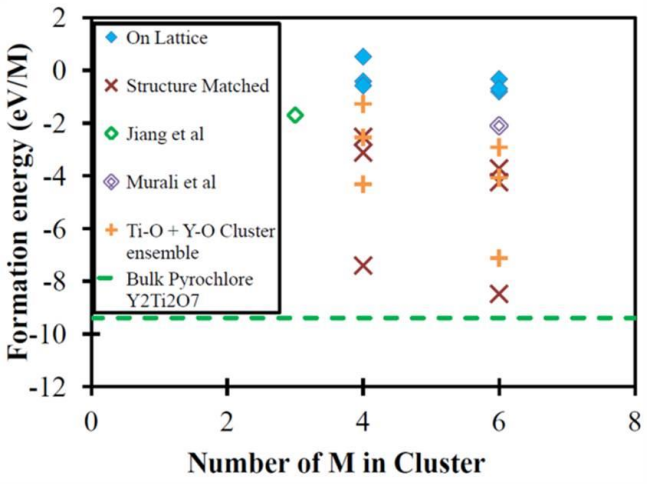

Figure 4.9: Cluster formation energies as a function of cluster size for Ti-Y-O clusters

The series "Ti-O + Y-O Cluster Ensemble" depicts the formation energies per metal atom for ensembles of Ti-O and Y-O structure-matched clusters of a given cluster size, where the overall Ti:Y ratio for the ensemble is 1:1. For both the 4 and 6 metal atom clusters, the Ti-Y-O structure-matched cluster series is lower in energy per M atom than the corresponding Ti-O/Y-O cluster ensemble, indicating that even for these very small cluster sizes there is a strong driving force for the reaction $2TiO_2 + Y_2O_3 \Rightarrow Y_2Ti_2O_7$.

Formation energies of two on-lattice clusters reported in earlier calculations [147, 149] are also included in Fig 4.9 for comparison. Clusters from Refs. [147, 149] show a greater stability than the on-lattice clusters investigated in the present study. In the case of Ref [149] this may be due to inclusion of locally stabilizing vacancies. The lowest energy cluster assembled in Ref [147] is stabilized by the inclusion of a [100] O-O interstitial dumbbell configuration that was found to be highly stable with respect to the single O octahedral interstitial. As this configuration requires that the O be permitted to reside on the Fe substitutional lattice, it is not permitted according to the on-lattice cluster assembly method

utilized in the present study. Nevertheless, the Ti-Y-O nanoprecipitates that are matched to the bulk oxide structure are far more stable than the on-lattice clusters assembled in this study and those from Refs [147, 149]. Evidently, the structure matching method results in clusters that are more stable than those assembled by any of the previously reported on-lattice methods. We therefore argue that the energetically most favorable nanoprecipitate nuclei formed in Ti-Y-O NFAs are fully consistent with stoichiometric oxide particles that are a partially relaxed precursor to a semicoherent structure orientation relationship with the Fe lattice, as opposed to clusters of Ti, Y, and O that are fully coherent with the Fe lattice. This result does not necessarily contradict the conclusion that structural vacancies will further increase the stability of equilibrium Ti-Y-O nanoclusters [146, 148, 149]. However, when the cluster is not restricted to the Fe lattice, vacancies in the cluster become difficult to define as a discrete species. Consequently it seems more accurate to conclude that some amount of vacant space in the Fe lattice is necessary to form the most stable Ti-Y-O nanoclusters, and that this space is provided by a corresponding aggregation of Fe vacancies.

4.2.4 Primary results and implications for Y-Ti-O nanocluster behavior

In the study presented in this section, we performed DFT calculations to identify possible candidate structures for the smallest nanoprecipitates in Ti-Y-O NFAs. In our search for potential structures, we utilized two cluster assembly methods: one which restricted the Ti or Y atoms to the Fe substitutional lattice sites and O to Fe octahedral interstitial sites, and one which matches the Y, Ti, and O to the structure of a known stable oxide phase. For the Ti-O and Y-O subsystems, we assembled large sets of clusters ranging in size from 3 to 30 atoms. It was determined that at all sizes, the clusters that match bulk oxide phases are more stable than the

clusters that are fully coherent with the Fe lattice. Based upon these findings, we assembled a smaller set clusters containing Ti, Y, and O to determine whether this trend also holds in the full Ti-Y-O system. Our results indicate that clusters which are matched to the structure of pyrochlore $Y_2Ti_2O_7$ are more stable than clusters that are restricted to the Fe lattice. This result is consistent with TEM observations of $Y_2Ti_2O_7$ oxides down the sizes of 1 nm [134, 150, 159]. This results is true not only among the set of clusters tested here, but among the broader set of M-O clusters of similar size tested in previous DFT studies of nanocluster formation in NFAs [147, 149]. We therefore believe that the most energetically favorable nanocluster nuclei in Ti-Y-O NFAs are likely to resemble complex Ti-Y oxides that are at least partially incoherent with the Fe lattice.

4.3 Thermodynamic and kinetic modeling framework for studying oxide precipitation in NFAs

The primary objective of the model described in this section was to understand and predict coarsening behavior of nanoprecipitates in NFAs during very long service lifetimes at temperatures relevant to nuclear reactor operating conditions. Additionally, the model was used to further elucidate the coarsening mechanisms identified by previous empirical modeling [124, 129, 130]. Finally, the possible effect of Y and Ti alloy content on precipitate size distribution was examined, in order to provide guidance for alloy design.

Based upon the DFT calculations reviewed in Sec. 4.2, and upon numerous experimental observations [124, 131, 135-137], the model developed in this section is based upon the assumption that the nanoprecipitates are known equilibrium Y-Ti oxide phases during their entire evolution. While this approximation will not capture potentially important details such as the precise nucleation pathway through compositional space or the appearance of metastable phases,

it is a well-defined limit that can be used as a platform to begin to understand the complex multicomponent precipitation process in NFAs.

This section is organized as follows: Sections 4.3.1-6 first detail the thermodynamic model used to evaluate the necessary driving forces for modeling nanoparticle precipitation in NFAs. The kinetic model for simulating the nanoparticle precipitation is then described in detail. Sections 4.3.7-10 present the predictions of the thermodynamic model and the results of fitting the kinetic model to experimental measurements of nanoparticle size as a function of time during aging. The predictions of the best-fit model regarding coarsening kinetics and alloy composition effects on nanoparticle size are then presented. Finally, Sec. 4.4 provides concluding remarks and commentary on pathways toward more advanced models.

4.3.1 Thermodynamic Model

The model developed in this study describes nanoparticle precipitation in NFAs fundamentally as the phase separation of Y and Ti oxide phases from a bcc Fe-Cr-Y-Ti solid solution. The thermodynamic model used to describe the driving forces for this phase separation includes the following phases: bixbyite Y_2O_3, rutile TiO_2, pyrochlore $Y_2Ti_2O_7$, orthorhombic Y_2TiO_5, and ferrite Fe-Cr-Y-Ti solid solution. The oxide phases are the equilibrium phases that appear on the Y_2O_3 – TiO_2 pseudobinary phase diagram [160] over the temperature range of interest (900 K – 1573 K), while ferrite is the predominant matrix phase in most NFAs [1, 125].

Within this thermodynamic model, the equilibrium phase separated state of a given NFA can be determined by first computing the free energies of the phases listed above and then minimizing the free energy of the total system with respect to the fractions of each phase. Numerous thermodynamic assessments in the CALPHAD formalism were used to describe the

free energies of these phases. The necessary parameters for these descriptions are summarized in Table 4.3.

Table 4.3: CALPHAD parameters used in the thermodynamic and kinetic models. All parameters have units J/mol.

Model	Expression	Source
Y_2O_3 (bixbyite)	$G^{203} = -1976462 + 731.6512T - 121.881T\ln T - 0.00506T^2 + 1090000T^{-1} - 13000000T^{-2} - \frac{3}{2}G^{gas}_{O_2}(T, P_{O_2})$	[161]
TiO_2 (rutile)	$G^{012} = -976986.6 + 484.74037T - 77.76175T\ln T + 1683920T^{-1} - 67156800T^{-2} - G^{gas}_{O_2}(T, P_{O_2})$	[151]
$Y_2Ti_2O_7$ (pyrochlore)	$G^{227} = G^{203} + 2G^{012} - 65569.9 - 37.19T$	[160]
Y_2TiO_5 (orthorhombic)	$G^{215} = G^{203} + G^{012} - 31976.9 - 21.3T$	[160]
Y (α)	${}^0G^{\alpha}_{Y} = -1297.798 + 134.528352T - 27.3038477T\ln T - 0.541758\times10^{-3}T^2 - 0.305012\times10^{-6}T^3$	[162]
Ti (α)	${}^0G^{\alpha}_{Ti} = 6667.385 + 105.366379T - 22.3771T\ln T + 1.21707\times10^{-3}T^2 - 0.84534\times10^{-6}T^3 - 2002750T^{-1}$	[162]
O_2 (gas)	$\frac{1}{2}G^{gas}_{O_2} = \mu_O - 6568.763 + 12.659879T - 16.8138T\ln T - 0.595797\times10^{-3}T^2 + 0.006781\times10^{-6}T^3 + 4383200T^{-1} + RT\ln P_{O_2}$	[162]
Solid Solution (α)	${}^{(0)}L^{\alpha}_{FeY} = 100000$ ${}^{(0)}L^{\alpha}_{CrY} = 300000$ ${}^{(1)}L^{\alpha}_{CrY} = 230000$ ${}^{(0)}L^{\alpha}_{FeTi} = -69241.924 + 25.246T + 0.0001T^2 + 120000T^{-1}$ ${}^{(1)}L^{\alpha}_{FeTi} = 5018.986 - 4.992T$ ${}^{(2)}L^{\alpha}_{FeTi} = 23023.241 - 13.110T$ ${}^{(0)}L^{\alpha}_{CrTi} = -2247.87 + 9.14144T$ ${}^{(1)}L^{\alpha}_{CrTi} = 198.73$	[163-166]

The total free energy to be minimized may be written as

$$G^{tot} = f^{\alpha}G^{\alpha} + f^{203}G^{203} + f^{227}G^{227} + f^{215}G^{215} + f^{012}G^{012} \quad (4.2)$$

where $f^i G^i$ is the product of the mole fraction of phase *i* and the molar free energy of phase *i*. The superscripts 203, 227, 215, and 012 refer to the oxide phases Y_2O_3, $Y_2Ti_2O_7$, Y_2TiO_5, and TiO_2 respectively. The free energy of the solid solution phase is computed using the following equation:

$$G^{\alpha} = \sum_i x_i {}^0G_i^{\alpha} + RT \sum_i x_i \ln x_i + {}^{ex}G^{\alpha} \tag{4.3}$$

where x_i is the mole fraction of component *i* in the ferrite phase α (*i* = Y or Ti), and ${}^0G_i^{\alpha}$ is the molar free energy of pure component *i* in the structure of α. The term ${}^{ex}G^{\alpha}$ is the excess free energy of mixing, described by the Redlich-Kister polynomial

$$^{ex}G^{a} = x_m x_n \sum_j (x_m - x_n)^j \left({}^{(j)}L_{mn}^{a} \right) \tag{4.4}$$

where *m* = Fe, Cr and *n* = Y, Ti. The parameters ${}^{(j)}L_{mn}^{\alpha}$ are defined in Table 4.3. Because the mole fractions of Ti and Y in NFAs are generally dilute (typically less than 1 at%), Y-Y, Y-Ti, and Ti-Ti interactions in the solid solution phase are also neglected. Furthermore, because the mole fractions of Fe and Cr in solution do not change during the precipitation of the Y and Ti oxide phases, the contributions to the total free energy of the free energies of pure Fe and Cr, the Fe and Cr entropies of mixing, and the Fe-Cr interactions in the excess free energy of mixing are approximately the same before and after the phase separation. They are therefore neglected when minimizing the free energy with respect to the mole fractions of the oxide phases. Finally, interactions involving O in the solid solution phase are neglected because it is assumed that O exists in the alloy at a constant chemical potential throughout the phase separation. This assumption is further discussed below.

When determining the equilibrium oxide phase separation in a given NFA, Eqn. 4.2 is minimized under the constraints of constant mole numbers of Fe, Cr, Y, and Ti, and constant chemical potential of O. These constraints are equivalent to assuming that the system is closed with respect to Fe, Cr, Y, and Ti but open with respect to O. The assumption of openness with respect to O is based upon two general observations. First, the O content typically measured in NFAs generally far exceed the amount of O nominally added to the alloy in the form of the Y_2O_3 powder [124, 137, 140, 167-170]. In fact, Auger et al. [170] compared Fe-14Cr model alloys manufactured both with and without the additions of Y_2O_3 powder and found that both variants contained similar O content, with the Y_2O_3 addition imparting only a relatively small amount of additional O. This suggests the majority of the O in the alloy enters the system during processing, presumably during the milling and subsequent heat treatment. Second, Cr and Fe oxides are often observed on the surface of NFAs [124, 140, 171] or the bulk [145, 168, 170], suggesting an equilibrium of the NFA precipitates with these oxides may be occurring. Furthermore, the internal oxidation of Y has been shown to reduce the amount of surface oxide growth in Fe [172], Ni-Cr alloys [173], as well as NFAs [171], indicating that the formation of surface oxides and the internal precipitation of Y oxide particles are coupled processes. Because the diffusion coefficient of O in the ferrite phase is many orders of magnitude higher than the diffusion coefficients of any of the metal species in the alloy [174-176], we assume that the O in the matrix can diffuse sufficiently fast that it can equilibrate with the plentiful Cr and Fe oxide phases on the surface or within the material on the timescale of the Y-Ti oxide nanoparticle precipitation. With these observations and assumptions, it is reasonable to assume that the surface oxide acts as a reservoir for O that maintains an O concentration in the matrix at a fixed

chemical potential. The exact value of this chemical potential is unknown, however in this study the chemical potentials corresponding to equilibrium with known Fe and Cr oxides have been used to provide a plausible range for this parameter.

4.3.2 Kinetic model: basic formalism and equations

The model used in this study to describe the kinetics of Y-Ti oxide precipitation is based upon Slezov's general theory of the kinetics of first order phase transformations. The main resulting expressions of this theory will be will be discussed in subsection 2.2.1; a thorough derivation of these expressions may be found in [177] and in chapter 2 of [178].

In the kinetic theory of Slezov, the ensemble of precipitates of a given phase in the system is described by the size distribution function $f^{\phi}(n,t)$, which specifies the concentration of precipitates or clusters of phase ϕ containing *n* constituent structural units at time *t*. In the present model we assume that the O atoms diffuse at a much higher rate than the metal atoms, and consequently the growth of the oxide precipitates is controlled kinetically by the aggregation of Y and Ti monomers. Therefore, for the purposes of describing the growth kinetics, the constituent structural units are taken to be integer numbers of Y and Ti atoms in proportions that match the Y:Ti ratios of the four oxide phases considered for precipitation. Specifically, these are

$$\begin{aligned} n^{203} &= 1Y \\ n^{227} &= 1Y + 1Ti \\ n^{215} &= 2Y + 1Ti \\ n^{012} &= 1Ti \end{aligned} \tag{4.5}$$

O is not included as a part of the constituent structural units because it is assumed that O arrives at the cluster nearly instantaneously on the timescale of Y and Ti diffusion, so the kinetics of O diffusion is not included explicitly in the model equations. The expressions for the volume and the free energy per structural unit of the oxide phases are defined assuming O joins the oxide precipitates in the correct stoichiometric proportions instantaneously from the background reservoir of O.

The evolution of the function $f^{\phi}(n,t)$ for each oxide phase ϕ is described by the following partial differential equation:

$$\frac{\partial f^{\phi}(n,t)}{\partial t} = -\frac{\partial J^{\phi}(n,t)}{\partial n} \tag{4.6}$$

where $J^{\phi}(n,t)$ is the flux in cluster size space. Because $f^{\phi}(n,t)$ is discrete in cluster size *n*, in practice Eqn. 4.6 may be recast as *n* ordinary differential equations:

$$\frac{df_n^{\phi}(t)}{dt} = J_{n-1}^{\phi} - J_n^{\phi} \tag{4.7}$$

where $f_n^{\phi}(t)$ is the concentration of clusters of phase ϕ and size *n* and J_n^{ϕ} is the flux of clusters of phase ϕ between sizes *n* and *n* + 1. These fluxes are expressed as

$$J_n^{\phi} = w_n^{\phi}\left\{ f_n^{\phi}(t) - f_{n+1}^{\phi}(t)\exp\left[\frac{\Delta G^{\phi}(n+1) - \Delta G^{\phi}(n)}{RT}\right]\right\} \tag{4.8}$$

The term w_n^{ϕ} is the rate at which a cluster of size *n* incorporates a constituent structural unit from the matrix phase and grows to size *n* + 1. Under the assumptions that the clusters are

spherical and grow via three dimensional monomer diffusion from the matrix phase to the surface of the cluster, the rates w_n^ϕ can be written as

$$w_n^\phi = 4\pi \frac{a^\phi}{\omega^\alpha} D_{eff}^\phi n^{1/3} \tag{4.9}$$

where a^ϕ is the characteristic length of a constituent structural unit in phase ϕ (α here designates the ferrite matrix phase). This parameter equal to the radius of a sphere with volume equal to the volume per structural unit of phase ω^ϕ:

$$a^\phi = \left[\frac{3\omega^\phi}{4\pi} \right]^{1/3} \tag{4.10}$$

D_{eff}^ϕ represents an effective diffusion coefficient that controls the precipitate growth kinetics of phase ϕ. This parameter is defined according to

$$\frac{1}{D_{eff}^\phi} = \sum_i \frac{(\nu_i^\phi)^2}{x_i D_i} \tag{4.11}$$

with *i* = Y, Ti. x_i and D_i are the mole fraction and diffusion coefficient of species *i* in the matrix phase, respectively. Under the assumption that the Y:Ti ratio of precipitates of a given phase is constant for all precipitate sizes, the parameter ν_i^ϕ is equal to the number of atoms of species *i* per constituent structural unit of precipitate phase ϕ, as summarized in Eqn. 4.5.

The term $\Delta G^\phi(n)$ is the change in free energy corresponding to the formation of a cluster of phase ϕ containing *n* structural units from the constituent atoms in solution in the matrix phase. This parameter is defined as

$$\Delta G^{\phi}(n) = n\left(g_p^{\phi} - \sum_i \nu_i^{\phi} \mu_i \right) + \sigma^{\phi}(n). \tag{4.12}$$

Here, g_p^{ϕ} is the free energy per structural unit of the precipitate phase, μ_i is the chemical potential of species *i* in the matrix phase, and $\sigma^{\phi}(n)$ is the interfacial energy of a cluster of phase ϕ and size *n*. To evaluate $\sigma^{\phi}(n)$, we assume the clusters are spherical and have a constant specific interfacial energy. Because the Y and Ti contents in NFAs are fairly dilute (typically 1 at% or less), the chemical potentials can be expressed to good approximation as

$$\mu_i = \mu_i^0(T) + RT \ln(x_i) \tag{4.13}$$

In terms of the thermodynamic parameters used to describe the solid solution phase, the term $\mu_i^0(T)$ is computed by the following expressions:

$$\mu_i^0(T) = {}^0G_i^{\alpha} + x_{Fe} \sum_j {}^{(j)}L_{Fei}^{\alpha} x_{Fe}^j + x_{Cr} \sum_j {}^{(j)}L_{Cri}^{\alpha} x_{Cr}^j \tag{4.14}$$

The free energy per structural unit g_p^{ϕ} is defined as the molar free energy of the precipitate phase as computed in Table 4.3 normalized by the moles of structural units per mole of oxide.

When numerically integrating the set of ordinary differential equations defined by Eqn. 4.7, the following set of initial and boundary conditions are applied:

$$
\begin{aligned}
& f_n^{\phi}(0)\Big|_{n>1} = 0 \\
& f_1^{\phi}(t) = \prod_i x_i^{\nu_i^{\phi}} \\
& x_i(0) = x_i^0 \\
& x_i(t) = x_i(0) - \sum_{\phi}\left[\nu_i^{\phi}\sum_{n=1}^{n_{\max}} n f_n^{\phi}(t)\right] \\
& \left.\frac{df_n^{\phi}(t)}{dt}\right|_{n\geq n_{\max}} = 0
\end{aligned}
\tag{4.15}
$$

where x_i^0 is the initial alloy concentration of species *i*, and n_{max} is the maximum cluster size considered. In this study, n_{max} was set to 10,000 structural units, which corresponds to precipitates of about 10 nm in diameter.

4.3.3 Formal considerations for the dislocation pipe diffusion mechanism

In order to incorporate precipitate growth and coarsening via dislocation diffusion into this model, some modifications to the basic equations are necessary. Qualitatively, this model assumes that each oxide precipitate or cluster is intersected by some number of dislocations, and that these dislocations act as pipes through which monomers diffuse to join or leave the clusters. Therefore, the coefficients w_n^{ϕ} must be rederived assuming a pipe diffusion mechanism, rather than normal three dimensional bulk diffusion. In performing this derivation, we follow the approach of Clouet et al. [179]. We assume that diffusion to the surface of a given cluster of size *n* with radius r_n occurs through N^D dislocation pipes of cross sectional area A^D, each intersecting the cluster normal to the surface. By the approach of Clouet et al., the concentration profile within each pipe is described by

$$x_i(r) = x_i^{\infty} \frac{r - r_n}{r} \tag{4.16}$$

where x_i^{∞} is the average concentration of species *i* far from the cluster surface and *r* is the radial distance from the center of the cluster along the axis of the pipe. The rate $w_{i,n}^{\phi}$ for species *i* is then computed by integrating the flux through the particle surface. For a dislocation diffusion mechanism, this yields

$$w_{i,n}^{\phi_D} = \frac{N^D A^D x_i^{\infty} D_i^D}{\omega^{\alpha} r_n} \tag{4.17}$$

where D_i^D is the dislocation diffusion coefficient of species *i.* In this study, we assume N^D is equal to 2 (corresponding to one dislocation completely intersecting each precipitate) and A^D is equal to the area of a circle with radius given by the lattice parameter of α-Fe. We note that this result is equivalent to that of Ardell et al. [180] in the limit of zero emission from the cluster.

In the present model, it is assumed that clusters of each phase can nucleate and grow through both normal bulk diffusion and through dislocation diffusion simultaneously. In practice, this is implemented by distinguishing between clusters of the oxide phases residing in the undefected matrix phase, designated ϕ, and those residing on dislocations, designated ϕ_D. The kinetics of the former are described using Eqn. 4.7, while the later are described using the following equation:

$$\frac{df_n^{\phi_D}(t)}{dt} = \left[J_{n-1}^{\phi_D} + I_{n-1}^{\phi_D}\right] - \left[J_n^{\phi_D} + I_n^{\phi_D}\right] \tag{4.18}$$

where the terms $J_n^{\phi_D}$ and $I_n^{\phi_D}$ are the fluxes of clusters of species ϕ_D through normal bulk diffusion and dislocation diffusion, respectively. The dislocation diffusion fluxes are defined by

$$I_n^{\phi_D} = w_n^{\phi_D}\left\{ f_n^{\phi_D}(t) - f_{n+1}^{\phi_D}(t)\exp\left[\frac{\Delta G^{\phi_D}(n+1) - \Delta G^{\phi_D}(n)}{RT}\right]\right\} \tag{4.19}$$

When evaluating the dislocation diffusion fluxes, it is assumed that only the Y atoms interact strongly with the dislocations. This assumption is based on the following observations: First, APT measurements indicate that Y segregation to dislocations is much stronger in NFAs than Ti segregation [139]. Second, Y is much less soluble in Fe than Ti [163, 164]. Therefore, the growth and coarsening rates of Y-Ti oxide precipitates in NFAs is most likely rate-limited by Y solubility and diffusion [124], and the mechanism of Ti diffusion will not have a large impact on the aggregate kinetics. Under this assumption, the effective coefficients of aggregation $w_n^{\phi_D}$ for the dislocation diffusion fluxes are expressed by

$$\begin{aligned}
\frac{1}{w_n^{\phi_D}} &= \frac{\left(\nu_{Ti}^{\phi_D}\right)^2}{w_{Ti,n}^{\phi}} + \frac{\left(\nu_{Y}^{\phi_D}\right)^2}{w_{Y,n}^{\phi_D}}, \\
w_{Ti,n}^{\phi} &= 4\pi\frac{a^{\phi}}{\omega^{\alpha}}x_{Ti}D_{Ti}n^{1/3}, \\
w_{Y,n}^{\phi_D} &= \frac{N^D A^D x_Y^D D_Y^D}{\omega^{\alpha} r_n x_{tot}^D}
\end{aligned} \tag{4.20}$$

where D_Y^D is the diffusion coefficient of Y in the dislocation pipe and x_Y^D is the mole fraction of Y atoms on dislocation sites. The term x_{tot}^D is the total fraction of dislocation sites in the system, which is assumed to be equal to the volume fraction of dislocation pipes, defined by

$$x_{tot}^D = \rho^D A^D \tag{4.21}$$

where ρ^D is the dislocation density. The free energy differences $\Delta G^{\phi_D}(n)$ are defined using Eqn. 4.12, except that the chemical potential of Y is now evaluated for a Y atom in the dislocation core, defined approximately as:

$$\mu_Y^D = \mu_Y^0(T) + \Delta E_Y^D + RT \ln\left[\frac{x_Y^D}{x_{tot}^D}\right] \tag{4.22}$$

where ΔE_Y^D is the energy of a Y atom in a dislocation core relative to the energy of a Y atom in bulk, undefected Fe.

Throughout the evolution of the functions $f_n^{\phi}(t)$ and $f_n^{\phi_D}(t)$, the monomer concentrations x_{Ti}, x_Y, and x_Y^D must be tracked explicitly. This is accomplished with the following set of equations:

$$\begin{aligned}
\frac{dx_{Ti}}{dt} &= -\left[\sum_{\phi} \nu_{Ti}^{\phi} \sum_{n=1}^{n_{Max}} n \frac{df_n^{\phi}(t)}{dt} + \sum_{\phi_D} \nu_{Ti}^{\phi_D} \sum_{n=1}^{n_{Max}} n \frac{df_n^{\phi_D}(t)}{dt}\right] \\
\frac{dx_Y}{dt} &= -\left[\sum_{\phi} \nu_Y^{\phi} \sum_{n=1}^{n_{Max}} n\left[J_{n-1}^{\phi} - J_n^{\phi}\right] + \sum_{\phi_D} \nu_Y^{\phi_D} \sum_{n=1}^{n_{Max}} n\left[J_{n-1}^{\phi_D} - J_n^{\phi_D}\right]\right] - K_{YD} \\
\frac{dx_Y^D}{dt} &= -\sum_{\phi_D} \nu_Y^{\phi_D} \sum_{n=1}^{n_{Max}} n\left[I_{n-1}^{\phi_D} - I_n^{\phi_D}\right] + K_{YD}
\end{aligned} \tag{4.23}$$

The term K_{YD} is the net rate at which Y atoms enter dislocation pipes. This rate may be cast in the formalism of Slezov as flux in the form of Eqn. 4.8, describing the reaction of Y atoms on the lattice with dislocation sites to form Y bound to dislocations. The resulting expression is

$$K_{YD} = 4\pi D_Y \frac{a^{\alpha}}{\omega^{\alpha}}\left[x_Y\left(x_{tot}^D - x_Y^D\right) - x_Y^D \exp\left[\frac{\Delta E_Y^D}{RT}\right]\right] \tag{4.24}$$

where a^{α} and ω^{α} are the atomic radius and volume of Fe, respectively. The conditions defined in Eqn. 4.15 still apply, with the following modifications for the monomer concentrations:

$$\begin{aligned} x_Y(0) &= x_Y^0(1 - x_{tot}^D) \\ x_Y^D(0) &= x_Y^0 x_{tot}^D \end{aligned} \tag{4.25}$$

4.3.4 Summary of model parameters

A number of parameters and physical quantities are necessary for evaluating this model, which may be generally categorized into kinetic quantities, thermodynamic quantities, and geometric quantities. These quantities are summarized in Table 4.4.

Table 4.4: Physical quantities and parameters used in the kinetic precipitation model.

Parameter	Description	Value	Source
ω^{ϕ}	Volume per structural unit of the precipitate phase ϕ (m^3)	Y_2O_3: 3.9×10^{-29} $Y_2Ti_2O_7$: 6.6×10^{-29} Y_2TiO_5: 1.1×10^{-28} TiO_2: 3.1×10^{-29} Fe: 1.2×10^{-29}	[154, 155, 158]
D_i^0	Pre-exponential factor for diffusion coefficient of species *i* (m^2/sec)	Ti: 0.21 Y: 8.0×10^{-7} Y (dislocation): 8.0×10^{-7}	[175, 176]
Q_i	Activation energy for diffusion coefficient of species *i* (kJ/mol)	Ti: 293.2 Y: 218.1 Y (dislocation): 109.0	[175, 176, 181-185]
σ_0	Intercept of specific interfacial energy expression Eqn. 4.27 (J/m^2)	Pipe diffusion model: 1.70 Standard model: 2.57	Best model fits
A	Slope of specific interfacial energy expression Eqn. 4.27 (J/m^2)	-1.2	Interpolation of data from [186, 187]
μ_O	Background O chemical potential (kJ/mol)	Pipe diffusion model: -415.1 Standard model: -474.4	Best model fits
ΔE_Y^D	Y-Dislocation binding energy (kJ/mol)	-241.2	DFT calculation in this work
ρ^D	Dislocation density (m^{-2})	10^{15}	Approximate value from [124]

The kinetic quantities are the diffusion coefficients of the Y and Ti monomers. For normal bulk diffusion, D_{Ti} has been taken from experimental measurement [175], and D_Y has been taken from first principles-based diffusion theory [176]. While no experimental value of D_Y is available, segregation measurements have been found to be reasonably consistent with the first principles-based value [124]. Arrhenius parameters for these diffusion coefficients are

provided in Table 4.4. No value of the dislocation diffusion coefficient D_Y^D has yet been determined, however in many metals it has been found that using the value of the bulk diffusion coefficient with a reduction of 40-60% in the activation energy is a reasonable approximation of this parameter [181-185]. Therefore, we will assume that D_Y^D is equal to D_Y evaluated using one-half the activation energy. In addition to the thermodynamic parameters listed in Table 1, the thermodynamic quantities required by this model include the specific interfacial energies σ_0^ϕ and the dislocation binding energy ΔE_Y^D. The former is treated as an adjustable parameter, as described in Sec. 4.3.6, while the latter is calculated in this study via DFT (see Sec. 4.3.8). Finally, the geometric quantities include principally molar volumes of the various phases in the system. These are summarized in Table 4.4. Once all of the necessary quantities were determined, the model differential equations were numerically integrated using the CVODE module of the SUNDIALS package [188].

4.3.5 Calculation of the Y-dislocation binding energy via DFT

In order to incorporate the effects of dislocation pipe diffusion into the kinetic model, the binding energy of a Y atom to a dislocation must be determined. The subject of solute interactions with dislocations in Fe has been well-studied, however in most cases the solutes of interest are interstitial solutes such as C or N. The interaction energy of Y with dislocations in Fe is currently unknown. In this study, DFT calculations have been employed to compute a first approximation for the Y-dislocation binding energy in Fe. To demonstrate that this approach can produce reasonably accurate results, the binding energies of C, O, and N with a dislocation in Fe were calculated as well and compared with available values from the literature and from elasticity theory.

The dislocation model chosen for these calculations is the [100](010) edge dislocation. This dislocation type was chosen for its structural simplicity, and while they are not involved in the predominant slip mechanisms in Fe [189], dislocations of this type are present in Fe and appear to play an important role in crack nucleation [190]. Fig. 4.10a illustrates the atomistic model of this dislocation structure, viewed along the [001] direction (i .e., along the core of the dislocation). Periodic boundary conditions are employed when calculating the energy of the dislocation structure via DFT, and a supercell was constructed with an array of four dislocations arranged such that their displacement fields are mutually compensated between periodic images. Fig. 4.10b depicts a schematic illustration of the simulation supercell used in these calculations.

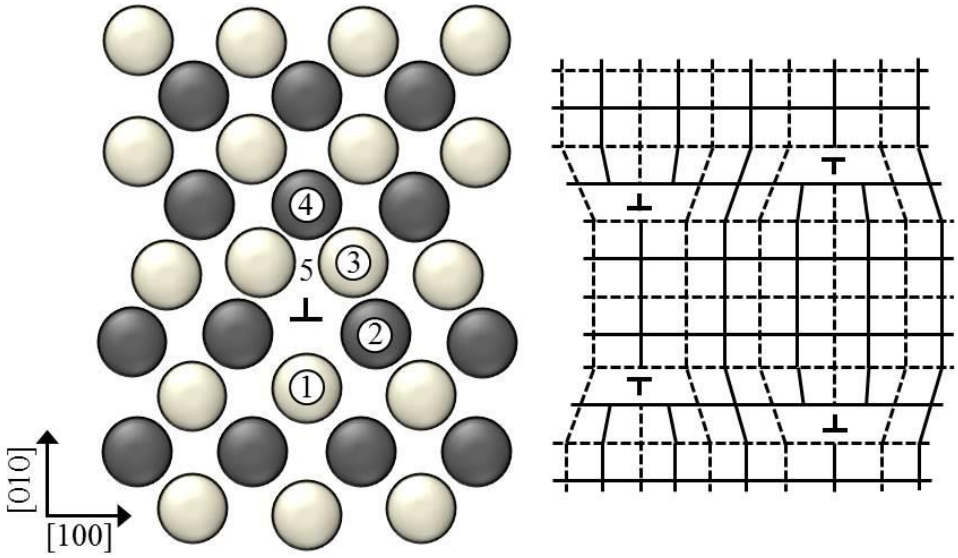

Figure 4.10a (left): Atomistic model of [100](010) dislocation. The colors denote different atomic planes parallel to the [001] direction. For binding energy calculations, Y is inserted into substitutional sites 1-4, and C/N/O is inserted into interstitial site 5. b (right): Schematic illustration of the 4 dislocation array in the simulation supercell used to calculate dislocation binding energies when viewed along the [001] direction. The solid and dashed lines correspond to the planes composed of the light and dark atoms in the atomistic model of Fig. 1a, respectively.

The solid and dashed lines in Fig. 4.10b correspond to the planes composed of the light and dark atoms in the atomic model of Fig. 4.10a, respectively. In the [001] direction, the supercell was three bcc cubic unit cells in height.

Dislocation binding energies were determined using the following expression:

$$\Delta E_i^D = \left(E_{i+Fe}^D + E_{Fe}^{bulk}\right) - \left(E_{Fe}^D + E_{i+Fe}^{bulk}\right) \tag{4.26}$$

where E_{i+Fe}^D is the DFT-calculated energy of the dislocation structure containing a solute atom of species *i*, E_{Fe}^D is the energy of the solute-free dislocation structure, E_{i+Fe}^{bulk} is the energy of bulk, undefected Fe with a single solute of species *i*, and E_{Fe}^{bulk} is the energy of pure, undefected Fe. When calculating E_{i+Fe}^D, the solute Y atom was placed on sites 1-4 in Fig. 4.10a, while the C, N, or O atom was placed on site 5. For the bulk Fe calculations, a 3×3×3 cubic bcc supercell was used, with a single solute atom. In the case of Y, the solute atom was placed on a substitutional site, and in the case of C, N, or O the solute atom was placed on an octahedral interstitial site.

All calculations were performed using the Vienna Ab Initio Simulations package (VASP) [62-65] in the generalized gradient approximation using the Perdew-Burke-Ernzerhof [66] exchange-correlation functional, and using the projector-augmented wave method [67]. For all calculations, a 3×3×3 k-point mesh and a 400 eV energy cutoff were used, and all calculations were spin polarized. Cell shape and ionic relaxations were permitted in both the bulk and dislocation structure calculations.

To estimate possible errors in Y-dislocation binding energy with supercell size, multiple dislocation cells of different sizes were tested. The basic supercell depicted schematically in Fig. 4.10b consists nominally of 6 cubic bcc unit cells in the [100] and [010] directions and 3 unit

cells in the [001] direction. Three additional supercell sizes were tested with sizes 8×6×3, 6×8×3, and 6×6×4, respectively. The first tests convergence with respect to distance between dislocations in the [100] direction, the second with respect to distance between dislocation cores in the [010] direction, and the third with respect to distance between solute atoms along the dislocation line in the [001] direction.

4.3.6 Physical quantities used as adjustable parameters

There are two additional quantities used in the present modeling framework that are not precisely known; these are the specific oxide-matrix interfacial energies σ_0^ϕ and the background O chemical potential μ_O. These quantities would be quite difficult to accurately determine and are therefore used as adjustable parameters in the kinetic model, and used to fit the model results to experimental measurements of the change in mean precipitate size as a function of aging time. The constraints and strategy for performing this fitting is the subject of this section.

In principle, the specific interfacial energies σ_0^ϕ represent eight independent parameters; one for each of the oxide phases, in both bulk and dislocation configurations. If all eight quantities are used as fitting parameters, then the model would likely have too many degrees of freedom to allow for a unique model fit. Therefore, two approximations were employed to reduce these quantities to a single adjustable parameter. First, we have assumed that the oxide particles in the undefected matrix and those residing on dislocations have the same interfacial energy. Second, we have assumed that the interfacial energies of the four oxide phases are related by a simple linear relationship in the Ti fraction of metal atoms in the oxide, according to the following expression:

$$\sigma_0^\phi = \sigma_0 + A x_{Ti}^\phi \tag{4.27}$$

where x_{Ti}^{ϕ} is the fraction of metal atoms per mole of oxide phase ϕ that are Ti. The slope *A* was determined by interpolation between the bare specific surface energies of Y_2O_3 and TiO_2 [187]. While this assumption has not been verified for the oxide phases used in the present model, experimental measurements of the interfacial energy between liquid Ni and Ti-bearing YSZ follow a linear relationship in Ti fraction like that of Eqn. 26 reasonably closely [186]. The parameter σ_0 from Eqn. 26 and the background O chemical potential μ_O defined in Table 4.3 are then the two adjustable parameters in this model. Both are assumed to be constant with temperature.

The model was fit using experimental data and observations from the alloy MA957. This alloy was chosen because of the abundance of data available from a uniform stock material [124, 130, 131, 135], which removes complexities associated with fitting to data from alloys with different compositions and processing histories. The following constraints were employed when adjusting the parameters σ_0 and μ_O. First, when starting with the nominal composition of MA957, the predominant Y-containing precipitate phase predicted by the model must be a complex Y-Ti oxide (i. e., $Y_2Ti_2O_7$ or Y_2TiO_5, and not Y_2O_3). This constraint is based upon extensive experimental evidence that Y precipitates in the form of Y-Ti-O nanoparticles in alloy MA957, and not Y_2O_3. Effectively this constraint sets a lower limit on μ_O; below a certain μ_O threshold, a combination of Y_2O_3 and Ti atoms in solution becomes thermodynamically more stable than the complex oxides $Y_2Ti_2O_7$ or Y_2TiO_5. Second, the mean precipitate number density, and volume fraction after the initial simulated heat treatment of the supersaturated solid solution must be consistent with the values measured in the MA957 stock material via SANS [124]. Within the range of values that kept these criteria satisfied, σ_0 and μ_O were adjusted to

best match SANS measurements of mean Y-Ti-O particle size as function of time during aging of the MA957 stock material at temperatures in the range 1223-1573 K [124, 130]. This fitting was done using a simple iterative routine to minimize the sum of the squared residual errors between model calculation and experimental measurements for the last aging time at each temperature. In an effort to isolate the dominant growth and coarsening mechanism in NFAs, this fitting was performed independently for a kinetic model that includes only conventional growth and coarsening through normal bulk diffusion (denoted hereafter the standard model) and for a kinetic model that includes both bulk and pipe diffusion mechanisms (denoted the pipe diffusion model).

4.3.7 Predictions of phases and volume fractions at equilibrium

The thermodynamic model described in Sec. 4.3.1 can be used to make certain predictions about the asymptotic behavior of NFAs, such as the identities and fractions of the phases present at equilibrium. Fig. 4.11 depicts a map of the predicted equilibrium precipitate phases at 1273 K in an Fe-14Cr-x_Y-x_{Ti} alloy as a function of the ratio $x_{Ti}/(x_Y + x_{Ti})$, where the sum $x_Y + x_{Ti}$ was constrained to be equal to 1 at%, and the background O chemical potential in terms of equivalent P_{O_2}.

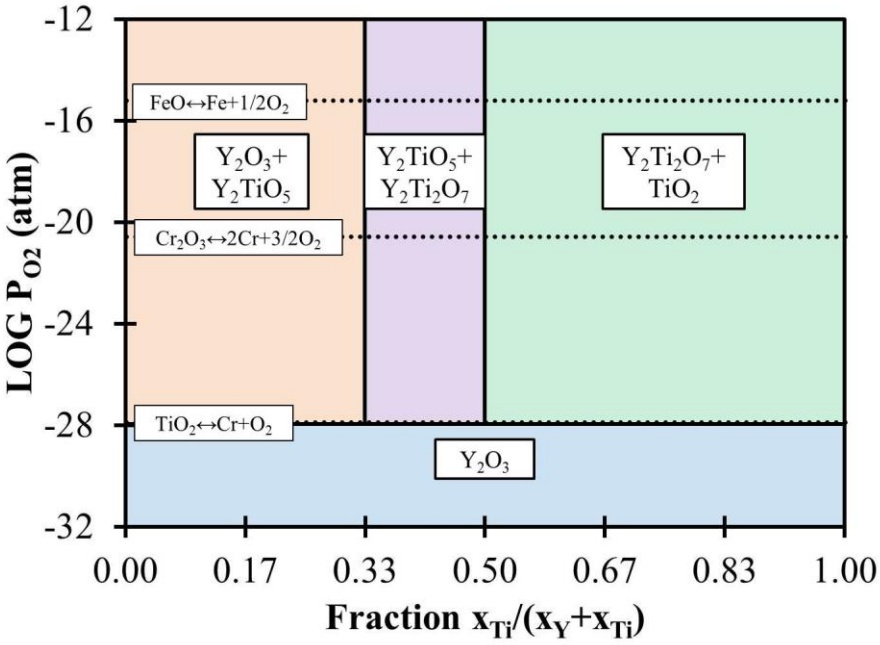

Figure 4.11: Equilibrium phases predicted by the thermodynamic model as a function of O partial pressure P_{O_2} and nominal fractions of Ti and Y in the alloy Fe-14Cr-x_Y-x_{Ti} at 1273 K. Dotted lines correspond to the equilibrium partial pressures for the reactions FeO↔Fe+1/2O$_2$, Cr$_2$O$_3$↔2Cr+3/2O$_2$, and TiO↔Ti+O$_2$

Lines corresponding to the equilibrium partial pressures for the reactions FeO↔Fe+1/2O_2, Cr_2O_3↔2Cr+3/2O_2, and TiO↔Ti+O_2 are included as well. Over the range of P_{O_2} for which Fe or Cr oxides are stable, the predicted phases are Y_2O_3, TiO_2, $Y_2Ti_2O_7$, and Y_2TiO_5, depending on Y and Ti alloy composition. Most NFAs occupy the Ti-rich composition range for which the predicted stable phases are TiO_2 and $Y_2Ti_2O_7$, in qualitative agreement with many experimental observations [124, 131, 135, 136, 191]. The phase stability behavior is fairly insensitive to P_{O_2}, with no change in phase stability above $P_{O_2} = 10^{-28}$ atm. Below this limit, only Y_2O_3 appears as a precipitate phase, and all Ti remains in solution. This value is well below the stability limit for Cr_2O_3, and is therefore most likely an unphysical value for NFAs under any condition.

The volume fraction of precipitate phase is an alloy property of particular interest in NFAs; to a first approximation, the change in strength due to the precipitates is proportional to the square root of this volume fraction [8]. Fig. 4.12 compares the precipitate volume fraction in a large number of NFAs with varying Ti and Y contents as measured via SANS [1, 129-131, 136, 137, 192-195] with the equilibrium volume fractions of oxide phases predicted by the thermodynamic model for the same alloys.

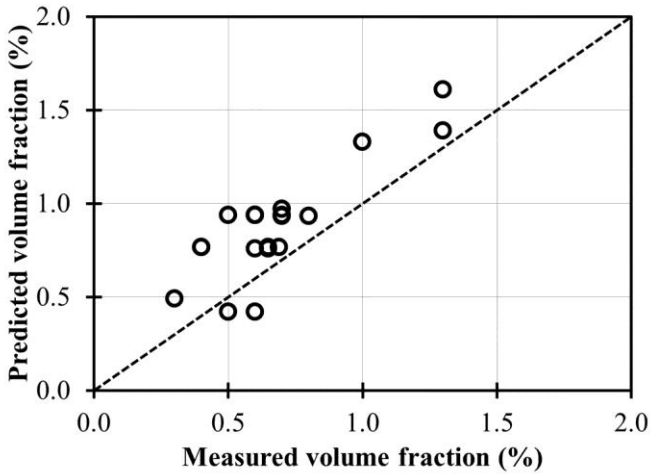

Figure 4.12: Comparison of measured precipitate volume fractions (citations in text) with the equilibrium oxide volume fractions predicted by the thermodynamic model.

In some cases, the experimental data in Fig. 4.12 include only the nm-scale Y or Y-Ti oxide particles and not the larger Ti oxide particles; for cases where this was explicitly stated in the experimental methods [1, 131, 136], only the predicted volume fractions of the Y and Y-Ti oxides were included in the corresponding model predictions in Fig. 4.12. In most cases, the predicted volume fractions are slightly above the measured volume fractions. This could conceivably be due to the SANS measurements missing precipitates that are outside the size range for which the measurements have been tuned, resulting in a small but systematic under-reporting of volume fractions. This explanation has been offered by Cunningham et al. [124] for

the apparent drop in precipitate volume fraction observed during extended aging of the NFA MA957, where precipitates may have grown beyond the size range for which the SANS measurements have been optimized. Aside from this error, Fig. 4.12 demonstrates reasonably good agreement between the model predictions and experiment. This suggests that the model adequately captures the trends in both the amount and identities of precipitate phases with Y and Ti alloy content.

In the effort to optimize NFA properties with respect to alloy composition, significant attention has been given to the effects Ti content on microstructure and mechanical properties. Oksiuta et al. [191] examined the precipitate microstructure and the Charpy impact toughness of an Fe-12Cr-0.2Y-*x*Ti (at%) NFA, where *x* varied from 0.1 to 0.6 at%. Fig. 4.13 depicts the equilibrium oxide volume fractions predicted by the thermodynamic model for this alloy on the primary axis, and the measured Charpy upper shelf energy on the secondary axis, as functions of Ti content.

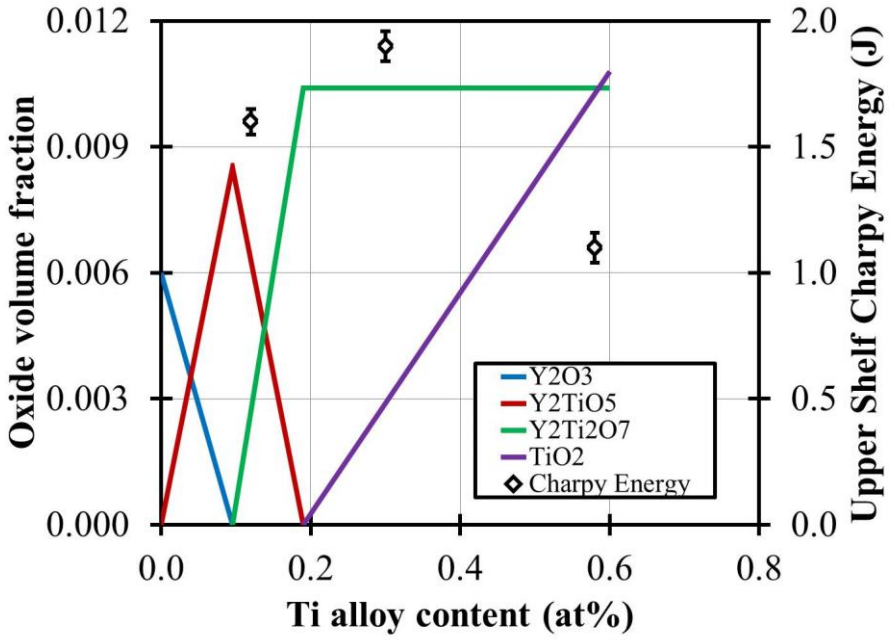

Figure 4.13: Predicted equilibrium oxide fraction (left axis) and measured Charpy upper shelf impact energy measured by Oksiuta et al. [191] (right axis) as a function of Ti alloy content in an Fe-12Cr-0.2Y-*x*Ti (at%) NFA.

The thermodynamic model predicts that the Y-Ti oxide volume fraction will plateau at about 0.2 at% Ti, beyond which additional Ti only increases the volume fraction of TiO_2. This is in qualitative agreement with the observations of Oksiuta et al., who noted significant Ti oxide precipitation in the alloy containing 0.6 at% Ti, but not in the 0.1 or 0.3 at% Ti alloys [191]. A significant drop in Charpy toughness was measured between the 0.3 at% Ti and 0.6 at% Ti alloys, a composition range that corresponds to a significant increase in the predicted volume fraction of TiO_2. Oksiuta et al. attributed this drop in Charpy toughness to the precipitation of a large amount of Ti oxide in the 0.6 at% Ti alloy, which appeared as much larger precipitates often on or near grain boundaries. This result suggests that Ti oxide precipitation should be minimized in order to maximize Charpy toughness. From the predictions of the thermodynamic

model in Figs. 4.11 and 4.13, TiO_2 formation can be avoided in alloys with a nominal Ti:Y ratio equal to 1.

While the thermodynamic calculations discussed above can be used to predict the identities and volume fractions of precipitate phases in equilibrium, the kinetic modeling approach outlined in sections 4.3.2-4.3.6 must be used to examine the evolution of the precipitate size distribution as a function of time, temperature, and alloy composition. This following sections first presents the results of the DFT calculations of the Y-dislocation binding energy, the fitting of the parameters σ_0 and μ_O, and finally the predictions of the best-fit kinetic model of the precipitate size evolution as a function of time, temperature, and alloy composition.

4.3.8 DFT calculations of solute-dislocation binding energies

The binding of the interstitial solutes such as C, N, and O to dislocations in α-Fe has been studied extensively from both experimental [196-200] and theoretical [201-206] approaches. In this subsection, we will first compare the results of the DFT calculations of the dislocation binding energies of these three solutes with results from the literature, to ensure that the simplified approach taken here can produce reasonably quantitative values.

Table 4.5 presents the dislocation binding energy values of C, N, and O resulting from the DFT calculations described in Sec. 4.3.5, as well as values determined in previous studies through a variety of experimental and theoretical approaches.

Table 4.5: Solute-dislocation binding energies resulting from DFT calculations of this study as well as other theoretical methods and experimental measurements from the literature.

Element	Binding energy (eV)	Method	Source
C	-0.66-0.75, -0.70 mean	Empirical potential	[201, 203, 205]
	-0.50-0.75, -0.62 mean	Elasticity theory	[202, 206]
	-0.45-0.75, 0.57 mean	Experiment	[196-198]
	-0.67	DFT calculation	This study
N	-0.40-0.80, -0.56 mean	Experiment	[199, 200]
	-0.35	DFT calculation	This study
O	-1.0	Elasticity theory	[206]
	-0.90	DFT calculation	This study
	Y Binding energy (eV)	Y occupation site	Supercell size
Y	-2.62	1	6×6×3
	-2.47	1	6×6×4
	-2.46	1	6×8×3
	-2.61	1	8×6×3
	-2.11	2	8×6×3
	-2.17	3	8×6×3
	0.29	4	8×6×3

Reasonably good agreement is observed for all three elements. Also presented in Table 4.5 are the Y-dislocation binding energies calculated for site 1 in Fig. 4.10a using four different supercell configurations and for sites 2-4 using a single configuration. The strongest binding energy is calculated for site 1, where all four values fall within the range of -2.47 and -2.65 eV, indicating that convergence errors with respect to cell size are likely to be on the order of 200 meV. While this is not an insignificant error in absolute terms, it is less than 10% of the magnitude of the overall value and the predicted values should be accurate enough to assess the possible impact of dislocation pipe diffusion on precipitate growth and coarsening. The binding energies calculated for sites 2 and 3 were somewhat weaker than site 1, but still substantial. Of the sites tested, only site 4 resulted in a repulsive interaction. In the kinetic modeling results described below, a value of -2.54 eV was used for the Y-dislocation binding energy,

corresponding to the average of the four values determined for site 1. These calculations predict a very strong Y dislocation binding energy, which may help to explain the strong Y segregation to dislocations observed in the analysis of some APT specimens [139]. We note that the non-local elasticity theory of Wang [206] predicts a Y binding energy of -1.62 eV. While this is a strong attractive interaction in qualitative agreement with the DFT calculations performed here, it demonstrates the need for an electronic structure method such as DFT to capture the full effect.

4.3.9 Model fitting to nanoprecipitate size evolution data in MA957

As described in Sec. 4.3.6, the interfacial energy parameter σ_0 and the background O chemical potential μ_O were used as adjustable parameters in order to fit the kinetic precipitation model to SANS measurements of mean precipitate size as a function of time and temperature in the NFA MA957, under two different model cases: in the first case, referred to as the standard model, it is assumed that precipitate growth and coarsening occurs only through normal three dimensional bulk diffusion. In the second case, referred to as the pipe diffusion model, precipitate growth and coarsening occurs through both normal bulk diffusion and dislocation diffusion mechanisms.

The best fit values of the interfacial energies in the standard and pipe diffusion models are depicted in Fig. 4.14a using the form of Eqn. 4.27. Also included in Fig. 4.14a are the values of the bare surface energies of Y_2O_3 and TiO_2, as well as the liquid Fe-TiO_2 interfacial energies [187].

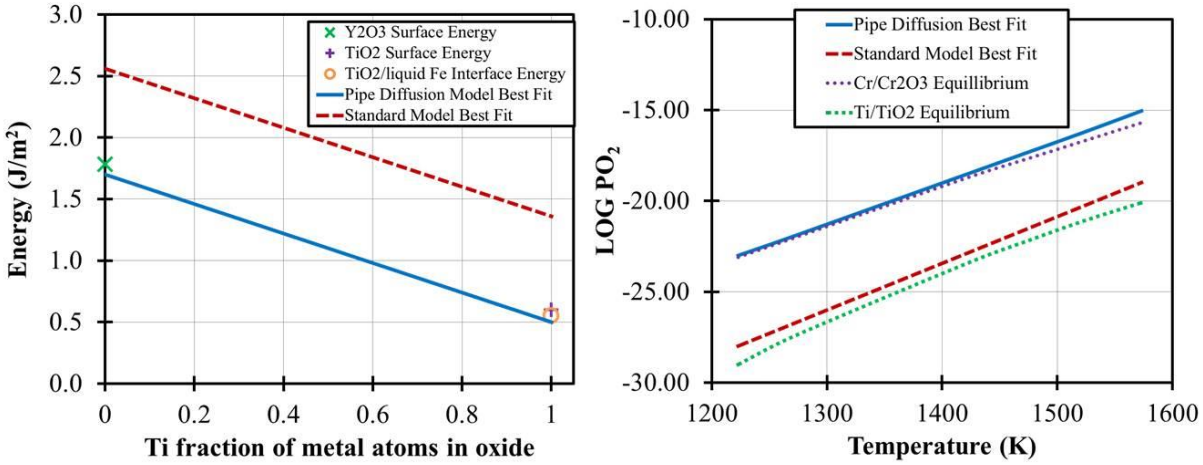

Figure 4.14a (left): Best fit values for the interfacial energies used in the kinetic precipitation model, using the form of Eqn. 26. b (right): Best fit values of the O chemical potential, in terms of equivalent P_{O_2}. Curves corresponding to equilibrium values of P_{O_2} for the reactions 2Cr + 3/2 O_2 ↔ Cr_2O_3 and Ti + O_2 ↔ TiO_2 are included for reference.

The best-fit values for the standard model are quite high, and are near the highest range reported even for incoherent planar interfaces [207], while the values for the pipe diffusion model are quite reasonable and close to the surface and interfacial energies of Y_2O_3 and TiO_2. In Fig. 4.14b, the best-fit O chemical potentials for the standard and pipe diffusion models are plotted in terms of equivalent P_{O_2} as a function of temperature. Also include are the curves corresponding to O chemical potential for which the reactions 2Cr + 3/2 O_2 ↔ Cr_2O_3 and Ti + O_2 ↔ TiO_2 are in equilibrium. The best fit chemical potential for the pipe diffusion model is quite low but is just above the equilibrium curve for Cr/Cr_2O_3, which is physically plausible. However, the best-fit curve for the standard model is well below the Cr/Cr_2O_3 equilibrium curve. It is difficult to justify this value physically, because Cr_2O_3 is often observed among the oxide scales on NFAs.

Fig. 4.15 depicts the volume fractions of the Y and Ti oxide phases in MA957 as functions of time during initial heat treatment at 1338 K, as predicted by the best-fit standard and pipe diffusion models.

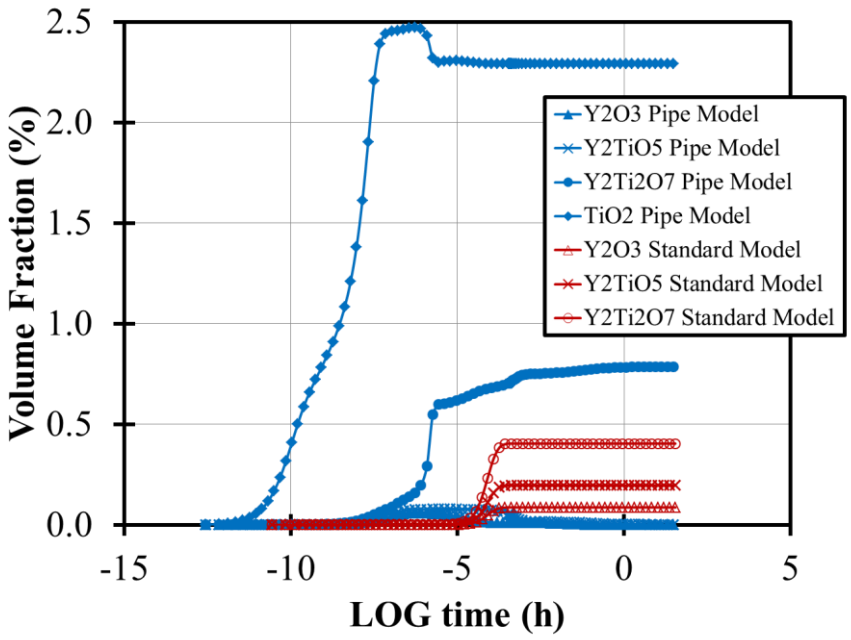

Figure 4.15: Oxide volume fractions in MA957 as predicted by the best-fit models.

In both model cases, the predominant Y oxide phase is $Y_2Ti_2O_7$. However, the pipe diffusion model also predicts the formation of a significant amount of TiO_2, in qualitative agreement with several experimental observations for this alloy [124, 131], while no TiO_2 formation is predicted by the standard model. This result is a consequence of the higher interfacial energy and lower O chemical potential in the standard model, which yield a significantly higher barrier to nucleation of TiO_2 relative to the pipe diffusion model. In both model cases, the precipitation occurs over a very short timescale, with steady state volume fractions appearing on the order of seconds. While no data are available regarding the kinetics of precipitation in MA957 during the initial heat treatment of which we are aware, in many other NFAs the appearance of the precipitates

does seem to be very rapid during the initial heat treatment of the mechanically alloyed material [137, 167].

When comparing the kinetic model results to experimental measurements, the simulated heat treatments consisted of an initial heat treatment of the solid solution at 1338 K, to first match the MA957 stock material condition, followed by extended aging at temperatures between 1223 K and 1523 K, to recreate the subsequent experimental aging conditions. The processing parameters for the stock MA957 material are proprietary and hence the exact time of the initial heat treatment is unknown, however for similar alloys the initial heat treatment step lasts between 1 and 10 hours [125, 131]. In the present study we have taken 3 hours as a typical value, although in practice the results are not significantly sensitive to the choice of this time. This insensitivity arises because the precipitation kinetics in NFAs are characterized by rapid nucleation followed by comparatively slow growth and coarsening, and in the present model the mean precipitate size changes by less than 5% at 1338 K over the time span of 1 to 30 hours in both the standard and pipe diffusion cases. Therefore, any initial heat treatment time selected within this range gives a nearly identical particle size distribution. Table 4.6 compares the values of nanoprecipitate mean radius, number density, and volume fraction for just after the initial heat treatment, calculated by the two best-fit model cases and as measured by SANS, in the MA957 stock material [124]. Both models show good agreement with the experimental measurement.

Table 4.6: Volume fraction, number density, and mean radius of nanoprecipitates in stock MA957 after initial heat treatment, as measured by SANS and as calculated by the best-fit pipe diffusion and standard models (using 3 hour initial heat treatment time).

Source	Volume Fraction (%)	Number Density ($\times 10^{23}$ m^{-3})	Mean Radius (nm)
SANS Measurement [124]	0.9±0.1	9.0±1.2	1.35±0.02
Pipe Diffusion Model	0.8	8.8	1.32
Standard Model	0.7	7.1	1.34

The change in the mean precipitate radius in MA957 as a function of aging time is illustrated in Fig. 4.16, as calculated in the best-fit model cases and measured experimentally [124, 130].

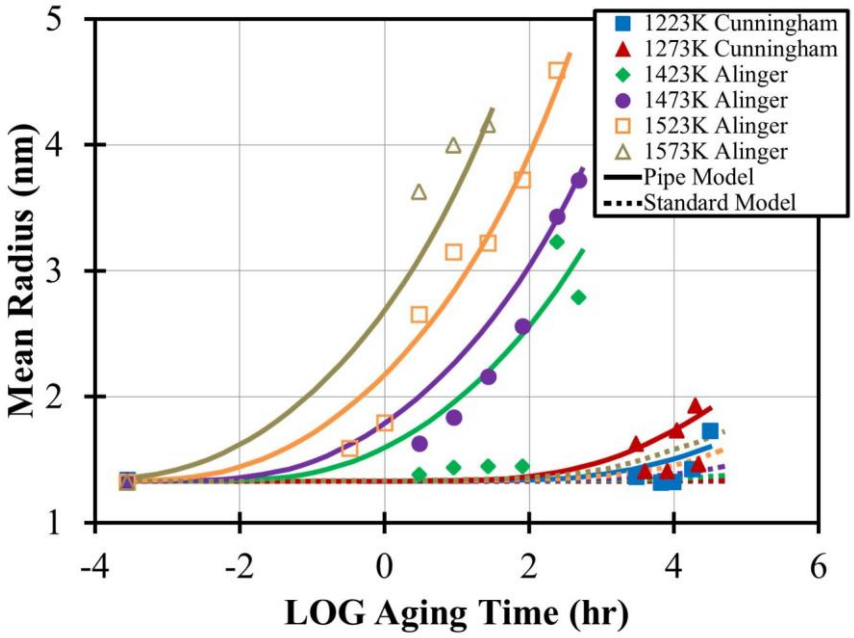

Figure 4.16: Mean $Y_2Ti_2O_7$ precipitate radius in alloy MA957 as a function of time during thermal aging. Data points represent experimental measurements [124, 130] while the curves represent the calculations of the best fit models.

The best-fit pipe diffusion model shows reasonably good agreement with the experimental data especially for longer aging times. On the contrary, the best fit standard model fails to capture

any significant coarsening. The failure of the best-fit standard model to reproduce the experimental coarsening behavior is due to the constraint that the precipitates predicted by the model must be Y-Ti oxide phases and not just Y_2O_3: in order to further enhance coarsening in the standard model, a lower O chemical potential must be used. This low PO_2 requirement emerges in the standard model because Y has very low solubility in the undefected ferrite matrix, which can only be enhanced to values consistent with measured coarsening through destabilizing the oxide through very low PO_2. However, it is evident form Fig. 4.14b that the O chemical potential used in the standard model is just above the value corresponding to Ti/TiO_2 equilibrium, and as demonstrated in Fig. 4.11, below this threshold Y_2O_3 becomes the only stable oxide phase. Overall, for any reasonably physical fitted parameters the standard model predicts coarsening rates well below measured values. Therefore, there does not seem to be any combination of interfacial energies and O chemical potential values for which the standard model can reproduce both the correct nanoprecipitate phases and coarsening behavior that match experimental observations; these features can only be self-consistently reproduced by the pipe diffusion model. This result is in agreement with the conclusions of Cunningham et al [124], who observed that no physically plausible mechanism could seem to account for the nanoprecipitate coarsening measured in MA957 that did not include the effects of dislocation diffusion.

4.3.10 Predictions of the fitted model for long term thermal stability and alloy design

The best-fit pipe diffusion model captures many the significant features of the nanoprecipitate size distribution evolution in the NFA MA957 during heat treatment over a wide range of aging conditions, and can therefore be used to make predictions for conditions that have

not been explored experimentally. This section explores the predictions of this model for coarsening behavior over timespans relevant to nuclear power applications, as well as the effects of Ti alloy content on nanoprecipitate phase and mean size. Fig. 4.17 illustrates the model predicted change in mean nanoprecipitate radius in MA957 after aging for 50 and 80 years as a function of aging temperature.

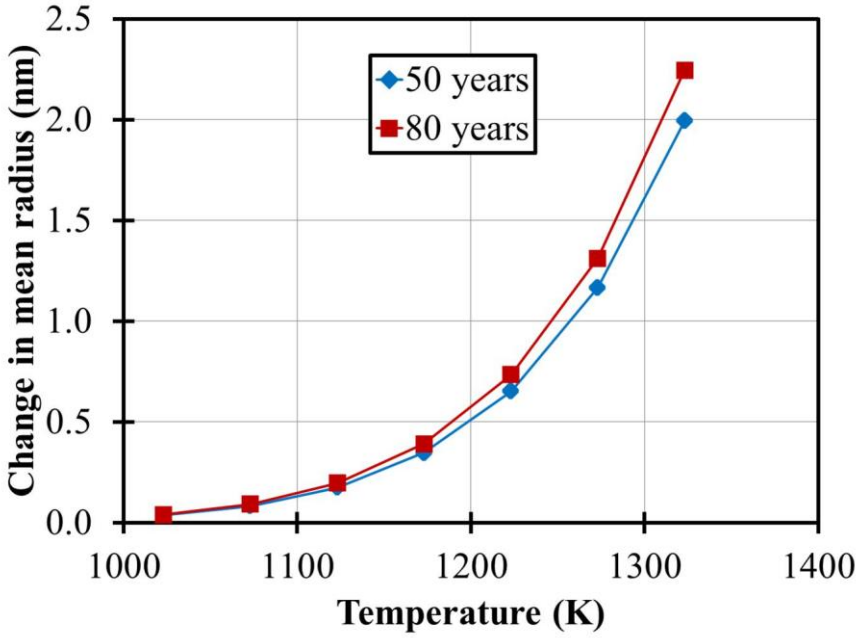

Figure 4.17: Predictions from the best fit pipe diffusion model of the change in mean $Y_2Ti_2O_7$ precipitate radius in alloy MA957 after 50 and 80 years as a function of aging temperature.

Very little coarsening is predicted over these timespans in the temperature range most of interest for NFA applications (1000-1100 K). While this is an encouraging prediction, it does not account for the role that irradiation may play on nanoprecipitate size evolution. Though studies have thus far indicated that the nanoprecipitates in NFAs are resistant to direct irradiation-induced dissolution [208, 209], the potential effects of irradiation on coarsening via dislocation pipe diffusion is presently unknown and should be an emphasis of future modeling efforts.

It has been repeatedly demonstrated that adding Ti to Y-based NFAs appears to refine the mean size of the nanoprecipitates, however the mechanism behind this effect is currently unknown. In Fig. 4.18, the predicted mean Y bearing nanoprecipitate radius of an Fe-14Cr-0.14Y-*x*Ti (at%) alloy after 3 hours at 1338 K is plotted as a function of Ti alloy content. Also presented are the volume fractions of the resulting Y containing nanoprecipitate phases. The volume fraction of TiO_2 precipitates is not included in Fig. 4.18 because these precipitates are much larger features than the nanometer-scale Y-Ti particles, and are not of primary interest in this study.

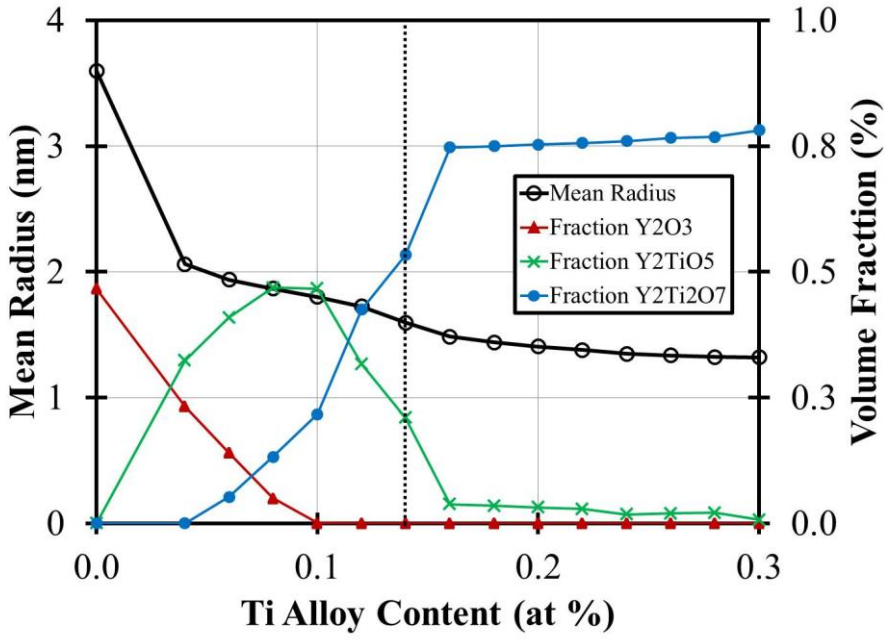

Figure 4.18: Model predictions from the best fit pipe diffusion model of the Y and Y-Ti oxide mean precipitate radius and volume fractions after heat treatment for 3 hours at 1338 K as a function of Ti content in an Fe-14Cr-0.14Y-xTi alloy. A dashed line indicates an alloy composition of 0.14 Ti, giving a Y:Ti ratio of 1:1.

The model predicts a reduction in mean nanoprecipitate size with increasing Ti alloy content, in qualitative agreement with numerous experimental observations [1, 134, 210, 211]. This reduction in size corresponds to a gradual change in the dominant oxide phase, from Y_2O_3 to

Y_2TiO_5 and finally to $Y_2Ti_2O_7$. Beyond 0.14 at% Ti a significant volume fraction of TiO_2 appears as well, though this data is not shown.

In the present model, the promotion of the complex Y-Ti oxide phases over Y_2O_3 results in a smaller mean particle size due to the following two mechanisms: (i) the phases Y_2TiO_5 and $Y_2Ti_2O_7$ have moderately stronger driving forces for precipitation than Y_2O_3 and (ii) the presence of Ti monomers in addition to Y monomers provides more opportunities for nucleation of the Y-Ti-O phases to occur. Taken together, these features result in a higher nucleation rate and subsequently a refined mean particle size. This effect is somewhat dependent upon the treatment of the interfacial energies in the present model, however the same qualitative behavior is observed even if the interfacial energies of all three Y-bearing oxides are assumed to be equal. According to the model predictions, most of the particle size refinement of Ti is achieved by around 0.16 at% Ti, or slightly greater than a Ti:Y ratio of 1. The model developed here would presumably yield similar effects for other alloying species that form complex oxides with Y, such as Al, however discerning which dopant would optimize this effect would depend strongly on the relative interfacial energies of the respective oxide phases. As this property is currently an empirical fitting parameter, a detailed study of the interfacial energies of different Y-M complex oxides would be necessary to speculate on the possible nanoprecipitate refining benefits of other elements relative to Ti.

4.4 Key results and conclusions

In this study, a framework has been developed for studying the thermodynamic and kinetic aspects of oxide precipitation in NFAs. This framework draws upon available thermodynamic and kinetic data, DFT calculations, and a rate theory cluster-based description of precipitation

kinetics to explore coarsening mechanisms as well as phase stability and particle size as functions of alloy composition. The principal conclusions of this effort are the following:

- DFT calculations of Y-Ti-O clustering energetics in Fe indicated that semi-coherent clusters resembling stoichiometric Y and Ti oxides are remarkable stable in Fe, even for very small sizes. Furthermore, the precipitate volume fractions and phase identities predicted by the equilibrium thermodynamic model are in reasonably good agreement with many experimental observations. These results provide additional evidence that the nanoprecipitates in most NFAs are primarily equilibrium Y-Ti oxide phases.
- DFT calculations and extensive model fitting to coarsening data in the NFA MA957 indicate that dislocation pipe diffusion is the dominant mechanism behind the coarsening of the nanometer-scale Y-Ti oxide precipitates. This corroborates the conclusions of Cunningham et al. [124] based upon empirical analysis of coarsening data.
- The extrapolations of the best-fit model indicate that little coarsening of the nanoprecipitates in the NFA MA957 should be expected over timespans of 50-80 years at operating temperatures relevant to nuclear power applications. This is in agreement with Cunningham et al. who predicted the precipitates would be thermally stable up to about 1123 K.
- The particle refining benefit of small additions of Ti is predicted to be due to the increased opportunities and driving force for nucleation of Y-Ti oxides over Y_2O_3. The majority of this beneficial effect is achieved for nominal alloy compositions with Ti:Y ratio slightly greater than 1. Larger values of this ratio lead to significant TiO_2

precipitation, which correlates with only very minor reduction in precipitate size and appears to be detrimental to certain mechanical properties [191].

While a number of approximations were adopted in assembling this framework, with reasonable physical parameter values the resulting model adequately captures many phenomena observed during nanoprecipitate evolution in NFAs. However, significant fitting to experimental data was employed to evaluate two key parameters: the specific oxide-matrix interfacial energy and the background O chemical potential. Furthermore, two other key parameters, the Y dislocation diffusion coefficient and the Y-dislocation binding energy, were given highly approximate treatment. This model should therefore be regarded as semi-empirical, and not fully fundamental or quantitative. Nevertheless, the model developed in this study has provided the following significant mechanistic insights into nanoprecipitate behavior in NFAs: The thermodynamic component of the model yields strong driving forces for the precipitation of Y-Ti oxides that result in very rapid nucleation, even assuming rather high interfacial energies of 1-2 J/m^2. In addition to the large formation enthalpy of the oxide phases, these large driving forces arise in part from the very low solubility of Y in the Fe-Cr matrix. This low solubility prohibits coarsening through Ostwald ripening; consequently the nm-scale precipitates remain quite stable after the rapid nucleation period. In fact, under standard assumptions of precipitation theory significant coarsening of the nanoprecipitates does not seem possible at all, some additional mechanism such as pipe diffusion must be invoked to reproduce the coarsening observed experimentally. By the method detailed in [124] the best-fit pipe diffusion model yields an effective activation energy for coarsening of 603 kJ/mol, comparable but slightly lower than the value of 673 kJ/mol determined by Cunningham et al [124]. Given that the estimated activation

energy of D_Y^D is only 109 kJ/mol, it is evident that the coarsening rate is dominated by Y solubility.

Though this model can serve as a foundation for future modeling efforts, the current model framework may be improved and expanded in many ways. Further study on interfacial energetics, Y-dislocation interactions and diffusion, and nanoparticle nucleation pathways would all lead to fruitful model refinement. Additionally, the present model deals only with thermal effects on the nanoprecipitate distribution, and the long term impact of irradiation on the nanoprecipitates remains a particularly significant open question.

Chapter 5: Conclusions

In the research reviewed in this document, a variety of computational materials science tools were utilized, from the conventional methods of rate theory and CALPHAD modeling to cutting edge atomistic techniques such ab initio molecular dynamics simulations. These tools were applied to three distinct projects related to thermal and radiation induced degradation of steels and Ni alloys for structural application in nuclear power systems. In this chapter, the main results of these projects will be reviewed

5.1 Theory and prediction of radiation induced segregation in Ni-Cr and Fe-Cr alloys

Radiation induced segregation is a process that can cause significant segregation of Cr near grain boundaries in Ni-Cr and Fe-Cr alloys. In the Ni-Cr system, this effect causes a substantial depletion of Cr in the region near grain boundaries, and may contribute to intergranular irradiation-assisted stress corrosion cracking. On the contrary, in Fe-Cr alloys RIS leads to Cr enrichment near grain boundaries. Many high Cr ferritic alloys are nominally near the α/α' phase boundary, and this enrichment of Cr may cause local precipitation of the Cr-rich

α’ phase, leading to embrittlement. The goal of this research project was to develop a fundamental description of the underlying atomic-level mechanisms of RIS, so that it can be better understood and predicted.

The results of this modeling effort have revealed the importance of the interstitial diffusion mechanism in RIS: in Fe-Cr alloys, fast Cr diffusion by interstitial dumbbells is the primary mechanism that drives enrichment of Cr near grain boundaries. Cr also exhibits fast interstitial diffusion in Ni-Cr alloys, however it is counterbalanced by fast Cr diffusion via vacancies. This results in Cr depletion overall, however it is considerably more moderate than the Cr depletion that would result if interstitials played no role at all, as had been previously suggested.

This work has also yielded new insight into the effect of defect annihilation kinetics at grain boundaries on RIS. The magnitude of Cr enrichment in Fe-Cr was found to be strongly dependent upon the angle of the grain boundary, a phenomenon that was well captured by the RIS model. While this grain boundary angle dependence was expected based on earlier modeling and experimental efforts, it was previously believed that general high angle grain boundaries were essentially perfect sinks. However, model results in the Ni-Cr alloy system have revealed that even high angle grain boundaries must be treated as real sinks with finite annihilation kinetics in order to accurately capture RIS behavior at moderate to low temperatures.

5.2 Atomistic modeling of the order-disorder phase transformation in Ni-Cr alloys

Ni-Cr alloys near the composition Ni_2Cr are susceptible to a phase transformation from a disordered solid solution to the ordered $MoPt_2$ structure at temperatures below 500 °C. This

phase transformation has dramatic and adverse effects for material properties such as toughness and corrosion resistance. At temperatures relevant to nuclear applications, this phase transformation is very slow, requiring decades to proceed to completion. It has therefore proven very difficult to determine from experimental data alone the exact timescale of this phenomenon

In this project, a multiscale model was developed that combined DFT calculations, Monte Carlo simulations, and phase transformation theory in order to provide a more accurate prediction of the timescale of the phase transformation. This effort yielded a simple, novel model for computing the kinetics of the disorder to order phase transformation that showed excellent agreement with Monte Carlo simulations. When this model was parameterized with reasonable physical values, good agreement was observed with experimental measurements as well. The model allows for a much more precise prediction of the timescale of the transformation than earlier empirical models.

The predictions of this model indicate that at temperatures relevant to PWR operating conditions, the disorder to order transformation should not proceed to completion within 80 years, the longest current estimate for life extensions for PWRs. However, the model indicates that the initial stages of this transition could occur on this timescale, and experimental evidence suggests that even a small amount of ordered phase fraction can lead to significant embrittlement. This phase transformation may therefore be cause for concern for in Ni-Cr alloys near the stoichiometric composition, in components designed for very long service lifetimes.

5.3 Thermodynamic and kinetic modeling of oxide precipitation in nanostructured ferritic alloys

Nanostructured ferritic alloys are a promising candidate class of materials for structural components in proposed fusion and advanced fission reactor designs. These alloys exhibit excellent high temperature mechanical properties and high radiation damage resistance, which are both highly attractive characteristics for nuclear applications. The desirable properties of NFAs arise from a dense dispersion of nm-scale Y-Ti-O particles, which impede dislocation motion and provide a high density of trapping and annihilation sites for radiation produced defects.

Due to the very small size of these precipitates, details regarding their structures and phase identities are still uncertain, and their kinetic evolution under long term thermal aging conditions has not been well established. The goal of this project was to develop a modeling framework that could be used to gain important fundamental understanding into the nature of the nanoprecipitates, the effects of thermal aging under time and temperature conditions relevant to proposed advanced reactor concepts, and alloy composition effects on the nanoprecipitate size distribution. This modeling framework combined key DFT calculations of Y-Ti-O clustering energetics, thermodynamic analyses in the CALPHAD formalism, and kinetic precipitation simulations in a cluster-based rate theory approach.

The results of this model have led to a number of interesting and useful conclusions. DFT calculations of nanocluster energetics have revealed that clusters of Ti, Y, and O that are structurally similar to ground state Y and Ti oxide phases are extraordinarily stable even for clusters containing fewer than a dozen atoms, where high interfacial energies would destabilize

most other incoherent structures. This result indicates that the smallest nanoparticles are likely to be crystallites of stoichiometric oxide phases, and not coherent transition phases as had been previously suggested. The CALPHAD-based thermodynamic assessments produce reasonably accurate predictions of precipitate volume fractions and phase identities as functions of alloy composition, providing further evidence that the nanoparticles in NFAs are, to a good approximation, the equilibrium oxide phases of Y and Ti.

The kinetic precipitation model based upon these thermodynamic assessments has provided a number of mechanistic insights into the nanoprecipitate evolution in NFAs. Due to the very large formation energies of the oxide phases and the vanishing solubility of Y in the ferrite matrix, the experimentally observed nanoprecipitate coarsening behavior cannot be captured by a model assuming standard precipitation mechanisms through normal bulk diffusion; only a model that accounts for coarsening through dislocation pipe diffusion can reproduce the measured coarsening rates. This result indicates that pipe diffusion is likely the dominant mechanism of coarsening in NFAs. Predicted coarsening rates from a pipe diffusion-based model suggest that the nanoprecipitates should remain thermally stable at operating temperatures for proposed for NFA applications for at least 80 years. Finally, the best fit kinetic model provided a useful insight for alloy design: adding small amounts of Ti to Y-based NFAs should produce a finer distribution of particles, however this benefit is due mostly to the promotion of $Y_2Ti_2O_7$ relative to Y_2O_3. Therefore, Ti additions far beyond a 1:1 proportionality with the Y content in the alloy cease to have any particle-refining effect and serve only to promote the precipitation of TiO_2, which appears to have a negative impact on mechanical properties.

5.4 Integration and future work

During the next stage of this research project, the techniques developed above will be integrated to study the phenomenon of radiation induced precipitation (RIP) in austenitic stainless steels. Many researchers have observed the appearance of Ni-Si and Mn-Ni-Si precipitates in irradiated austenitic stainless steels [212-216], most commonly in alloys with high Ni concentration such as D9 and 316. Some of these precipitates have been identified as Ni_3Si or G-phase, an intermetallic phase with a nominal composition $M_6Ni_{16}Si_7$, where M is often Mn. The appearance of these phases is not generally observed under thermal aging at comparable temperatures, and their precipitation could have significant and unexpected consequences for the mechanical properties of the material. Understanding and predicting the precipitation of these phases is therefore crucial in forecasting the lifetime of these alloys under LWR operating conditions.

These precipitates are most often associated with voids, grain boundaries, and dislocation loops. Because both Si and Ni are strongly enriched by RIS in these alloys [21, 37] it is believed that these precipitates form due to large changes in local alloy chemistry near these features. Thus, a model framework for understanding and predicting RIP in austenitic stainless steels would begin with a first principles-based RIS model for Ni and Si, following the approach outlined in Chapter 2. The predicted local composition changes under irradiation will then be used to evaluate the thermodynamic driving forces for the precipitation of the Ni-Si rich phases. Because the Ni_3Si phase is an ordered fcc compound, the Monte Carlo techniques utilized in Chapter 3 are ideally suited augment available thermodynamic data for this phase, particularly at low temperatures. Finally, the modeling framework described in Chapter 4 would then be

applied to study the thermodynamics and kinetics of the precipitation of the Ni and Si rich phases.

5.4 Closing remarks

The research pursued here addressed a number of disparate phenomena with a wide variety of tools, however the work was unified by a general guiding multiscale approach. This approach began with utilizing DFT calculations to obtain important energies and to make crucial observations of atomic-level phenomena. The information gained in from these calculations was used to perform advanced atomistic simulations and ultimately to construct continuum level models for describing complex microstructural processes. Because of this atom-up approach, the models developed in this work have yielded not just reproductions of experimental data, but fundamental insight into the atomic-level mechanisms that govern the observed material behavior.

Bibliography

[1] Odette GR, Alinger MJ, Wirth BD. Recent developments in irradiation-resistant steels. Annual Review of Materials Research 2008;38:471-503.

[2] Odette GR, Hoelzer DT. Irradiation-tolerant Nanostructured Ferritic Alloys: Transforming Helium from a Liability to an Asset. Jom-Us 2010;62:84-92.

[3] Ardell AJ. RADIATION-INDUCED SOLUTE SEGREGATION IN ALLOYS. In: Ghetta V, Gorse D, Maziere D, Pontikis V, editors. Materials Issues for Generation IV Systems: Springer; 2008. p. 285.

[4] Was GS, Andresen PL. Irradiation-Assisted Stress-Corrosion Cracking in Austenitic Alloys. Jom-Journal of the Minerals Metals & Materials Society 1992;44:8-13.

[5] Was GS, Bruemmer SM. Effects of Irradiation on Intergranular Stress-Corrosion Cracking. Journal of Nuclear Materials 1994;216:326-47.

[6] Was GS, Wharry JP, Frisbie B, Wirth BD, Morgan D, Tucker JD, et al. Assessment of radiation-induced segregation mechanisms in austenitic and ferritic–martensitic alloys. Journal of Nuclear Materials 2011.

[7] Kim JH, Byun TS, Hoelzer DT, Kim SW, Lee BH. Temperature dependence of strengthening mechanisms in the nanostructured ferritic alloy 14YWT: Part I-Mechanical and microstructural observations. Mat Sci Eng a-Struct 2013;559:101-10.

[8] Kim JH, Byun TS, Hoelzer DT, Park CH, Yeom JT, Hong JK. Temperature dependence of strengthening mechanisms in the nanostructured ferritic alloy 14YWT: Part II-Mechanistic models and predictions. Mat Sci Eng a-Struct 2013;559:111-8.

[9] Was GS. Fundamentals of radiation materials science : metals and alloys. Berlin ; New York: Springer; 2007.

[10] Olander DR, United States. Energy Research and Development Administration. Division of Reactor Development and Demonstration. Fundamental aspects of nuclear reactor fuel elements : prepared for the Division of Reactor Development and Demonstration, Energy Research and Development Administration. Oak Ridge, Tenn.

Springfield, Va.: Technical Information Center, Office of Public Affairs

available [from] National Technical Information Service, U.S. Dept. of Commerce; 1976.

[11] Allen TR, Tan L, Was GS, Kenik EA. Thermal and radiation-induced segregation in model Ni-base alloys. Journal of Nuclear Materials 2007;361:174-83.

[12] Hanninen H, Aho-Mantila I. Environment-Sensitive Cracking of Reactor Internals. Third Int Symp Environmental Degradation of Materials in Nuclear Power Systems--Water Reactors: The Metallurgical Society; 1988. p. 77-92.

[13] Bruemmer SM, Was GS. Microstructural and Microchemical Mechanisms Controlling Intergranular Stress-Corrosion Cracking in Light-Water-Reactor Systems. Journal of Nuclear Materials 1994;216:348-63.

[14] Busby JT, Was GS, Kenik EA. Isolating the effect of radiation-induced segregation in irradiation-assisted stress corrosion cracking of austenitic stainless steels. Journal of Nuclear Materials 2002;302:20-40.

[15] Field KG, Barnard L, Parish CM, Busby JT, Morgan D, Allen TR. Dependence on grain boundary structure of radiation induced segregation in a 9 wt.% Cr model ferritic/martensitic steel. Journal of Nuclear Materials 2013;435:172-80.

[16] Wharry JP, Jiao Z, Was GS. Application of the inverse Kirkendall model of radiation-induced segregation to ferritic–martensitic alloys. Journal of Nuclear Materials 2011.

[17] Wiedersich H, Okamoto PR, Lam NQ. Theory of Radiation-Induced Segregation in Concentrated Alloys. Journal of Nuclear Materials 1979;83:98-108.

[18] Perks JM, Marwick AD, English CA. Computer code to calculate radiation induced segregation in concentrated ternary alloys. AERE-R-121211986. p. 48.

[19] Grandjean Y, Bellon P, Martin G. Kinetic-Model for Equilibrium and Nonequilibrium Segregation in Concentrated Alloys under Irradiation. Physical Review B 1994;50:4228-31.

[20] Allen TR, Was GS. Modeling radiation-induced segregation in austenitic Fe-Cr-Ni alloys. Acta Materialia 1998;46:3679-91.

[21] Fukuya K, Fujii K. A Multicomponent Model of Radiation-induced Segregation for Commercial Stainless Steels. Journal of Nuclear Science and Technology 2009;46:744-52.

[22] Tucker JD, Najafabadi R, Allen TR, Morgan D. Ab initio-based diffusion theory and tracer diffusion in Ni-Cr and Ni-Fe alloys. Journal of Nuclear Materials 2010;405:216-34.

[23] Nastar M, Bellon P, Martin G, Ruste J. Role of Interstitial and Interstitial-Impurity Interaction on Irradiation Induced Segregation in Austenitic Steels. Materials Research Society Symposium Proceedings 1998;481:383-8.

[24] Choudhury S, Barnard, L., Tucker, J. D., Allen, T. R., Wirth, B. D., Asta, M., Morgan, D. . Ab-initio based modeling of diffusion in dilute bcc Fe-Ni and Fe-Cr alloys and implications for radiation induced segregation. Journal of Nuclear Materials 2011;411:1-14.

[25] Soisson F. Kinetic Monte Carlo simulations of radiation induced segregation and precipitation. Journal of Nuclear Materials 2006;349:235-50.

[26] Allnatt AR, Lidiard AB. Atomic transport in solids. Cambridge [England] ; New York: Cambridge University Press; 1993.

[27] Van der Ven A, Yu HC, Ceder G, Thornton K. Vacancy mediated substitutional diffusion in binary crystalline solids. Progress in Materials Science 2009.

[28] Tucker JD, Allen TR, Najafabadi R, Morgan D. Determination of Solute-Interstitial Interactions in Ni-Cr by First Principles. International Conference on Advances in Mathematics, Computational Methods and Reactor Physics, M and C 2009;2:891.

[29] Radhakrishnan K, Hindmarsh, A. Description and Use of LSODE, the Livermore Solver for Ordinary Differential Equations. Lawrence Livermore National Laboratory Report 1993;UCRL-ID-113855.

[30] Lupis CHP. Chemical thermodynamics of materials. New York: North-Holland; 1983.

[31] Swoboda B, Van der Ven A, Morgan D. Assessing Concentration Dependence of FCC Metal Alloy Diffusion Coefficients Using Kinetic Monte Carlo. 2009.

[32] Manning JR. Correlation Factors for Diffusion in Nondilute Alloys. Physical Review B 1971;4:1111-&.

[33] Bocquet JL. Diffusion of Dumbbell Interstitials in Concentrated Random Alloys - an Effective Field Approximation. Acta Metallurgica 1986;34:571-97.

[34] Duh TS, Kai, J. J., Chen, F. R., Wang, L. H. Numerical simulation modeling of the effects of grain boundary misorientation on radiation-induced solute segregation in 304 austinitic stainless steels. Journal of Nuclear Materials 2001:267-73.

[35] Reed-Hill RE, Abbaschian R. Physical metallurgy principles. 3rd ed. Boston, Mass.: PWS-Kent Pub.; 1992.

[36] Read WT, Shockley W. Dislocation Models of Crystal Grain Boundaries. Physical Review 1950;78:275-89.

[37] Allen TR, Busby JT, Was GS, Kenik EA. On the mechanism of radiation-induced segregation in austenitic Fe-Cr-Ni alloys. Journal of Nuclear Materials 1998;255:44-58.

[38] Bonny G, Terentyev D, Malerba L. On the alpha-alpha ' miscibility gap of Fe-Cr alloys. Scripta Materialia 2008;59:1193-6.

[39] Carter RD, Damcott DL, Atzmon M, Was GS, Bruemmer SM, Kenik EA. Quantitative analysis of radiation-induced grain-boundary

segregation measurements. Journal of Nuclear Materials 1994;211:70-84.

[40] Wolfer WG. The dislocation bias. Journal of Computer-Aided Materials Design 2007;14:403-17.

[41] Woo CH, Singh BN. Production Bias Due to Clustering of Point-Defects in Irradiation-Induced Cascades. Philosophical Magazine a-Physics of Condensed Matter Structure Defects and Mechanical Properties 1992;65:889-912.

[42] Osetsky YN, Bacon DJ, Singh BN, Wirth B. Atomistic study of the generation, interaction, accumulation and annihilation of cascade-induced defect clusters. Journal of Nuclear Materials 2002;307:852-61.

[43] Sakaguchi N, Shibayama T, Kinoshita H, Takahashi H. Atomistic observation of radiation-induced grainboundary movement in Fe Cr Ni alloy under electron

irradiation. Philosophical Magazine Letters 2001;81:691-6.

[44] Hackett MJ, Najafabadi R, Was GS. Modeling solute-vacancy trapping at oversized solutes and its effect on radiation-induced segregation in Fe-Cr-Ni alloys. Journal of Nuclear Materials 2009;389:279-87.

[45] Ruzickova J, Million B. Self-diffusion of the components in the f.c.c. phase of binary solid solutions of the Fe-Ni-Cr system. Mat Sci & Eng 1981;50:59-64.

[46] Olsson P. Ab initio study of interstitial migration in Fe-cr alloys. Journal of Nuclear Materials 2009.

[47] Sakaguchi N, Takahashi H, Ichinose H. Influence of silicon and phosphorus on radiation-induced segregation of chromium and nickel in austenitic model alloys. Mater Trans 2005;46:440-4.

[48] Sakaguchi N, Watanabe S, Takahashi H. A new model for radiation-induced grain boundary segregation with grain boundary movement in concentrated alloy system. J Mater Sci 2005;40:889-93.

[49] Lam NQ, Kumar A, Weidersich H. In: Brager HR, Perrin JS, editors. Effects of Radiation on Materials, 11th Conference: American Society for Testing and Materials; 1982. p. 985.

[50] Stepanov IA, Pechenkin VA, Konobeev YV. Modeling of radiation-induced segregation at grain boundaries in Fe-Cr-Ni alloys. Journal of Nuclear Materials 2004;329-33:1214-8.

[51] Barnard L, Tucker JD, Choudhury S, Allen TR, Morgan D. Modeling Radiation Induced Segregation in Ni-Cr Model Alloys From First Principles. Journal of Nuclear Materials 2011.

[52] Kusunoki K. Molecular-dynamics study of self-interstitial diffusion in bcc-Iron. Mater Trans 2006;47:1906-9.

[53] Finkenstadt D, Bernstein N, Feldman JL, Mehl MJ, Papaconstantopoulos DA. Vibrational modes and diffusion of self-interstitial atoms in body-centered-cubic transition metals: A tight-binding molecular-dynamics study. Physical Review B 2006;74.

[54] Marian J, Wirth BD, Caro A, Sadigh B, Odette GR, Perlado JM, et al. Dynamics of self-interstitial cluster migration in pure alpha-Fe and Fe-Cu alloys. Physical Review B 2002;65.

[55] Terentyev D, Olsson P, Klaver TPC, Malerba L. On the migration and trapping of single self-interstitial atoms in dilute and concentrated Fe-Cr alloys: Atomistic study and comparison with resistivity recovery experiments. Computational Materials Science 2008;43:1183-92.

[56] Terentyev D, Olsson P, Malerba L. Diffusion of 3D-migrating self-interstitial clusters in diluted and concentrated Fe-Cr alloys. Journal of Nuclear Materials 2009;386-88:140-2.

[57] Wong KL, Shim JH, Wirth BD. Molecular dynamics simulations of point defect interactions in Fe-Cr alloys. Journal of Nuclear Materials 2007;367:276-81.

[58] Pechenkin VA, Molodstov VL, Ryabov VA, Terentyev D. On the radiation-induced segregation: Contribution of interstitial mechanism in Fe–Cr alloys. Journal of Nuclear Materials 2013;433:372-7.

[59] Sanchez J, Fullea J, Andrade MC, de Andres PL. Ab initio molecular dynamics simulation of hydrogen diffusion in alpha-iron. Physical Review B 2010;81.

[60] Sahli B, Fichtner W. Ab initio molecular dynamics simulation of self-interstitial diffusion in silicon. Physical Review B 2005;72.

[61] Mohn CE, Stolen S, Hull S. Diffusion within alpha-CuI studied using ab initio molecular dynamics simulations. J Phys-Condens Mat 2009;21.

[62] Kresse G. Thesis: Technische University at Wien; 1993.

[63] Kresse G, Furthmuller J. Efficient iterative schemes for ab initio total-energy calculations using a plane-wave basis set. Physical Review B 1996;54:11169-86.

[64] Kresse G, Furthmuller J. Efficiency of ab-initio total energy calculations for metals and semiconductors using a plane-wave basis set. Computational Materials Science 1996;6:15-50.

[65] Kresse G, Hafner J. Abinitio Molecular-Dynamics for Liquid-Metals. Physical Review B 1993;47:558-61.

[66] Perdew JP, Burke K, Ernzerhof M. Generalized gradient approximation made simple. Physical Review Letters 1996;77:3865-8.

[67] Blochl PE. Projector augmented-wave method. Phys Rev B 1994;50:953.

[68] Nose S. A Unified Formulation of the Constant Temperature Molecular-Dynamics Methods. J Chem Phys 1984;81:511-9.

[69] Zeng ZY, Hu CE, Cai LC, Jing FQ. Ab initio study of lattice dynamics and thermal equation of state of Ni. Physica B 2012;407:330-4.

[70] G. KT. Measurement of the thermal-expansion coefficient of nickel from 300 to 1000 K and determination of the power-law constants near the Curie temperature. Physical Review B 1977;16:4872-81.

[71] Karmazin L. Lattice Parameter Studies of Structure Changes of Ni-Cr Alloys in the Region of Ni2Cr. Mat Sci & Eng 1982;54:247-56.

[72] Karger J, Ruthven DM. Diffusion in zeolites and other microporous solids. University of Michigan: Wiley; 1992.

[73] Haile JM. Molecular Dynamics Simulation: Elementary Methods: Wiley-Interscience; 1997.

[74] Van der Ven A, Ceder G, Asta M, Tepesch PD. First-principles theory of ionic diffusion with nondilute carriers. Physical Review B 2001;64:184307.

[75] Bocquet JL. Towards a General Formulation for the Phenomenological Coefficients of Diffusion Lij in Concentrated Random Alloys. Res Mechanica 1987;22:1-44.

[76] Allnatt AR. Einstein and Linear Response Formulas for the Phenomenological Coefficients for Isothermal Matter Transport in Solids. Journal of Physics C-Solid State Physics 1982;15:5605-13.

[77] Ehrhart. Atomic Defects in Metals. Berlin: Landolt-Bornstein Springer-Verlag; 1991.

[78] Dimitrov C, Dimitrov O. Influence of Nickel Concentration on Point-Defect Migration in High-Nickel Fe-Cr-Ni Alloys. Journal of Nuclear Materials 1988;152:21-9.

[79] Lorenz CD, Ziff RM. Universality of the excess number of clusters and the crossing probability function in three-dimensional percolation. J Phys a-Math Gen 1998;31:8147-57.

[80] Million B, Ruzickova J, Velisek J, Vrestal J. Diffusion-Processes in the Fe-Ni System. Mater Sci Eng 1981;50:43-52.

[81] Ruzickova J, Million B. Self-Diffusion of the Components in the Fcc Phase of Binary Solid-Solutions of the Fe-Ni-Cr System. Mater Sci Eng 1981;50:59-64.

[82] Rittner JD, Seidman DN. <110> symmetric tilt grain-boundary structures in fcc metals with low stacking-fault energies. Physical Review B 1996;54:6999-7015.

[83] Rtishchev VV, Vintajkin EZ, Pigrova GD, Udovenko VA. Fiz Met Metalloved 1977;43.

[84] Berkowitz BJ, Miller C. The Effect of Ordering on the Hydrogen Embrittlement Susceptibility of Ni2Cr. Metallurgical Transactions A 1980;11A:1877-81.

[85] Kargol JA, Zeller MV, Asfahani R, Parrill TM. AES STUDIES OFPHOSPHORUS IMPURITY ON HYDROGEN EMBRITFLEMENT OF Ni2Cr. Applications of Surface Science 1983;15:129-48.

[86] Marucco A, Nath B. Effects of Ordering on the Properties of Ni-Cr Alloys. J Mat Sci 1988;23:2107-14.

[87] Marucco A. Atomic Ordering in the Ni-Cr-Fe System. Mat Sci & Eng 1994;A189:267-76.

[88] Marucco A. Effects of Composition on the Order-Disorder Transformation in Ni-Cr Based Alloys. Key Engineering Materials. Switzerland: Trans Tech Publications; 1990. p. 77-90.

[89] Kim S, Kuk IH, Kim JS. Order-disorder raction in Alloy 600. Materials Science and Engineering A 2000;A279:142-8.

[90] Delabrouille F, Renaud D, Vaillaint F, Massoud J. Long Range Ordering of Alloy 690. 14th International Conference on Environmental Degradation of Materials in Nuclear Power Systems. Virginia Beach, VA2009. p. 888-94.

[91] Karmazin L, Krejci J, Zeman J. gamma Phase and Ni2Cr-type long-range order in Ni-rich Ni-Cr-Mo alloys. Materials Science and Engineering A 1993;A183:103-9.

[92] Kolmogorov A. A statistical theory for the recrystallization of metals. Akad nauk SSSR, Izv, Ser Matem 1937;1.

[93] Johnson W, Mehl R. Reaction kinetics in processes of nucleation and growth. Trans AIME 1939;135.

[94] Avrami M. Kinetics of Phase Change. I: General Theory. J Chem Phys 1939;7.

[95] Avrami M. Kinetics of Phase Change. II: Transformation-Time relations for random distribution of nuclei. J Chem Phys 1940;8.

[96] Avrami M. Kinetics of Phase Change. III: Granulation, Phase Change an Microstructures. J Chem Phys 1941;9.

[97] Sun NX, Liu XD, Lu K. An explanation to the anomalous avrami exponent. Scripta Materialia 1995;34:1201-7.

[98] Metropolis N, Rosenbluth AW, Rosenbluth MN, Teller AH, Teller E. J Chem Phys 1953;21.

[99] Voter AF. Introduction to the Kinetic Monte Carlo Method. In: Sickafus KE, Kotomin EA, editors. Radiation Effects in Solids. Dordrecht: (Springer; 2005.

[100] Van der Ven A, Thomas JC, Xu Q, Swoboda B, Morgan D. Nondilute diffusion from first principles: Li diffusion in LixTiS2. Physical Review B 2008;78.

[101] Van der Ven A, Thomas JC, Xu Q, Bhattacharya J. Linking the electronic structure of solids to their thermodynamic and kinetic properties. Mathematics and Computers in Simulation 2010;80:1393-410.

[102] Van de Walle A, Ceder G. J Phase Equilib 2002;23.

[103] de Fontaine D. In: Ehrenreich H, Turnbull D, editors. Solid State Physics. New York: Academic Press; 1994. p. 33.

[104] Sanchez JM, Ducastelle F, Gratias D. General Cluster Descriptions of Multicomponent Systems. Physica A 1984;128.

[105] de Fontaine D. Configurational Thermodynamics of Solid Solutions. Solid State Physics 1979;34.

[106] Van der Ven A, Ceder G. Vacancies in ordered and disordered binary alloys treated with the cluster expansion. Phys Rev B 2005;71.

[107] Van der Ven A. Coarse graining vacancies in binary alloys where the vacancy concentration is very low. to be submitted 2013.

[108] Frenkel D, Smit B. Understanding molecular simulation : from algorithms to applications. 2nd ed. San Diego, Calif. ; London: Academic; 2002.

[109] Allnatt AR, Lidiard AB. Atomic Transport in Solids: Cambridge University Press; 1993.

[110] Kang HC, Weinberg WH. J Chem Phys 1989;90.

[111] Ehrhart P. Atomic Defects in Metals. New York: Springer Verlag; 1991.

[112] Bonny G, Terentyev D, Malerba L, Van Neck D. Early stages of alpha-alpha prime phase separation in Fe-Cr alloys: An atomistic study. Physical Review B 2009;79.

[113] Nash P. Bull Alloy Phase Diag 1986;7.

[114] Vineyard GH. Theory of Order-Disorder Kinetics. Physical Review 1955;102:981-92.

[115] Dienes GJ. Kinetics of Order-Disorder Transformations. Acta Metallurgica 1955;3:549-57.

[116] De Koning M, Ramos de Debiaggi S, Monti AM. Atomistic calculation of vacancy-formation free energies by reversible vacancy creation. Physical Review B 2004;70.

[117] Foiles SM, Baskes MI, Daw MS. Embedded-Atom-Method Functions for the Fcc Metals Cu, Ag, Au, Ni, Pd, Pt, and Their Alloys. Physical Review B 1986;33:7983-91.

[118] Korzhavyi PA, Abrikosov IA, Johansson B, Ruban AV, Skriver HL. First-principles calculations of the vacancy formation energy in transition and noble metals. Physical Review B 1999;59:11693-703.

[119] Scholz H. Universitat zu Gottingen; 2001.

[120] Smedskjaer LC, Fluss MJ, Legnini DG, Chason MK, Siegel RW. The Vacancy Formation Enthalpy in Ni Determined by Positron-Annihilation. J Phys F Met Phys 1981;11:2221-30.

[121] Zhao L, Najafabadi R, Srolovitz DJ. Finite-Temperature Vacancy Formation Thermodynamics - Local Harmonic and Quasi-Harmonic Studies. Model Simul Mater Sc 1993;1:539-51.

[122] Miller MK, Parish CM, Li Q. Advanced oxide dispersion strengthened and nanostructured ferritic alloys. Mater Sci Tech-Lond 2013;29:1174-8.

[123] Ukai S, Fujiwara M. Perspective of ODS alloys application in nuclear environments. Journal of Nuclear Materials 2002;307:749-57.

[124] Cunningham N, Odette GR. On the Remarkable Thermal Stability of Nanostructured Ferritic Alloys. Acta Materialia submitted 2013.

[125] De Bremaecker A. Past research and fabrication conducted at SCK center dot CEN on ferritic ODS alloys used as cladding for FBR's fuel pins. Journal of Nuclear Materials 2012;428:13-30.

[126] Eiselt CC, Klimenkov M, Lindau R, Moslang A. Characteristic results and prospects of the 13Cr-1W-0.3Ti-0.3Y(2)O(3) ODS steel. Journal of Nuclear Materials 2009;386-88:525-8.

[127] Klueh RL, Shingledecker JP, Swindeman RW, Hoelzer DT. Oxide dispersion-strengthened steels: A comparison of some commercial and experimental alloys. Journal of Nuclear Materials 2005;341:103-14.

[128] Schneibel JH, Liu CT, Miller MK, Mills MJ, Sarosi P, Heilmaier M, et al. Ultrafine-grained nanocluster-strengthened alloys with unusually high creep strength. Scripta Materialia 2009;61:793-6.

[129] Miao P, Odette GR, Yamamoto T, Alinger M, Klingensmith D. Thermal stability of nano-structured ferritic alloy. Journal of Nuclear Materials 2008;377:59-64.

[130] Alinger M. Thesis: University of California Santa Barbara; 2004.

[131] Alinger MJ, Odette GR, Hoelzer DT. On the role of alloy composition and processing parameters in nanocluster formation and dispersion strengthening in nanostuctured ferritic alloys. Acta Materialia 2009;57:392-406.

[132] Klimiankou M, Lindau R, Moslang A. HRTEM Study of yttrium oxide particles in ODS steels for fusion reactor application. Journal of Crystal Growth 2003;249:381-7.

[133] Ramar A, Baluc N, Schaublin R. On the lattice coherency of oxide particles dispersed in EUROFER97. Journal of Nuclear Materials 2009;386:515-9.

[134] Ribis J, de Carlan Y. Interfacial strained structure and orientation relationships of the nanosized oxide particles deduced from elasticity-driven morphology in oxide dispersion strengthened materials. Acta Materialia 2012;60:238-52.

[135] Wu Y, Haney EM, Cunningham NJ, Odette GR. Transmission electron microscopy characterization of the nanofeatures in nanostructured ferritic alloy MA957. Acta Materialia 2012;60:3456-68.

[136] Ohnuma M, Suzuki J, Ohtsuka S. A new method for the quantitative analysis of the scale

and composition of nanosized oxide in 9Cr-ODS steel. Acta Materialia 2009;57:5571-81.

[137] Kim SW, Shobu T, Ohtsuka S, Kaito T, Inoue M, Ohnuma M. Kinetic Approach for Growth and Coalescence of Nano-Size Oxide Particles in 9Cr-ODS Steel Using High-Energy Synchrotron Radiation X-rays in SPring-8. Materials Transactions 2009;50:917-21.

[138] Yamashita S, Ohtsuka S, Akasaka N, Ukai S, Ohnuki S. Formation of nanoscale complex oxide particles in mechanically alloyed ferritic steel. Phil Mag Lett 2004;84:525-9.

[139] Miller MK, Kenik EA, Russell KF, Heatherly L, Hoelzer DT, Maziasz PJ. Atom probe tomography of nanoscale particles in ODS ferritic alloys. Mat Sci Eng a-Struct 2003;353:140-5.

[140] Miller MK, Russell KF, Hoelzer DT. Characterization of precipitates in MA/ODS ferritic alloys. Journal of Nuclear Materials 2006;351:261-8.

[141] Miller MK, Hoelzer DT, Kenik EA, Russell KF. Nanometer scale precipitation in ferritic MA/ODS alloy MA957. Journal of Nuclear Materials 2004;329:338-41.

[142] Marquis EA. Core/shell structures of oxygen-rich nanofeatures in oxide-dispersion strengthened Fe-Cr alloys. Appl Phys Lett 2008;93.

[143] Williams CA, Smith GDW, Marquis EA. The effect of Ti on the coarsening behavior of oxygen-rich nanoparticles in oxide-dispersion-strengthened steels after annealing at 1200 degrees C. Scripta Materialia 2012;67:108-11.

[144] Williams CA, Smith GDW, Marquis EA. Quantifying the composition of yttrium and oxygen rich nanoparticles in oxide dispersion strengthened steels. Ultramicroscopy 2013;125:10-7.

[145] Williams CA, Unifantowicz P, Baluc N, Smith GDW, Marquis EA. The formation and evolution of oxide particles in oxide-dispersion-strengthened ferritic steels during processing. Acta Materialia 2013;61:2219-35.

[146] Fu CL, Krcmar M, Painter GS, Chen XQ. Vacancy mechanism of high oxygen solubility and nucleation of stable oxygen-enriched clusters in Fe. Physical Review Letters 2007;99:-.

[147] Jiang Y, Smith JR, Odette GR. Formation of Y-Ti-O nanoclusters in nanostructured ferritic alloys: A first-principles study. Physical Review B 2009;79:-.

[148] Gopejenko A, Zhukovskii YF, Vladimirov PV, Kotomin EA, Moslang A. Ab initio simulation of yttrium oxide nanocluster formation on fcc Fe lattice. Journal of Nuclear Materials 2010;406:345-50.

[149] Murali D, Panigrahi BK, Valsakumar MC, Chandra S, Sundar CS, Raj B. The role of minor alloying elements on the stability and dispersion of yttria nanoclusters in nanostructured ferritic alloys: An ab initio study. Journal of Nuclear Materials 2010;403:113-6.

[150] Wu Y, Haney E, Odette GR, Cunningham N. TEM Characterization of the Structure and Composition of the Nanofeatures in Nanostructured Ferritic Alloy MA957. Fusion Materials Semiannual Progress Report, DOE/ER-0313/502011.

[151] Cancarevic M, Zinkevich M, Aldinger F. Thermodynamic description of the Ti-O system using the associate model for the liquid phase. Calphad 2007;31:330-42.

[152] Jamieson JC, Olinger B, Dachille F, Simons PY, Roy R. Pressure-Temperature Studies of Anatase, Brookite Rutile and Tio2 (Ii) - a Discussion. American Mineralogist 1969;54:1477-&.

[153] Waldner P, Eriksson G. Thermodynamic modelling of the system titanium-oxygen. Calphad-Computer Coupling of Phase Diagrams and Thermochemistry 1999;23:189-218.

[154] Li X, Finnis MW, He J, Behera RK, Phillpot SR, Sinnott SB, et al. Energetics of charged point defects in rutile TiO2 by density functional theory. Acta Materialia 2009;57:5882-91.

[155] Paton MG, Maslen EN. A Refinement of Crystal Structure of Yttria. Acta Crystallographica 1965;19:307-&.

[156] Hin C, Wirth BD. Formation of Y2O3 nanoclusters in nano-structured ferritic alloys: Modeling of precipitation kinetics and yield strength. Journal of Nuclear Materials 2010;402:30-7.

[157] Uchida Y, Ohnuki S, Hashimoto N, Suda T, Nagai T, Shibayama T, et al. Effect of Minor Alloying Element on Dispersing Nano-Particles in ODS Steel. Mater Res Soc Symp Proc 2007;981.

[158] Jiang Y, Smith JR, Odette GR. Prediction of structural, electronic and elastic properties of Y2Ti2O7 and Y2TiO5. Acta Materialia 2010;58:1536-43.

[159] Etienne BA, Cunningham N, Wu Y, Odette GR. Effects of friction stir welding and post-weld annealing on nanostructured ferritic alloy. Mat Sciand Tech 2011;27:724-8.

[160] Gong WP, Li DJ, Chen ZS, Zheng F, Liu Y, Du Y, et al. Phase equilibria of the TiO2-Y2O3 system. Calphad 2009;33:624-7.

[161] Djurovic D, Zinkevich M, Aldinger F. Thermodynamic modeling of the yttrium-oxygen system. Calphad 2007;31:560-6.

[162] Dinsdale AT. Sgte Data for Pure Elements. Calphad 1991;15:317-425.

[163] Bo H, Wang J, Duarte L, Leinenbach C, Liu LB, Liu HS, et al. Thermodynamic re-assessment of Fe-Ti binary system. T Nonferr Metal Soc 2012;22:2204-11.

[164] Du Z, Zhang W, Zhuang Y. Thermodynamic assessment of the Fe-Y system. Rare metals 1996;16:52-8.

[165] Ghosh G. Thermodynamic and kinetic modeling of the Cr-Ti-V system. J Phase Equilib 2002;23:310-28.

[166] Hasek B. Thesis: Thermodynamoc modeling and first-principles calculations of the Cr-Hf-Y ternary system: The Pennsylvania State University; 2010.

[167] Brocq M, Radiguet B, Poissonnet S, Cuvilly F, Pareige P, Legendre F. Nanoscale characterization and formation mechanism of nanoclusters in an ODS steel elaborated by reactive-inspired ball-milling and annealing. Journal of Nuclear Materials 2011;409:80-5.

[168] de Castro V, Marquis EA, Lozano-Perez S, Pareja R, Jenkins ML. Stability of nanoscale secondary phases in an oxide dispersion strengthened Fe-12Cr alloy. Acta Materialia 2011;59:3927-36.

[169] Oksiuta Z, Lewandowska M, Unifantowicz P, Baluc N, Kurzydlowski KJ. Influence of Y2O3 and Fe2Y additions on the formation of nano-scale oxide particles and the mechanical properties of an ODS RAF steel. Fusion Eng Des 2011;86:2417-20.

[170] Auger MA, de Castro V, Leguey T, Munoz A, Pareja R. Microstructure and mechanical behavior of ODS and non-ODS Fe-14Cr model alloys produced by spark plasma sintering. Journal of Nuclear Materials 2013;436:68-75.

[171] Lee JH. Oxidation of Oxide Dispersion Strengthened Steels: I. Influence of Alloy Composition. Advanced Materials Research 2013;748:86-90.

[172] Caudron E, Buscail H, Cueff R, Issartel C, Perrier S, Riffard F. GAXRD and in situ X-ray diffraction characterizations of the yttrium implantation effect on pure iron oxidation at high temperature. Journal of Physics IV France 2002;Pr6.

[173] Ramanarayanan TA. Investigations on the Growth Mechanisms of a-Cr2O3 on Ni-Base Alloys with and without Y2O3 Dispersions. Bunsen Society for Physical Chemistry 1985;89:402-9.

[174] Barlow R, Grundy PJ. Determination of Diffusion Constants of Oxygen in Nickel and Alpha-Iron by an Internal Oxidation Method. Journal of Materials Science 1969;4:797-&.

[175] Klugkist P, Herzig C. Tracer diffusion of Titanium in a-Iron. Physica status solidi 1995;148:413-21.

[176] Murali D, Panigrahi BK, Valsakumar MC, Sundar CS. Diffusion of Y and Ti/Zr in bcc iron: A first principles study. Journal of Nuclear Materials 2011;419:208-12.

[177] Slezov VV, Schmelzer J. Kinetics of formation of a phase with an arbitrary stoichiometric composition in a multicomponent solid solution. Phys Rev E 2002;65.

[178] Slezov VV. Kinetics of first order phase transitions. Weinheim: Wiley-VCH; 2009. p. 1 online resource (xiv, 415 p.).

[179] Clouet E, Barbu A, Lae L, Martin G. Precipitation kinetics of A1(3)Zr and Al3SC in aluminum alloys modeled with cluster dynamics. Acta Materialia 2005;53:2313-25.

[180] Ardell AJ. Coarsening of Grain-Boundary Precipitates. Acta Metall Mater 1972;20:601-&.

[181] Love GR. Dislocation pipe diffusion. Acta Metall Mater 1964;12:731-7.

[182] Miller KM, Ingle KW, Crocker AG. A Computer-Simulation Study of Pipe Diffusion in Body-Centered Cubic Metals. Acta Metall Mater 1981;29:1599-606.

[183] Mishin Y, Herzig C. Grain boundary diffusion: recent progress and future research. Mat Sci Eng a-Struct 1999;260:55-71.

[184] Picu RC, Zhang D. Atomistic study of pipe diffusion in Al-Mg alloys. Acta Materialia 2004;52:161-71.

[185] Song SH, Chen XM, Weng LQ. Solute diffusion during high-temperature plastic deformation in alloys. Mat Sci Eng a-Struct 2011;528:7196-9.

[186] Mantzouris X, Zouvelou N, Skarmoutsos D, Nikolopoulos P, Tietz F. Interfacial properties and structure stability of Ni/Y-2 O-3-ZrO2-TiO2 cermet anodes for solid oxide fuel cells. Journal of Materials Science 2005;40:2471-5.

[187] Triantafyllou G, Angelopoulos GN, Nikolopoulos P. Surface and grain-boundary energies as well as surface mass transport in polycrystalline yttrium oxide. Journal of Materials Science 2010;45:2015-22.

[188] Hindmarsh AC, Brown PN, Grant KE, Lee SL, Serban R, Shumaker DE, et al. SUNDIALS: Suite of nonlinear and differential/algebraic equation solvers. Acm T Math Software 2005;31:363-96.

[189] Franciosi P. Glide Mechanisms in Bcc Crystals - an Investigation of the Case of Alpha-Iron through Multislip and Latent Hardening Tests. Acta Metall Mater 1983;31:1331-42.

[190] Gehlen PC, Rosenfie.Ar, Hahn GT. Structure of (100) Edge Dislocation in Iron. J Appl Phys 1968;39:5246-&.

[191] Oksiuta Z, Baluc N. Role of Cr and Ti contents on the microstructure and mechanical

properties of ODS ferritic steels. Advanced Materials Research 2009;59:-.

[192] Heintze C, Hernández-Mayoral M, Ulbricht A, Bergner F, Shariq A, Weissgärber T, et al. Nanoscale characterization of ODS Fe–9%Cr model alloys compacted by spark plasma sintering. Journal of Nuclear Materials 2012;428:139-46.

[193] Olier P, Malaplate J, Mathon MH, Nunes D, Hamon D, Toualbi L, et al. Chemical and microstructural evolution on ODS Fe–14CrWTi steel during manufacturing stages. Journal of Nuclear Materials 2012;428:40-6.

[194] Száraz Z, Török G, Kršjak V, Hähner P. SANS investigation of microstructure evolution in high chromium ODS steels after thermal ageing. Journal of Nuclear Materials 2013;435:56-62.

[195] Zhong SY, Ribis J, Klosek V, de Carlan Y, Lochet N, Ji V, et al. Study of the thermal stability of nanoparticle distributions in an oxide dispersion strengthened (ODS) ferritic alloys. Journal of Nuclear Materials 2012;428:154-9.

[196] Gavrilyuk VG, Kushnareva NP, Prokopenko VG. Alloyage Influence on Dislocation Mobility in Alpha-Iron. Fiz Met Metalloved+ 1976;42:1288-93.

[197] Henderson B. Defects in crystalline solids. London,: Edward Arnold; 1972.

[198] Kamber K, Keefer D, Wert C. Interactions of interstitials with dislocations in Iron. Acta Metall Mater 1961;9:403-14.

[199] Petarra DP, Beshers DN. Cold-Work Internal Friction Peak in Iron. Acta Metall Mater 1967;15:791-&.

[200] Thomas WR, Leak GM. The Binding Energy of Nitrogen in a Dislocation. Proc Phys Soc B 1955;68:1001-7.

[201] Clouet E, Garruchet S, Nguyen H, Perez M, Becquart CS. Dislocation interaction with C in alpha-Fe: A comparison between atomic simulations and elasticity theory. Acta Materialia 2008;56:3450-60.

[202] Cochardt AW, Schoek G, Wiedersich H. Interaction between dislocations and interstitial atoms in body-centered cubic metals. Acta Metall Mater 1955;3:533-7.

[203] De Hosson JTM. An atomic model for the interaction between a /2<111>(110) edge dislocation and carbon in Fe. Solid State Communications 1975;17.

[204] Feng YQ, Wang CY. Electronic effects of light impurities on edge dislocation motion in iron at T=0 K. J Alloy Compd 2000;312:219-27.

[205] Tapasa K, Osetsky YN, Bacon DJ. Computer simulation of interaction of an edge dislocation with a carbon interstitial in alpha-iron and effects on glide. Acta Materialia 2007;55:93-104.

[206] Wang R. Nonlocal Elastic Interaction Energy between a Dislocation and a Point-Defect. J Phys D Appl Phys 1990;23:263-5.

[207] Howe JM. Interfaces in materials : atomic structure, thermodynamics and kinetics of solid-vapor, solid-liquid and solid-solid interfaces. New York: Wiley; 1997.

[208] Certain AG, Field KG, Allen TR, Miller MK, Bentley J, Busby JT. Response of nanoclusters in a 9Cr ODS steel to 1dpa, 525°C proton irradiation. Journal of Nuclear Materials 2010;407:2-9.

[209] Lescoat ML, Ribis J, Gentils A, Kaïtasov O, de Carlan Y, Legris A. In situ TEM study of the stability of nano-oxides in ODS steels under ion-irradiation. Journal of Nuclear Materials 2012;428:176-82.

[210] Dou P, Kimura A, Kasada R, Okuda T, Inoue M, Ukai S, et al. Effects of titanium concentration and tungsten addition on the nano-mesoscopic structure of high-Cr oxide dispersion strengthened (ODS) ferritic steels. Journal of Nuclear Materials 2013;442:S95-S100.

[211] He P, Klimenkov M, Lindau R, Möslang A. Characterization of precipitates in nano structured 14% Cr ODS alloys for fusion application. Journal of Nuclear Materials 2012;428:131-8.

[212] Boothby RM, Harries DR, Williams TM. Precipitation and Void-Swelling in Nickel-Manganese Austenitic Stainless-Steels. J Nucl Mater 1983;115:16-24.

[213] Brager HR, Garner FA. Influence of Neutron-Spectra on the Radiation-Induced Evolution of Aisi-316. J Nucl Mater 1982;108:347-58.

[214] Lee EH, Mansur LK. Fe-15Ni-13Cr austenitic stainless steels for fission and fusion reactor applications. III. Phase stability during heavy ion irradiation. J Nucl Mater 2000;278:20-9.

[215] Maziasz PJ. Formation and Stability of Radiation-Induced Phases in Neutron-Irradiated Austenitic and Ferritic Steels. J Nucl Mater 1989;169:95-115.

[216] Maziasz PJ. Overview of Microstructural Evolution in Neutron-Irradiated Austenitic Stainless-Steels. J Nucl Mater 1993;205:118-45.